Spring 2019

Off Axis Compressive Response of Ice-Templated Ceramics

Rahul Kumar Jujjavarapu
Old Dominion University

OFF AXIS COMPRESSIVE RESPONSE OF ICE TEMPLATED CERAMICS

by
Rahul Kumar Jujjavarapu
B. Tech. 2014 ALIET, Jawaharlal Nehru Technological University, India

A Thesis Submitted to the Faculty of
Old Dominion University in Partial Fulfillment of the
Requirements for the Degree of

MASTER OF SCIENCE

MECHANICAL ENGINEERING

OLD DOMINION UNIVERSITY

May 2019

Approved by:

Oleksandr Kravchenko (Director)

Dipankar Ghosh (Member)

Xiaoyu Zhang (Member)

ABSTRACT

OFF AXIS COMPRESSIVE RESPONSE OF ICE TEMPLATED CERAMICS

Rahul Kumar Jujjavarapu
Old Dominion University, 2019
Co-Directors: Dr. Oleksandr Kravchenko
Dr. Dipankar Ghosh

The off-axis compressive behavior of ice-templated ceramic was analyzed using experimental results and micro-mechanical model simulation. Ice-templated ceramics is a versatile processing technique used to manufacture anisotropic ceramic foam by exploiting the anisotropic growth characteristics and lamellar morphology. The ice-templating process results in processing-structure-property relationships determined by the microstructure. The processed alumina samples which were later manufactured by water jet machine from the freeze casting were tested under quasi-static off-axis loading conditions and were used to determine the mechanical properties of the material. Digital image correlation (DIC) was used to measure the strain response of ice-templated ceramic under off-axis loading. DIC results revealed non-homogenous strain distribution in the material during compression. Specifically, the origin of the localized strain concentration columnar regions, which are oriented in the ice-growth direction. Those regions were found to be the onset failure of in off-axis and 0-degree loading conditions. The experimental results reveal the strong influence of the loading direction on the compressive behavior of the ice-templated ceramic. A Representative Volume Element is developed to predict the behavior of off-axis loading. Micro-mechanical loading results in indicated that buckling of lamella walls were determined as the driving factor of failure. The results of the model compared favorably with the experimental results.

This thesis is dedicated to my parents and my American family.

ACKNOWLEDGEMENTS

Firstly, I take the privilege graduating from Frank Batten College of Engineering & Technology. Thanks to my advisors Dr. Kravchenko and Dr. Ghosh who believed in me to do research and gave me continuous encouragement to write my thesis successfully. Their constant gentle criticism helped to shape my character as well as my academics. Their untiring efforts deserve special appreciation. I should thank my fellow lab mates Mr. Mahesh, Mr. Shashanka, Mr. Ben, and Mr. Siavash who assisted and assured my experiments with their experienced training. I would like to thank Dr. Flory, Chair of Department of Engineering Technology and Dr. Bawab, Chair of Mechanical and Aerospace Engineering, who supported me during the period of my study. There are many other people who prayed and constantly wished to complete my work at ODU. I am obliged to my parents for their unwavering support to meet my educational goals.

NOMENCLATURE

A	Cross sectional area
L	length
F	Force
F_t	Force rate
G	Shear Force
m	cosine angle
n	sine angle
U	is the displacement
x	component
y	component
z	component

Greek symbols

σ	Normal Stress
ε	Normal Strain (Engineering Strain)
ε_t	Strain rate
ν	is the Poison's ratio
τ	is shear strain
α	is the angle of orientation
θ	Angle

TABLE OF CONTENTS

LIST OF TABLES

Table Page

LIST OF FIGURES

CHAPTER 1

Introduction

In this era, as the usage of composite materials is increased, ceramics have taken their unique place, Ceramics are by definition compounds between metallic and non-metallic elements. This thesis mainly focuses on a specific ceramic as it discussed the studies the mechanical behavior of ice-templated Aluminum Oxide (Al_2O_3). This material has started to be used as a component in special and advanced engineering applications [1]. Due to the excellent properties of aluminum oxide such as resistance to a wide range of chemical agents, lighter weight than metals, and strength characteristics compared to other metals, innovative design cost is economical. Through the investigation of the microstructure, this ice-templated alumina is observed to be cellular ceramics. Cellular solids, in the form of either honeycomb-like materials with prismatic cells or foams with polyhedral cells, are widely used in engineering applications such as lightweight structural sandwich panels or components designed for absorbing impact energy [1]. They also appear widely in natural materials such as wood and bone. Models which predict their compressive failure behavior have broad applicability to both engineered and natural cellular materials. Cellular ceramics are a class of highly porous materials that cover a wide range of structures, such as foams, honeycombs, interconnected rods, interconnected fibers, inter-connected hollow spheres. These highly porous materials have a lot of applications as filters for molten metal, hot gas and diesel engine exhausts filters, catalyst carriers, biomaterials, thermal insulators for furnaces and aerospace applications, gas combustion burners and lightweight building materials [1]. This work used powders that are commercially available. Specifically, ice-templated scaffolds were processed from the commercially available Al_2O_3

powders of different sizes. The suspensions used to prepare the samples were processed from these powders. These suspensions were again employed through a process which is a prominent technique in the ceramics field named as freeze casting.

These alumina powders are processed through a technique called freeze casting. It is a cost effective and environmentally friendly technique. In this technique, an aqueous and non-aqueous solution particulate suspension is solidified under a unidirectional temperature gradient. During unidirectional solidification of an aqueous particulate suspension, ice crystals nucleate and grow from the bottom to the top of the suspension i.e. in the direction of the applied unidirectional thermal gradient [2,4,5]. The ice crystals start to grow at the bottom of the suspension and propagate upwards under the influence of the applied thermal gradient. The mold which is made of Teflon tube where the suspensions placed is radially insulated to avoid horizontal thermal gradient and ensure the aqueous suspensions are solidified only in the vertical direction. This Teflon tube is placed on a steel plate. Their gap is adjusted between the steel plate and the top of nitrogen gas to control the freezing front velocity. The thermocouple is placed on the steel plate to measure the temperature during the freezing process.

Scanning electron microscopy analysis reveals some interesting microstructural morphology exhibited by freeze casted ceramics. Specifically, lamellar pore morphology is observed where architecture found to be in the form of alternating layers is interconnected with the bridges. Therefore, this anisotropic morphology stems from the processing technique. The ideal fabrication technique should produce scaffolds with controlled pore size, shape, and orientation in a reliable and economical way. Experimental and numerical investigations on natural cellular solids suggest that such anisotropic pore architecture could be beneficial to improve the mechanical and functional properties of engineering cellular solids. There are studies done to

understand the various processes of ceramic materials and physics behind the process and establish the processing micro structural relationship.

The uniaxial compressive response of ice-templated sintered alumina scaffolds has a strong dependence on the solids loading of ceramic suspensions and freezing velocity. It is observed that the variation of the particle size has a significant effect on the freezing front velocity [5]. Moreover, increasing the solids loading there is a transition in the pore morphology, and the FFV is observed to be more drastic for scaffolds processed. In the previous work, it states that microstructure of each Al_2O_3 scaffold was characterized from two different planes transverse to the freezing direction. The addition of platelets to the suspension showed improvement of the mechanical response in which it is rationalized based on the stiffening and strengthening effects exhibited by the intralamellar and interlamellar platelets.

It is observed that low FFV regime platelets are mainly present within the lamella walls whereas increasing the FFV more platelets can be found in between the walls that developed lamellar bridges. The investigations reveal that for a given suspension concentration, not only the FFV but also the platelets content can induce significant microstructural modifications [6]. Now with the increase of platelets, the fraction of the lamellar bridges also increased. There is a tremendous amount of increase in the stiffness, peak stress, and plateau stress and energy absorption capacity with the inclusion of the platelets. The dendritic architecture is observed by the pore volume where highly lamellar pore morphology is seen.

At comparable freezing front velocity, smaller particles will have a greater tendency to be ejected by the advancing ice front in comparison to relatively large [5]. The studies reveal that process microstructure relationship and the properties of the material were responsible for its compressive strength. Further, making observations of the micrographs reveals the walls of

alumina have alternatively occurred; with the inclusion of platelets the bridges are formed. The anisotropic materials manifest different properties in different directions, which made us focus on studying different orientations.

The variation of the normalized quasi-static compressive strength with relative density reasonably predicted by the Gibson and Ashley for closed-cell, open cell, and honeycomb foams, which gives insight for computational modeling. A honeycomb-shaped structure provides a material with minimal density and relatively high out-of-plane compressive properties and out-of-plane shear properties. Computational micromechanics stands as a very useful tool in this area as it can provide virtual tests which can be used to check the different failure criteria. The experimental study of the mechanical behavior of alumina scaffolds has been studied under transverse and longitudinal compression, as well as in off-axis compressive loading cases. The representative volume element (RVE) was proposed for the micromechanical analysis based on the honeycomb analogy. Representative volume element (RVE) is the smallest volume over which a measurement can be made that will yield a value representative of the whole. Abaqus software was used to develop a RVE. Further, to design the model in the Abaqus we studied the spacing between the lamella walls and angle of the bridges with respect to the lower lamella wall from the micrographs. Modeling results indicated that buckling of the lamella walls was determined to be the driving factor of failure. The results of the model have been compared with the experimental results.

CHAPTER 2

Literature Review

2.1 Cellular solids and its applications

Cellular solids are prevalent in natural and engineered structures; models that can explain their mechanical behavior have widespread utility. Generally, porosity is detrimental in engineering solids because of the undesirable effects on the mechanical and functional properties in the end applications. However, most of the engineering solids such as metals, ceramics, and polymers contain a very small percentage of processing-induced porosity, which is inevitable. Interestingly, there are numerous natural solids such as bones, cork, wood, leaves, sponges, and coral where the constituent materials are arranged in a fashion that leads to the formation of a two- or three-dimensional arrangement of pores creating highly porous architectures [2]. Successful models of cellular solids can be used to understand their observed behaviors and predict the behaviors from a description microstructural property such as relative density and the orientation. Cellular solid is one made up of an interconnected network of solid struts or plates, which form the edges and face of cells. The single most important feature of a cellular solid is its relative density. As the relative density increases, the cell wall thickens, and the pore space shrinks. Cellular solids have physical, mechanical and thermal properties which are measured by the same methods as those used for fully dense solids. The major applications of the cellular materials are thermal insulation, packaging, structural use, and buoyancy. Most of the cellular solids have been used for thermal insulation [1] in products as humble as disposable coffee cups and as elaborate as the insulation of the booster rockets for the space shuttle. Modern buildings,

transport systems, and even ships all take advantage of the lower thermal conductivity of the expanded plastic foams. The second major use of the man-made cellular solids is in packaging. An effective package must absorb the energy of impacts or of forces generated by deceleration without subjecting the contents to damaging stresses. The strength of the cellular solids can be adjusted by controlling its relative density. These can undergo large compressive strains at almost constant stress so that a large amount of energy can be absorbed without generating high stresses.

Many natural structural materials are cellular solids: wood, cancellous bone, and coral all support large static and cyclic loads, for a longer period. The structural use of natural cellular materials by man is as old as history itself. The shape and structure of cells are important because the properties of cellular solids depend directly on the shape and structure of the cells. Cellular solids have relative densities, which are less than about 0.3; most are much less, with densities as low as 0.003 [1]. The structure of the cellular solids ranges from the near-perfect order of the bee's honeycomb to being disordered. The study of the geometry of the three-dimensional cellular solids has a pedigree almost as distinguished as that of honeycomb. The material description should be as full as possible, to allow the solid material properties to be identified. The density is straightforward: it is usually adequate to cut a block of foam, measure its dimensions, and weigh it. But in seeking the correlations between properties and structure it is important to measure the density of each sample since densities can vary by 10% or more in a single batch of material.

Cellular ceramics are processed by sintering of loosely packed of ceramic powder compacts, which mainly leads to the formation of open-cell porous materials. By definition, sintering is a heat treatment process in which a powder or porous material, already formed into a required shape, is converted to useful solid. Sintering is achieved by heating the consolidated mass of

particles, referred to as the green body or powder compact, to a temperature that is in the range between approximately 50% and 80% of melting temperature. The powder is heated below its melting point which results in joining together of the particles and the densification of the body as required in the fabrication process. This type of sintering is referred to as solid-state sintering. The key objective of the sintering studies is, therefore, to understand how the processing variables influence the microstructure.

Ceramics have covalent bonds which are strong giving the materials higher melting points and moduli other than any solid [9]. The strong bonding has another consequence: it gives strong elastic coupling between atoms. This gives thermal conductivities which are larger by a factor of about 100 than those of polymers. The strong ionic and covalent bonds give ceramics a relatively high modulus. The modulus slightly varies with temperature.

Honeycombs shed light on the mechanics of much more complex three-dimensional foams. If a honeycomb is compressed in-plane, the cell walls at first bend, giving linear elastic deformation. Beyond a critical strain the cell collapses by elastic buckling, plastic yielding, creep, or brittle fracture, depending on the cell wall material [1]. As these are brittle materials it tends to fracture. The in-plane stiffness and strengths are the lowest because stresses in the plane make cell walls bend. The out-plane stiffness and strengths are much larger because they require the axial extension or compression of the cell walls. In brittle materials it is by the brittle fracture of the cell walls, at high strains, the cells collapse sufficiently that opposing cell walls touch and further deformation compresses the cell material itself. The increase in the relative density of honeycomb increases the relative thickness of cell walls. Then resistance to cell wall bending and cell collapse rises, giving a higher modulus and plateau stress; and the cell walls touch sooner, reducing the strain at which densification begins. Honeycombs are much stiffer and

stronger when loaded along the cell-axis in the z-direction. Similarly, it shows high values of strength and stiffness in the z-direction out of the plane. For out-of-plane loading, the initial linear elastic deformation involves significant axial or shear deformations of the cell walls whereas the latter part of the curve is by tearing or crushing

2.2 Unidirectional Freezing of Aqueous particulate suspensions.

Cellular ceramics can be engineered to combine several advantages inherent to their architecture: they are lightweight, can have open or closed porosity making them useful as insulator or fillers, can withstand high temperatures and exhibit high specific strength, and are particular in compression. The full potential of cellular ceramics will only be achieved once a proper control of size, shape, and amount of porosity is available. There are several methods for processing of cellular ceramics: replica method, direct foaming, sacrificial phase foaming, paste extrusion, amorphous bubble bonding, and rapid prototyping.

The replica method is a heat treatment process where the burn off the polymer component, which leaves behind a ceramic skeleton and is then sintered to develop a porous ceramic structure that is a replica of the starting polymeric foam. A typical ceramic foam microstructure is obtained through the replica method. Secondly, for indirect foaming technique, a ceramic suspension is first foamed by introducing gas bubbles into suspension. Then the suspension is polymerized to retain the porous architecture induced through the gas bubbles, followed by demolding, drying, and sintering to develop a porous ceramic structure. Next, the sintered foams are glazed to improve the mechanical properties of the porous ceramic structure. Thirdly, the sacrificial phase technique for the fabrication of porous ceramics involves in the preparation of a two-phase composite consisting of a continuous matrix of ceramic and sacrificial particulate phase. Fourth, paste extrusion is a conventional technique generally employed to manufacture honeycombs mainly used for catalysts and filters. In this paste extrusion technique, a paste of ceramic powder, binders, and the lubricating agent is prepared using high-shear mixing. An extrusion ram forces through a die and results in the extruded product of the desired shape, which can be further molded into required shape and length; the extruded green bodies go through a typical ceramic

processing route of drying, the binder burns out, and sintering produces the final macroporous ceramics. Fifth, the amorphous bubble bonding a unique cellular solid fabrication technique is where hollow spheres can be bonded together by applying heat to a cellular network of precursor hollow spheres. Sixth, rapid prototyping technique, also known as solid free-form fabrication, is employed to produce a scaled or full-sized prototype from complex datasets, in which three-dimensional objects are assembled by point, line or planar addition of the material [2].

The above techniques are utilized to fabricate cellular ceramics for various applications. Although the control over the structure and functional properties of cellular ceramics is continuously improving, all the processing routes suffer from an inherent limitation: every processing route is intrinsically limited to a narrow range of pore characteristics. In addition, removal of the pore foaming agent can be considered the problem, and efforts have been input in developing processing routes with environmentally friendly pore forming agents, yielding techniques such as gel casting, direct foaming or recent developments with particles-stabilized wet foams. In pursuit of such processing routes, freeze casting has attracted considerably more focus in the last few years because of the ability to develop bio-inspired novel porous ceramics, which can be post-processed to dense hybrid materials. This technique exploits the anisotropic growth characteristics of solvent crystals and phases segregation of particulate suspensions under unidirectional freezing conditions to develop hierarchical porous solids. Although various solvents have been attempted, water remains as the predominantly employed freezing vehicle because of the availability and similarity of the resultant structure that are major interests to design bio-inspired materials. A key feature of the freeze-cast porous solids is the presence of the tunable anisotropic pore morphology with low tortuosity that is highly suitable for structural, biomedical, and energy storage applications. Moreover, within a wide range of wide porosity

freeze cast, porous ceramics exhibit significantly greater compressive strength in comparison to isotropic porous ceramics processed using the other techniques.

Freeze casting has first been developed as a near net shape forming technique, yielding dense ceramics parts with a fine replicate of mold details. Any ice crystal being converted into porosity later on its porosity in the process, introducing large size defects are unwelcome in ceramic applications. It is realized that the formation and growth of ice crystals is a substantial benefit if it is properly controlled. During the solidification of the slurry where the structure is formed, characteristics of the future porosity are determined. During this stage, continuous crystals of solvent that formed under certain conditions and grew into the slurry are rejected by moving of solidification. The technique consists of freezing a liquid suspension followed by sublimation of the solidified phase from solid to gas under reduced pressure, and subsequent sintering to consolidate and densify the wall, leading to porous structure with unidirectional freezing, where pores are a replica of solvent crystals. In freeze-casting, the particles in suspension in the slurry are rejected from the moving solidification front and piled up between the growing cellular solvent crystals.

2.3 Digital Image Correlation

Digital Image Correlation (DIC), also referred to photogrammetry, was developed in the early 1980s at the University of South California as a method for the full field analysis of surface strain [10]. The digital image correlation has demonstrated uses in the following industries: automotive, aerospace, biological, industrial, research and educational, government and military, and electronics. This method is based on the calculation of surface deformation using a set of digital images from un-deformed and deformed states. The technique consists of capturing grey-scale images of a random or regular surface pattern using cameras. The surface pattern is typically applied in the form of dark speckles on top of a white/high contrast base, providing patterns that can easily be recognized from image to image. This surface pattern deforms during loading. Image facets are created within the captured images allowing for surface coordinates and deformation to be tracked from image to image with sub-pixel accuracy. Upon the conclusion of processing, a complete strain map of the specimen surface is obtained. Originally developed as a 2D technique, measurements utilize a single camera focused directly on the surface of the planar specimen undergoing planar deformation. This technique is limited by the requirement that the specimen must undergo only planar motion. Out of plane motion and lack of parallel positioning introduces error into measurement making 2D digital image correlation impractical to apply to cylinders in uniaxial compression. This three-dimensional technique involves the use of two digital cameras. The cameras are placed so that the specimen surface is viewed from two different angles creating a full-field three-dimensional measurement of the specimen shape and displacements.

This image correlation is a non-contact measuring technique for determining 3D coordinates, 3D motion, surface deformation, and strain. 3D images were captured by using high-speed cameras.

The edge of using this camera is to ensure the accuracy of the strain data measured with the digital image correlation system. An optically based sensing system that can measure the displacement and strain over essentially the entire area of utility-scale blade leads to a measuring system that can significantly reduce the time and cost associated with traditional instrumentation. 2D or 3D image correlation photogrammetry can also be combined with high-speed cameras. These image correlations used for providing full-field results with extensive quantitative capability extends its applicability in various studies [13]. It is used to find out the radial strain result in an armored housing on a bracket, aimed at a prepared area of interest on the composite flywheel with possible crack radiation [13]. These cameras were used in high-speed tire dynamometer testing where the tire speeds up to required kilometers per hour where the pictures are captured showing principal strains on the complete tire. The software can calculate strains between any two different measurement conditions, and additional images can be added to a measurement series. There is no problem importing a reference image of the unloaded tire and then recalculating the strains relative to this new reference point, if so desired. Alternatively, the relative strain between any two intermediate steps in a long measurement sequence can be calculated in addition to the automatically calculated strains relative to the first step. High-speed materials from the fracture mechanics to production-rate forming limit analysis are ideally suited for the 3D image correlation method. This correlation system with fully integrated number of frames per second allows frame cropping to significantly increase the frame rate. By reducing the active pixels, the frame rates can be significantly increased. The robustness of 3D image correlation photogrammetry becomes clearest when dynamic deformations are considered. The usage of high-speed cameras, the method can capture high-speed events such as ballistic and crash events. Dielectric elastomers are currently being developed due to their significant

potential advantages over alternatives such as shape memory alloys [13]. Important criteria are high elastic strain, low power dissipation, wide operating temperature range, and rapid actuation with precise control. 3D image correlation photogrammetry is an excellent tool for evaluating the performance of these actuators.

3D coordinates are measured and evaluated using stereo-camera setup; therefore, the specimen is allowed to move in 3D space and the coordinates will be calculated in x, y and z so distance changes are no problem. For the 3D evaluation setup, a sensor setup is required using stereo camera setup lighting in terms of hardware as well as software basically the ARAMIS professional software is then used leading over the technical part. 3D cameras have out-of-plane motion detection; the other thing one should consider is lighting therefore good measurement needs to have good illumination depending on the frame rate lamps need to be powerful for the slow speed measurements. It is important to provide proper illumination to ensure enough image contrast and to ensure short shutter time for fast motions. 3D systems basically do have a stereo camera frame on which the cameras are mounted to provide enough mechanical stability and thus provide accurate 3D coordinates throughout the measurement.

Initially, the stochastic patterns are sprayed on the manufactured sample by using black aerosol paints. Before processing to testing of the sample to avoid any kind distortion from the lenses. the calibration is done. The ARAMIS software computes the coordinates on the pattern in each individual image or frame of a video. The use of a rigid geometrical construction compensates for the lens distortion, which shows effect in practice. Based on the sample dimensions the focal lengths of the camera and the distance between the camera and the sample are chosen from the ARAMIS manual. The next step is to perform the calibration and position the camera at a distance that allows you to cover as much as possible of your specimen. Make sure the camera is

placed perpendicular onto the object in both horizontal and vertical axis to avoid pseudo strain due to the out-of-plane movement of the object. Then focus the camera to determine the displacements to scale the images.

After calibration begins the compression test and record the images. The recorded video or the images are then analyzed in the GOM correlate software. The first step in this software is to create the surface component using squared facets on the acquired images, then the stochastic pattern structure is identified automatically for all the available images. The pattern quality was checked for all tests and satisfied the recommended parameters to allow for the reliable measurement of strain. A three-dimensional gradient tensor field is calculated to create strain distribution profiles capable of displaying both major and minor strain of specimen during loading. Now the full field strain distribution is displayed on top of the image data and you can see a legend of displaying strain values; in addition, we can also do the point wise inspection with deviation labels. The available strain data of x and y values allows us to find out the poison's ratio values for different oriented manufactured samples.

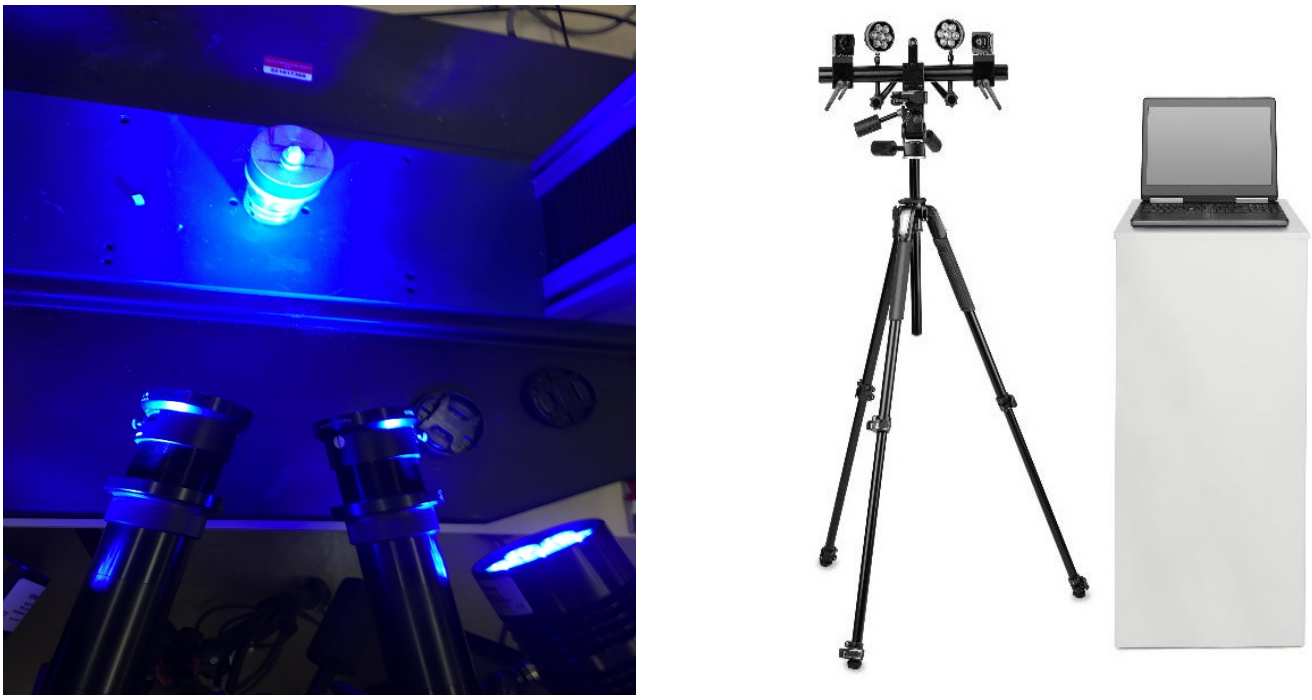

Figure 1(a) The illuminating light focusing on the sample before calibration 1(b) The figure represents the 3D camera mounted on tripod and the system to compute data for the test of specimen.

Fig 1(a) represents the illuminating light focusing on the sample to get a better image in the provided DIC system. Then the better image will be able to measure the distance between the center of the tripod to the face of the sample and further proceeded by calibration before the test. Fig 1(b) represents the significant devices the camera mounted on the tripod and system provided with ARAMIS software to compute the data for the test of the specimen.

2.4 Computational Methods

The microstructural features of cellular solids affecting their mechanical response are most easily observed in engineering honeycombs and foams. Honeycombs, with their prismatic cells, are referred to as two-dimensional cellular solids, while foams with their polyhedral cells are three- dimensional cellular solids. The relative density is the density of the cellular solid divided by that of the solid it is made from and is equivalent to the volume fraction of solid.

The wide range of demanding applications has grown in ceramics due to recent advancements in fabrications that enable the production of sub-micrometer grained ceramics which are free of impurities and amorphous phases at the grain boundaries. The extensive application of ceramics is still limited by their low fracture toughness and large variability of strength in comparison to metals [12,13]. Therefore, it is essential to gain a thorough understanding of not only the fracture process at the microscopic level but its relation to macroscopic material behavior. Linking numerical modeling with sound experiments and theory is paramount to reaching this goal.

In the theory of composite materials, the representative elementary volume (REV), also called the representative volume element (RVE) or the unit cell [14], is the smallest volume over which a measurement can be made that will yield a value representative of the whole. Representative volume element (RVE) for a material point of the continuum is a material volume which is statistically representative for the infinitesimal material neighborhood of the material point. It is known as a heterogeneous material with spatially varying but known constitutive properties. It is of importance that statistical properties of the state variables are considered invariant of the position in the material. This is called statistical homogeneity.

To build a RVE model ABAQUS package is used. ABAQUS is a complete finite-element environment that provides a simple, consistent interface for creating, submitting, monitoring, and evaluating results from Abaqus/Standard and Abaqus/Explicit simulations. Abaqus is divided into modules, where each module defines a logical aspect of the modeling process; for instance, defining the geometry, defining the material properties, and generating mesh. As we move from module to module, we can build the model from which Abaqus generates an input file that the user submits to the Abaqus/Explicit analysis product. The analysis product performs the analysis, sends the information to Abaqus to allow monitoring the progress of the job, and generates output database. Finally, the visualization module of Abaqus can be used to read the output database and view the results of the analysis.

Modeling Approach:

The model is built and analyzed in the following steps. Parts define the geometry of the individual components of the model and, therefore, are the building blocks of an Abaqus model. It is possible to create parts that are native to Abaqus or to import parts created by other applications either as a geometric representation or as a finite element mesh. Then the material properties like Young's modulus and Poison's ratio are defined. Properties of part can be defined through sections. A solid homogenous section is created, and this section is assigned to RVE. Each part is oriented in its own coordinate system and is independent of other parts in the model. Although the model may contain many parts, it contains only one assembly. It is possible to define the geometry of the assembly by creating instances of a part and then positioning the instances relative to each other in a global coordinate system. An instance can be classified as either independent or dependent. Independent part instances are meshed individually, while the mesh of a dependent part instance is associated with the mesh of the original part. By default, part instances are dependent and so for this part.

The mesh module allows generating meshes on parts and assemblies created within Abaqus/CAE. As with creating parts and assemblies, the process of assigning mesh attributes to the mode - such as seeds, mesh techniques, and element types - is feature based. As a result, the user can modify the parameters that define a part or an assembly, and the mesh attributes within the mesh module that are regenerated are automatically specified. Applying prescribed conditions, such as loads and boundary conditions, are step dependent, which means that the user must specify the step or steps in which they become active. Now that steps are already defined in the analysis, this section defines prescribed conditions. In structural analyses, boundary conditions are applied to those regions of the model where the displacements and/or rotations are

known. Such regions may be constrained to remain fixed during the simulation or may have specified, nonzero displacements and/or rotations.

The periodic boundary conditions are applied to simulate the process in a small part of large system. Each side in the computational cell is interacting not only with adjacent side in the cell but also with their images in the adjacent boxes. The choice of the position of the original box has no effect on the forces or behavior of the system.

Once all the tasks involved in defining a model are done, and then the job module can be used to analyze the model. The job module allows for creating a job, submitting it for analysis, and monitoring the progress. Multiple models can be created and monitored simultaneously. In addition, there is an option of creating only the analysis input file for model. This option allows viewing and editing the input file before submitting it for analysis. Graphical post processing is important because of the great volume of data created during a simulation. The visualization module of Abaqus/CAE allows viewing the results graphically using a variety of methods, including deformed shapes plots, contour plots, vector plots, animations, and X-Y plots. In addition, it allows creating tabular reports of the output data.

CHAPTER 3

Preparation of Freeze Casting Alumina

3.1 Experimental Set Up and Operational Procedure of Freeze Casting

The ice-templating process has attracted an increasing effect over the last few years, particularly in the field of porous ceramics. Freeze Casting is a versatile technique that involves solidification of particulate suspension under the influence of a unidirectional temperature gradient that facilities anisotropic growth of solvent crystals. Therefore, the freeze casting technique requires a device that can enable uni-directional freezing of particulate suspensions under well-controlled cooling conditions. Although the technique is simple in principle, there is no commercial set up available yet that can be readily employed to process materials under unidirectional freezing conditions. The main components of this device are liquid Nitrogen L-N_2; cold finger, which is made of thin steel plate; and a cryogenic temperature measurement system that records temperature of suspensions as low as -100°C. The Dewar used in the experiment is thermally insulated cylindrical vacuum flask with a capacity of 3L. This L-N_2 Dewar is placed on a thick aluminum base plate on which all the components of the device are attached. In order to avoid all the vibrations and to ensure that the plate is parallel to the ground, the leveling screws with rubber discs are attached to the base plate. The stoppers are attached to the top surface of the base plate to fix the Dewar at the center of the plate. A metal plate is attached to one side of the base plate to fix the Dewar at the center of the plate. The temperature measurement system is placed on the metal plate which is attached to the base plate.

A long metal sleeve concentric with the threaded rod rests on a circular nut, which is attached to the rod. As the nut rotates, the long metal sleeve can move vertically along the threaded rod.

There are two L-shaped hollow arms that are attached to the setup. One end of one of the L-shaped arms (called L-N_2 level indicator) is fixed to a large metal disk, which is attached directly to the long metal sleeve towards the upper end, and a small metal plate is fixed at the other end of the arm. On the L-N_2 level indicator, a funnel is also attached at the top that is used for pouring L-N_2 into the Dewar. The mechanism was devised that allows to measure the L-N_2 level within the Dewar and adjust the gap in between the L-N_2 top surface and the cold finger. The other L-shaped arm holding the cold finger at one end is attached to a short metal sleeve through the other end, where the short sleeve is concentric with the long metal sleeve. The Teflon mold is placed on the cold finger where the prepared suspension is placed in it. The suspension is in contact with the cold finger which is placed above the liquid nitrogen surface. The temperature of the suspension starts to decrease rapidly at the bottom compared to the top within the mold is subjected to unidirectional temperature gradient where the temperature increases from bottom to top.

A digital micrometer is also connected to short metal sleeve, where the movement of the spindle of the micrometer controls the vertical movement of the short sleeve along the long sleeve. Both sides of the cold finger (i.e., thin steel plate) are metallographically polished, and the circular shape (diameter ~90 mm) of the plate helps to maintain a uniform temperature distribution over the cold finger. As illustrated in Fig. 2 the cold-finger is not directly attached to the L-shaped metal arm, rather is connected through a Teflon connector to minimize the heat transfer to the cold-finger from the metal arm. The angle in between the cold-finger and metal arm is 90°, which keeps the cold-finger parallel to the L-N_2 surface inside the Dewar. It is also of note that prior to start of an experiment, both the metal plate on the L-N_2 level indicator and cold-finger reside at the same height from the base plate. The low temperature measurement system consists

of a 4-channel thermocouple data logger and a T type thermocouple (Omega Engineering Inc., Stamford, CT), where the thermocouple is attached on the top surface of the cold finger. T type thermocouple is chosen because it is suitable for extremely low-temperature applications (e.g., cryogenics and ultra-low freezers) and has excellent repeatability within the temperature range of -200°C to 350°C with an accuracy of +/- 1°C and sensitivity of about 43 µV/°C

The operation set up is set up is shown in the below pictures describing each component. Fig. 2(a) represents thermally insulated container, which is named as Dewar. The Fig. 2(b) represents the base plate, which holds the Dewar with stoppers mounted on it, and the leveling screws were placed under the base plate for support and ensure the base plate is parallel to the ground. Fig. 2(c) is represented to present L-shaped arms for Liquid-N_2 indicator and cold finger threaded rod and circular nut. Fig. 2(d) presents digital micrometer, short metal sleeve, and large metal disc. The Fig. 2 (e) shows the data logger. Fig. 2(f) shows the cold finger [2].

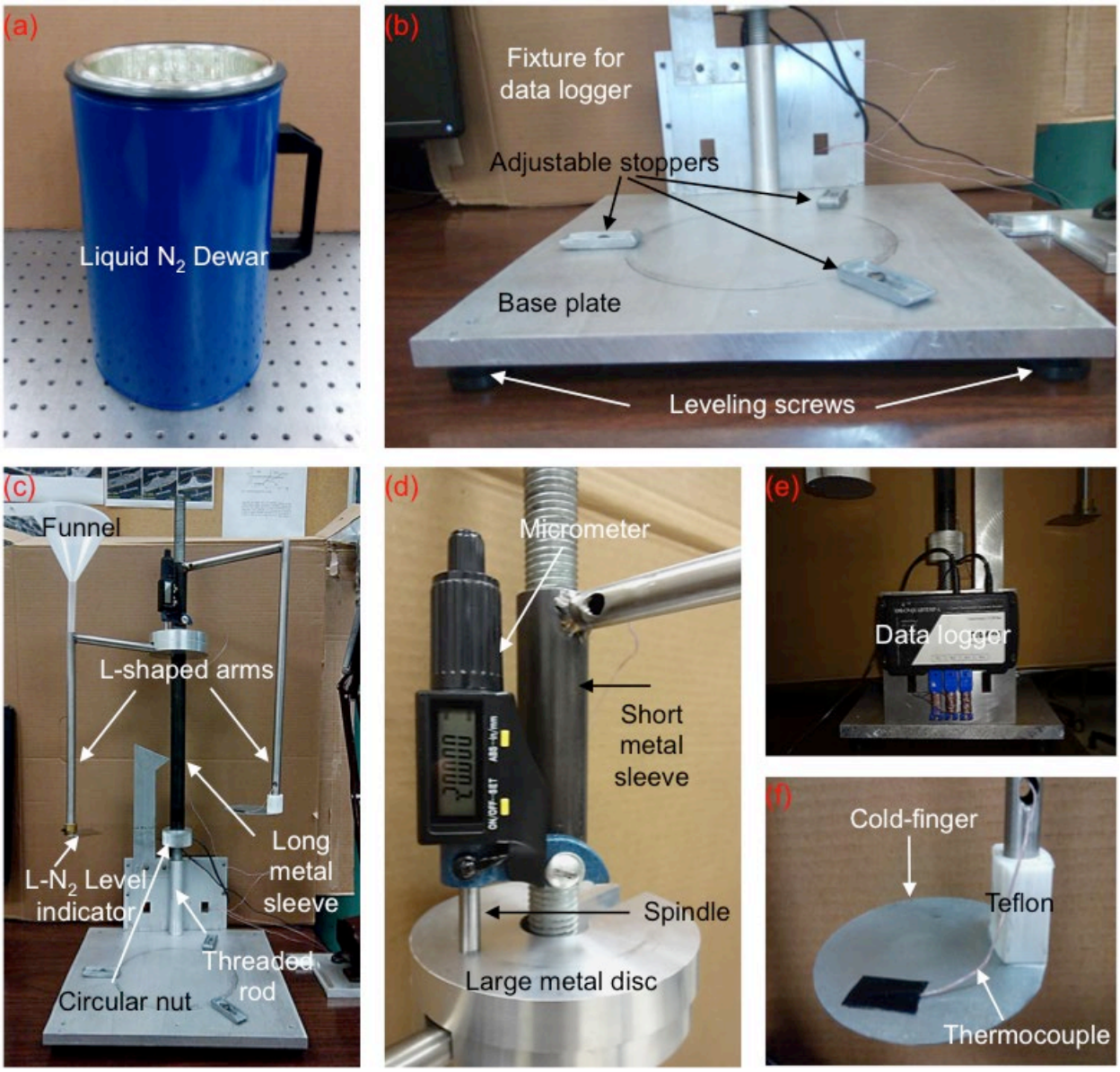

Figure 2 Images of the actual components of the custom-made freeze casting device: (a) liquid N2 Dewar, (b) base plate, fixture for data logger, leveling screws, and adjustable stoppers, (c) L-shaped arms for the L-N2 level indicator and cold finger, threaded rod and circular nut,(d) digital micrometer, short sleeve, and large metal disc,(e) data logger,(f) cold finger [2].

3.2 Processing of Freeze Casting

The various processing steps involved in the freeze casting are described in this section. Initially, it is important to prepare well-dispersed aqueous solution, for that the required amount of ceramic powder, deionized water and milling media (ZrO_2, spheres of 5mm diameter) were mixed in a Nalgene bottle. In order to stabilize the suspension, a small amount of dispersant (typically 0.5 wt.% of the powder) was also added to the suspension. Next, the suspension was ball milled for 24 hours on the ball-milling device as shown in Fig. 3(a).

After completion of ball milling, a binder was added to the suspension (typically 5 wt.% of the powder) and mixed for another hour. Afterward, the ZrO_2 spheres were separated from the suspension followed by de-airing for 30 min shown in Fig. 3(b). This process is done on a device where the vacuum pump is connected to a container, in which the suspension is placed to remove the air bubbles. After this step the suspension is casted into the mold by freezing with Liquid N_2 as shown in Fig. 3(c). Afterwards, the frozen samples were freeze dried for 96 hours at low pressure and low temperature shown in Fig. 3(d). Next the freeze dried samples were sintered in a box furnace Fig. 3 (e). Fig. 4. describes about the processing steps of the sample preparation where the image were represented in the Fig. 3. The flow chart in detail give us detailed process of preliminary step of the solution preparation then proceeding step wise to sintering to manufacture green alumina samples.

Figure 3 Processing Steps involved in unidirectional freeze casting: 3(a) Ball Milling 3(b) De-airing of suspension 3(c) Freeze Casting 3(d) Freeze Drying 3(e) Sintering

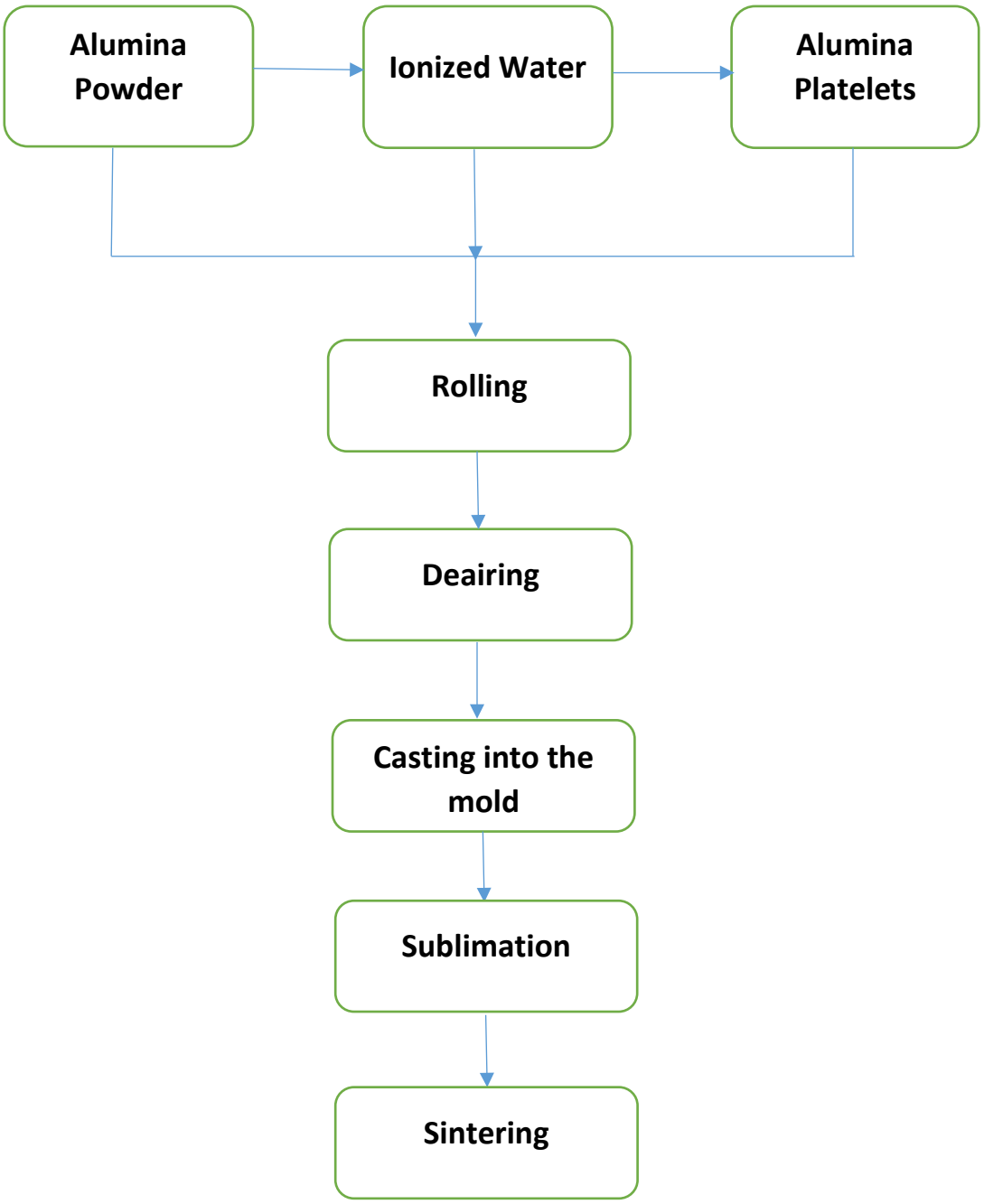

Figure 4 Flow chart of Freeze Casting Processing steps and the final solidification of the prepared samples

Preliminary studies stated that the amount of Liquid N_2 in the Dewar is one critical parameter to control freezing kinetics [5,6]. During this experiment the freezing velocity is not varied; this suggests the gap between the cold finger and the Liquid N_2 is constant for each prepared sample. This ensures that both the cold finger and the Teflon mold containing ceramic suspension are retained within the cooling zone inside the Dewar during freeze casting. It was decided to utilize 1.75 L of L-N_2 for each experiment. To measure the desired amount of Liquid N_2, which is contained in the Dewar, a level indicator is placed in the Dewar, which can move vertically on the threaded rod to adjust the position for different volume of L-N_2 in the Dewar. Afterwards the Liquid N_2 is poured into Dewar through the funnel until top surface of liquid touches the metal plate of level indicator. This indicates the desired volume of L-N_2 is present within the Dewar. The level indicator is then moved out of Dewar. The next step is to adjust the gap in between the cold finger and top surface of L-N_2 which is performed using the digital micrometer.

As the spindle moves out of the micrometer, the L-shaped arm containing the cold-finger moves upward and digital reading on the micrometer indicates the magnitude of the vertical displacement. Using the micrometer, the cold-finger is displaced upward until the desired gap in between the cold-finger and L-N_2 is achieved. As mentioned previously, by adjusting the gap in between the cold-finger and L-N_2, unidirectional temperature gradient and thus the freezing front velocity are controlled.

In the next step, a Teflon tube is placed on the cold finger, which is utilized as mold to contain ceramic suspension during freeze casting. Both ends of the Teflon tube are polished to make them flat and parallel. To ensure there is no leakage from the bottom of the mold on the cold-finger, a small amount of grease is applied on the bottom of the surface of the mold to glue the mold on the cold finger. The precautions are considered so there is no spread of grease inside the

mold, and even when transferring the suspension to the mold, so that no air bubbles get trapped within the suspension, which can cause defects in processed materials. During this stage, the Teflon mold is radially insulated using high-density polymeric foam to avoid any thermal gradient from the sides so that the suspension within the mold is subjected to only unidirectional freeze casting. The upper part of inner wall of the Dewar is also insulated to radial thermal gradient to the mold. The length of the freezing process varies within the range of 30-70 min depending on the ice-growth velocity. The time requirement of the unidirectional solidification of a ceramic suspension in the freeze casting process typically ranges from 30-60 min; preparation of well-dispersed aqueous suspension is important.

After completion of the freeze casting, the frozen sample was removed from the mold and stored in the refrigerator temporarily. Afterward the frozen samples were freeze-dried for 96 hours at low pressure (0.014 mbar) and temperature (-50°C). Next, the freeze dried samples were sintered in a box furnace using the following time temperature schedule: (i) heated from the room temperature to 450°C at a rate of 3°C/min and held for 4 hours for the binder burnout, (ii) heated from 450°C to 1550°C at a rate of 5°C /min and sintered for 4 hours, and (iii) finally cooled from sintering temperature to the room temperature at a rate of 5°C/min.

The below Fig. 5 is the representation of the sintering cycle for the samples. In this process the temperature is varied for periods of time to compact and form a solid mass of material by heat below its liquification point.

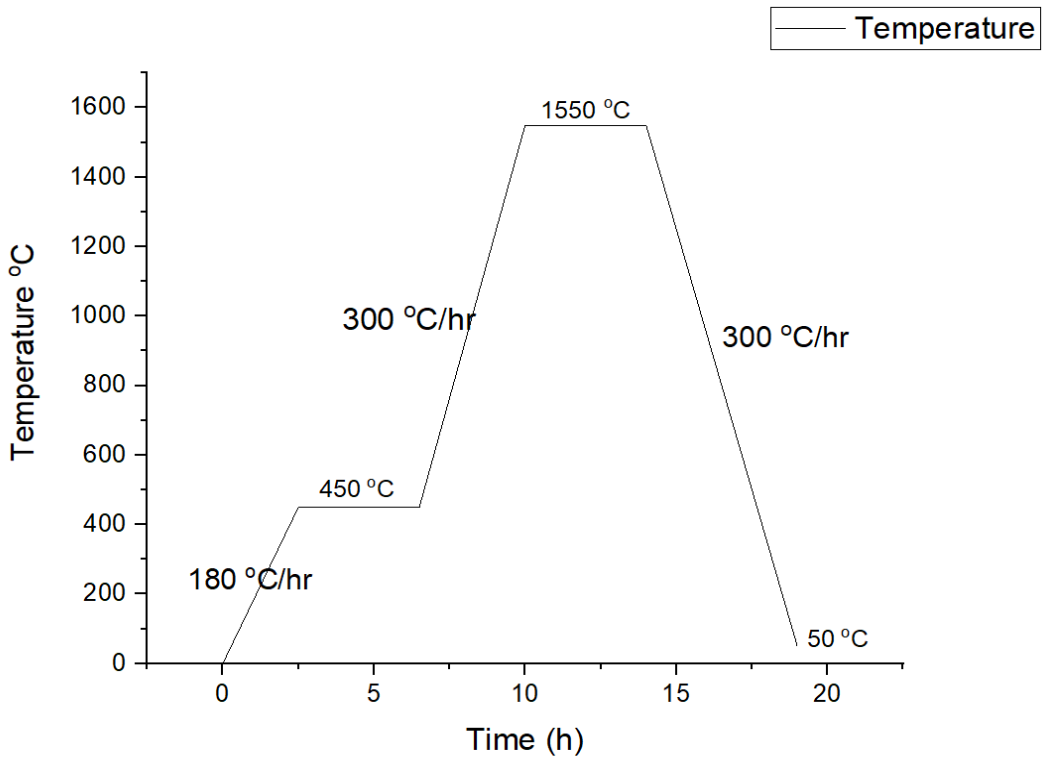

Figure 5 Schematic diagram of sintering regime for all the green samples

The above Fig. 5 is the representation of the sintering cycle for the samples. In this process the temperature is varied for periods of time to compact and form a solid mass of material by heat below its liquification point.

3.3 Manufacturing of Off-Axis Slabs

A waterjet was used to manufacture off-axis slabs of alumina. Waterjet is a generic term used to describe equipment that uses a high-pressure stream of water for cutting or cleaning purposes. Abrasive jet is a subcategory of the water jet in which an abrasive is introduced to accelerate the process. The ordinary tap water is pressurized and forced it through a small hole. In the case of the abrasive water jet, the garnet abrasive is mixed with water and a thin stream of water traveling very fast, which will rapidly erode most materials. Water jets can cut about any material that can be made into a sheet. Machining with waterjets has many advantages over other machining technologies [9]. The most important advantages are that no heat is generated in the work piece, there are low machining forces on the workpiece, machining of a wide range of materials is possible, and there are free contouring possibilities.

Aluminum oxide is an electric insulator but has a relatively high thermal conductivity for a ceramic material. Aluminum oxide is insoluble in water. For cutting alumina, advanced waterjet software is used; this software named ProtoMAX creates a space for personal drawing of the cutting operation. Initially the drawing is done in required geometric shapes to create a layout, and these layout files should be saved as DXF files. The cut qualities were assigned to drawing elements; it defines how fast the nozzle travels and determines the edge quality of the part. The slower the cutting speed, the smoother the cutting edge; the higher the cutting speed, the coarser the cutting edge. The layout contains all the tools to assigns the qualities for the geometries in the part. Next, the tool to clean up the drawing is opened; the clean tool automatically works with the geometries in the drawing to ensure there are no other gaps or other issues that will cause a problem for the machine. The last step in the layout is to add the path elements to machine tool path. The layout has automated pathing tools to make this process easy. The post tool

automatically converts the drawing file to tool path file and gives a chance to inspect or make corrections before proceeding for the cutting.

After creating the tool path file, that file is opened in the ProtoMAX MAKE. Then the material type and thickness are mentioned. Under the control of the ProtoMAX MAKE software the cutting nozzle follows the machine tool path using the drawings x and y coordinates. Prior to start the actual cutting of the part it is always good to do a dry run. Before preparing for the operation, lower the splashguard, raising the water level to keep noise and dust levels down and closing the lid.

Altogether there are three orientations which are machined using water jet. The 0^{o}, 15^{o} and 90^{o} orientations are measured in the ice-growth direction. Once the alumina slabs with different orientation are cut with the waterjet, individual sample cubes with dimensions of 6x6x6 mm^3. Next, to cut them into the required samples they were machined on the diamond saw. Materials are ensured to be cut in the middle of the large samples to ensure the homogenous density of the specimens by avoiding high-density gradients near the outer surfaces of the alumina samples.

Figure 6 Represents the water jet cutting system

Figure 7 Diamond saw cutting machine

After sintering, the samples are manufactured in the water jet cutting system as shown in the Fig. 6 in three different slabs. For cutting in definte shape and different off-axis loading samples the ProtoMAX software is advantageous. Then these slabs are futher manufactured into individvidual cubic samples on the diamond saw machine as shown in Fig. 7.

CHAPTER 4

Compressive response of alumina in different orientations

Experimental Results

The foams manufactured on a large scale, are used in packaging, crash protection, and lightweight materials. It is significant to understand the mechanical behavior of materials. The strength and fracture behavior are still important even when the primary use is not mechanical and when the foam is used for thermal insulation or flotation or as a filter. The elastic plastic like those of honeycomb structure show linear elasticity at low stresses followed by a long collapse plateau truncated by a regime of densification in which stress rises steeply [1].

When loading is compressive, the plateau region is associated with the collapse of the cells by elastic buckling in elastomeric foams by the formation of plastic hinges in a foam which yields and by brittle crushing in a brittle foam. Increasing the relative density of the foam increases Youngs modulus, raises the plateau stress, and reduces the strain at which densification starts. Uniaxial compression testing is valuable to optimize critical yield properties of alumina, and accurate determination of strain behavior is necessary to advance the performance of the material.

Digital image correlation (DIC) provided a non-contact method to analyze surface strains of material properties under deformation and compliments traditional measurement. DIC was particularly useful for analyzing compression specimens of cylindrical samples due to edge effects associated with shadowing and pixel mapping. Image sections, typically edges that did not display optimum contrast due to shadows or low light artifacts were eliminated to enhance

DIC analysis. Facets, defined by pixel size and step length, were generated in grid patterns across the optimized areas of the digital images. Facet size is the true dimension of the defined area in pixels. Step length is the distance between adjacent facet centers, with smaller steps leading to increased spatial resolution. Upon facet definition, a start point was defined for the initial image set. The start point provides a reference for the software to recreate the initial facet field on subsequent image sets to quantify three-dimensional strains. During computer computation, the gray scale speckle pattern is tracked within each rectangular facet from image to image. A three-dimensional gradient tensor field is calculated to create strain distribution profiles capable of displaying both major and minor strain of specimen during loading.

4.1 0-Degree Off-Axis Loading: Uniaxial compressive Response

Computer models have achieved great predictive power, but without precise material properties, the models will never fulfill their accurate modeling potential. Understanding the complex response of materials in order to fully understand their properties is critical for the refinement of design and manufacturing with all materials. 3D Digital Image correlation (DIC) provides full field 3D deformation and strain measurement, allowing for more complete understanding of complex material responses.

All in a fraction of time it reduces the need for mechanical gauges and greatly increases the quality and quantity of the data collected. Forming verification with optical metrology, directly comparing against the engineering FEA computer model of stamping and hydroforms, gives manufacturing direct control of its operations with better data.

The standard material properties testing for alumina includes compression test. It is suited for 3-D image correlation method. Providing measurement abilities is not possible with traditional methods. The method becomes critical in anisotropic materials such as composites to biomaterials, where the single point or average measurements means very little. The ARAMIS system connects to the testing machine reading the load and displacement of crosshead and its data collection is fully programmable. ARAMIS then tracks these points throughout the test, so their complex 3D deformations and strains are measured, calculating the true strain tensor for every point.

Compression tests procedures followed on Tinus Olsen 10kN load. Now the manufactured square samples from the cutting machine are placed between the platens. The geometry measurements of sample were defined as input to provide the for accurate results. Before proceeding, the compression tests the mode of method of compression test selected. The

parameter of shape selection is mentioned as square where the entries are given in terms of the length and width. To ensure the platens don't move during the running the experiment initial pre-load is applied. The square samples manufactured were compressed at a displacement rate of 0.5mm/min. Now the stress values are tabulated from the Load Vs Time graph recorded in the software provided by Tinus Olsen. Compression strain values were recorded simultaneously using digital image correlation methods.

The formulae used to tabulate the stress and strain are as follows:

$$F_t = F/t$$

where

F_t is the force rate N/s

F is the applied in Newtons

T is the time in seconds

The strain rate ε_t is given by

$$\varepsilon_t = \varepsilon/t$$

where

ε is the strain recorded by DIC system.

t is the time in seconds.

The stress σ is given by

$$\sigma = F/A$$

where

F is the force applied in Newtons

A is the cross-sectional area

The modulus E is given by

$$E = F_t/\varepsilon_t$$

where

F_t is the force rate N/s

ε_t is the strain rate

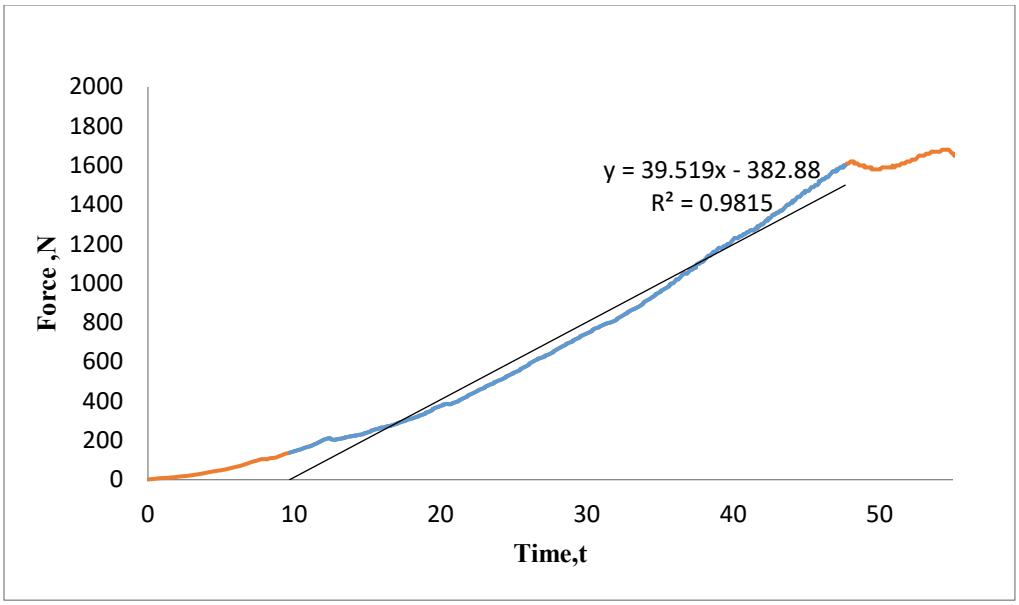

Figure 8: Represents load - time in off-axis loading which the samples are manufactured at zero degree.

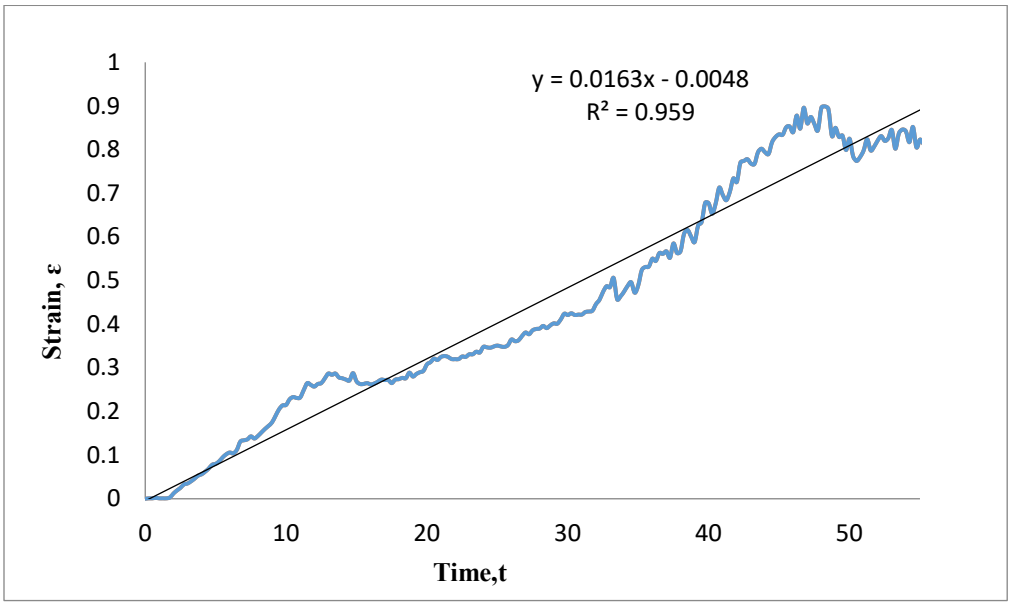

Figure 9: The above plot represents the average strain -time which is displayed in frames from the digital image correlation system.

The load in Newtons is plotted against the time in seconds; the trend is observed for the sample manufactured in the zero degree off axis modulus shown in Fig 8. When the sample is compressed quasi-statically, the maximum load till the breakage of the sample is 1600N. The linearity of the sample gives us the elastic limit and slope of it gives us the load rate. The optical measurement system helps to record the vertical displacement under compression where the data is plotted in the Fig 9. with respect to time. The calculation of the modulus value is further measured in synchronous with time period of load and strain.

Fig. 10 represents the initial pattern formation after thorough calibration when the pre-load is applied in the ice-growth direction which we also refer to as zero-degree orientation. The strain measurements are recorded where the pattern deformation is observed in Fig. 11. The different colors on the pattern represent the strain concentration values. Similar steps were followed to record the strain measurements in the y-direction, which were represented in Fig. 12 and Fig. 13. After, the several steps of calibration to capture the optimized pattern to record the strain values from the DIC system. The shape of the adequate sample shape to be used for identification of the material parameters starting from the force-time curve. The x-components and the y-components values are useful in finding out the Poison's ratio in the loading direction. Progressive crushing of the sample can be observed in Fig. 11-13.

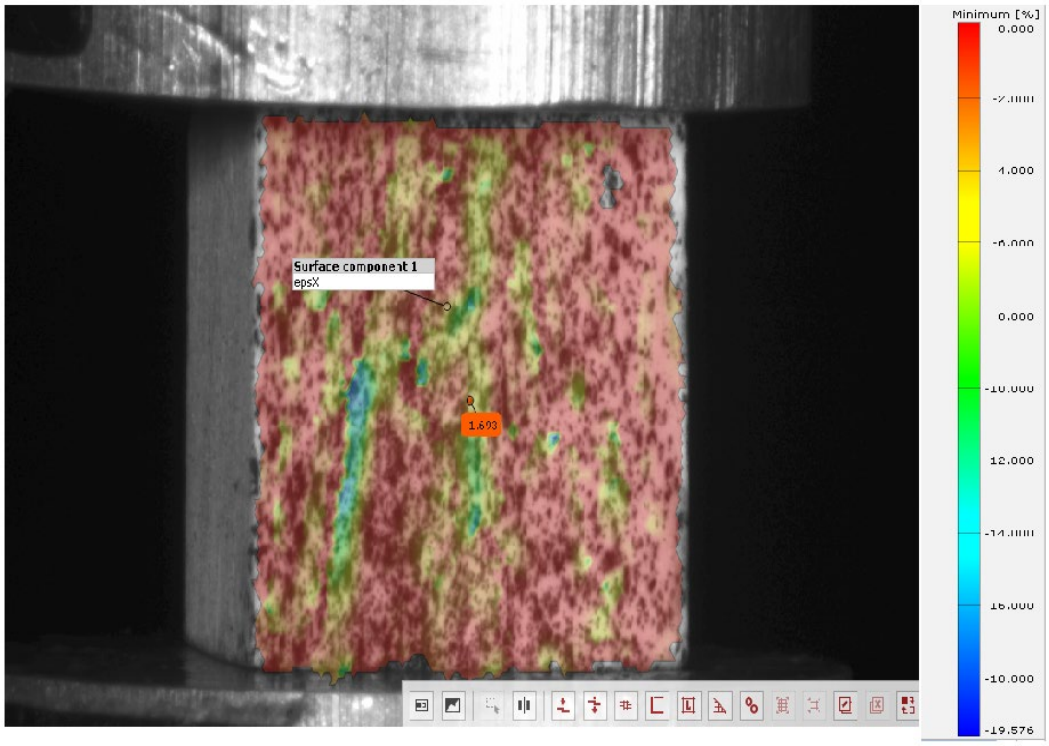

Figure 10 Initial pattern image in x-direction when pre-load is applied on to the manufactured square sample in the ice growth direction

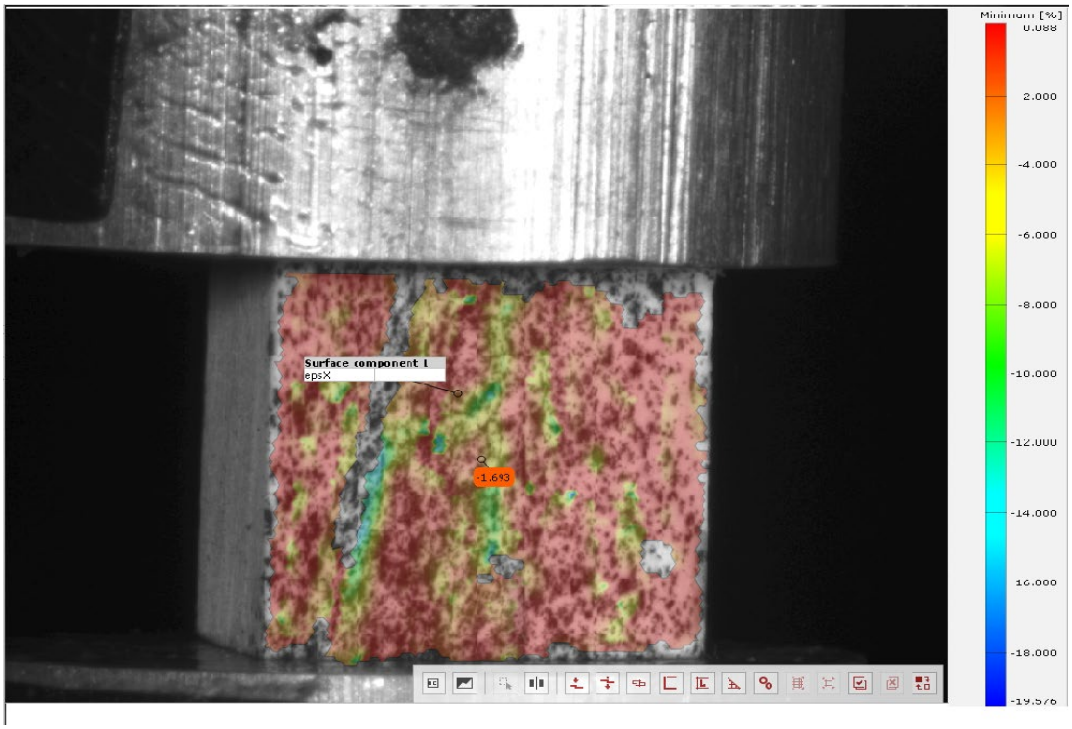

Figure 11 Strain measurements are recorded by the DIC system in x direction under compressive loading.

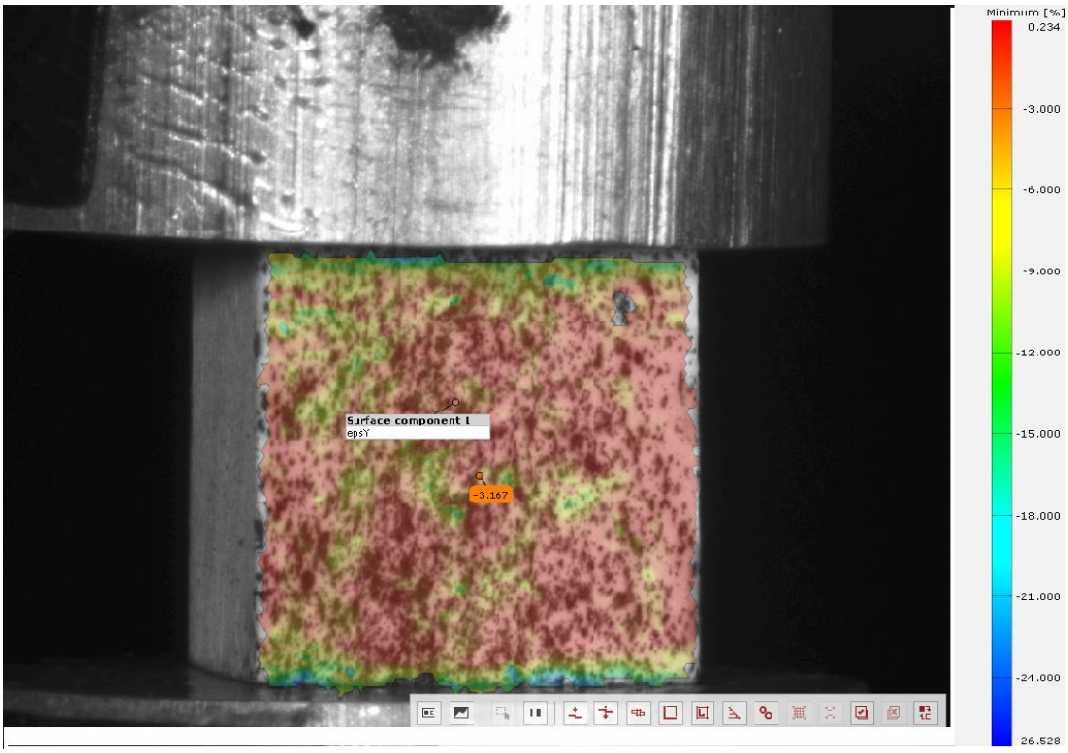

Figure 12 Initial pattern surface component formed where the pre-load is applied in the y-direction.

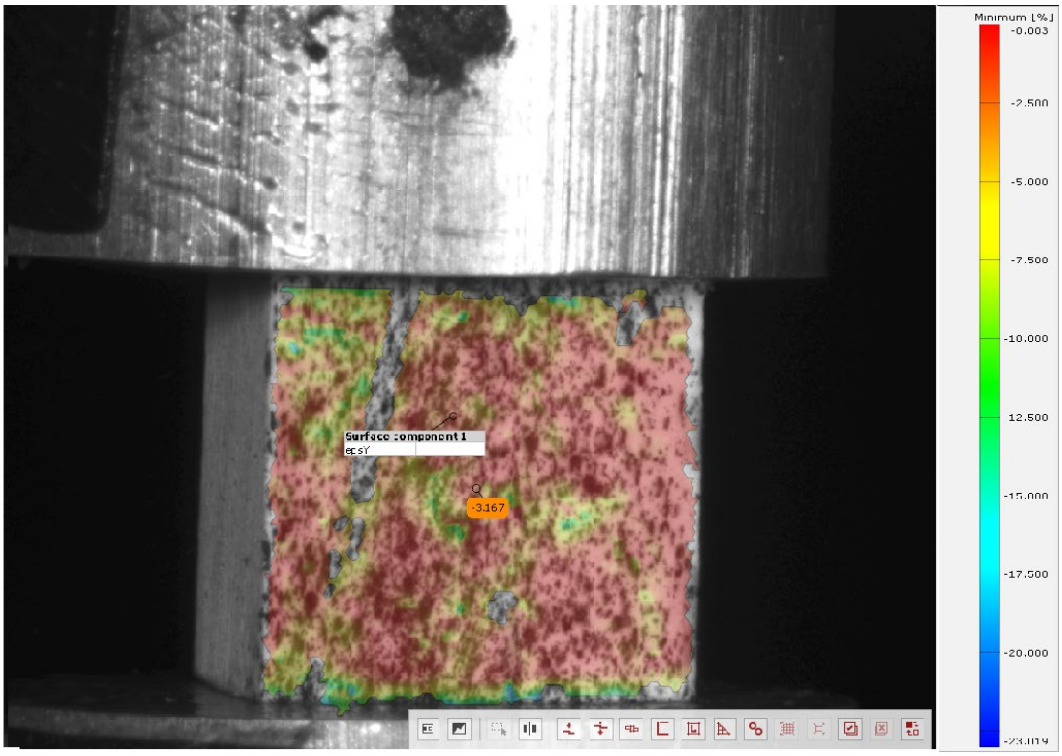

Figure 13 Strain values are recorded in y-direction by the DIC system under compression load

Results exhibited the minimum value for the sample manufactured in zero-degree off axis loading, plotted in the Fig 14-15, where the load rate and strain rate are calculated from the beginning of the load to the elastic limit that the sample resist to deform for the applied load. We can observe the force rates and strain rates for tools provided by the compression test machine and DIC system to further calculate Poisson's ratio. From the Fig. 13 we can observe the pattern formed by the camera system deforms in the ice growth direction when the load is applied. The breakage of the sample is observed till 1% strain and the stress concentration values are observed on the stress contour.

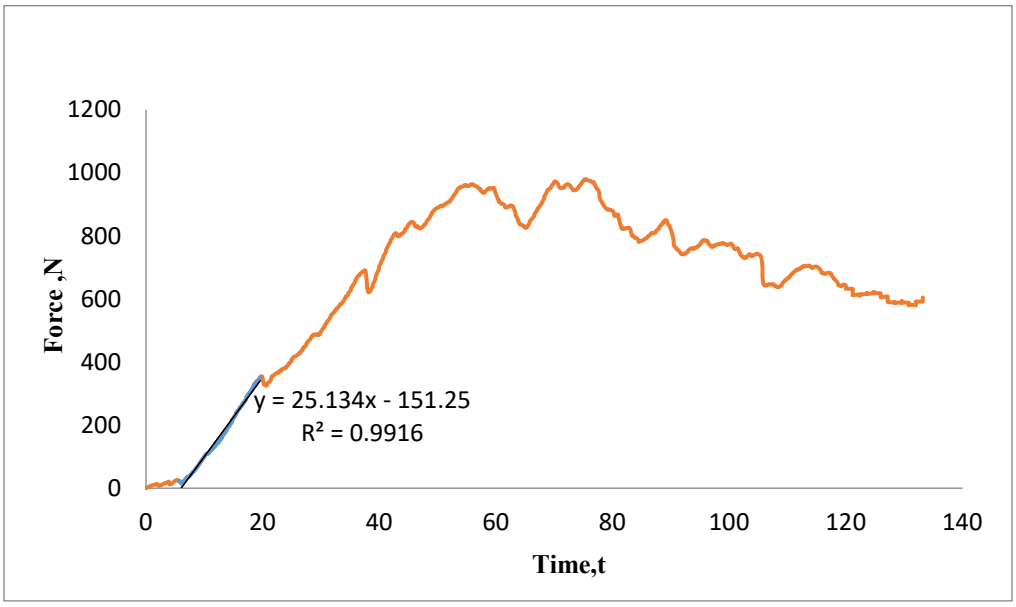

Figure 14 The above plot represents the manufactured sample at zero degrees with minimum stress under compressive load.

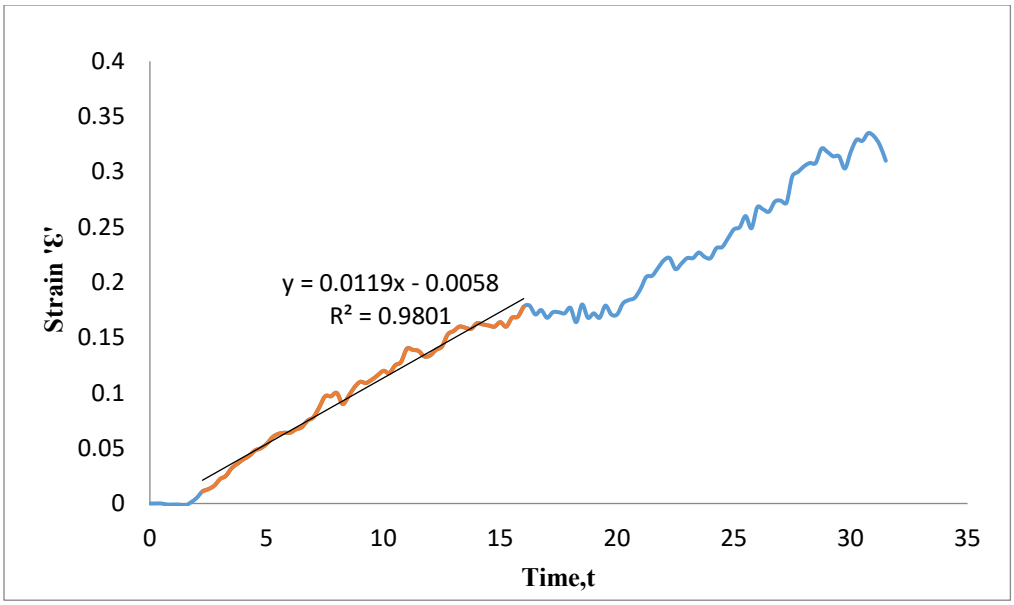

Figure 15 Strain-time of the sample which shows minimum stress under compressive response.

Fig. 16 and Fig. 17 represent the initial pattern formation when the pre-load is applied in the x-direction and y-direction. The different colors on the pattern represent the strain concentration values and the point-wise inspection can be done with deviation labels. When the quasi-static load is applied in the y-direction the crushing of the sample is observed on the top parallelly the strain measurements are recorded in the x-direction upon when the sample reaches around the 1.5% strain shown in Fig 17. Similarly, the following measurement are recorded in the y-direction shown in Fig. 19 which are useful in find the Modulus and the Poison's ratio.

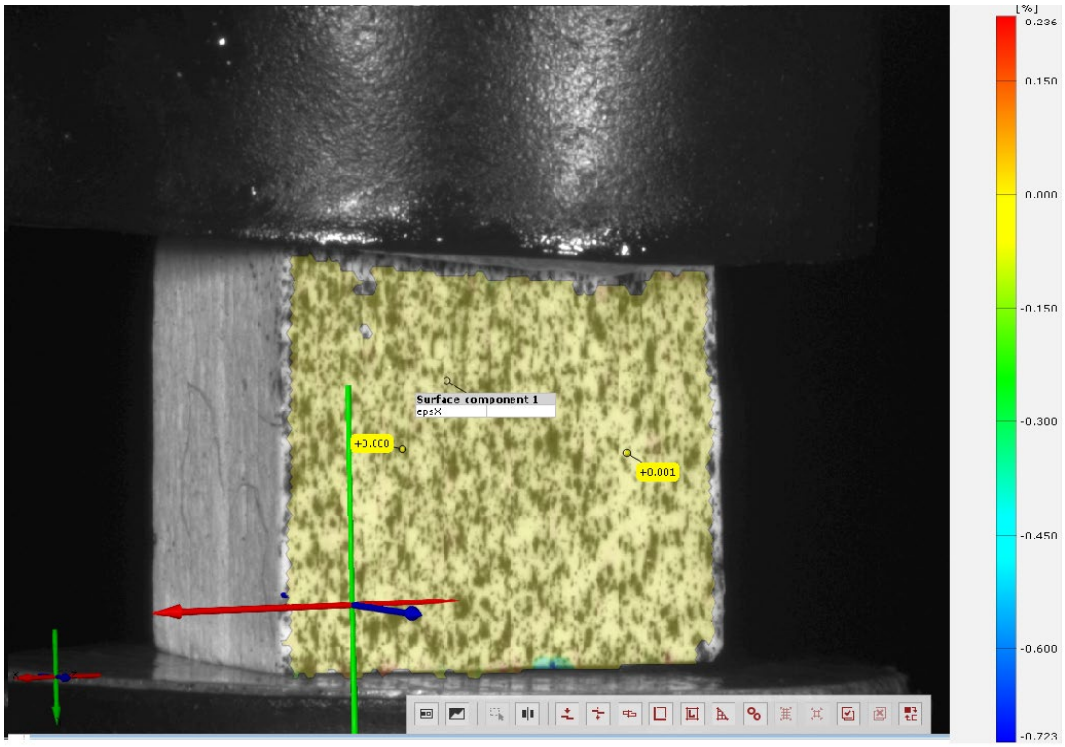

Figure 16 The initial pattern formation captured at zero sec when the preload is applied on the sample.

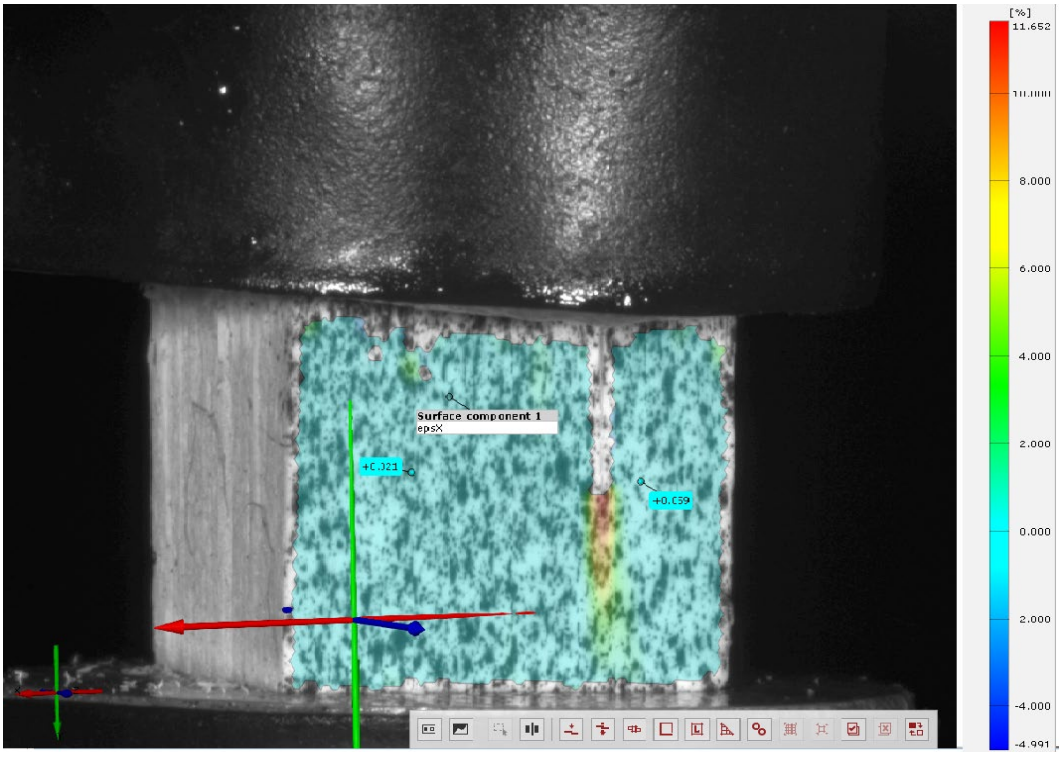

Figure 17 Displacement recorded image at time period 55 sec by the DIC system.

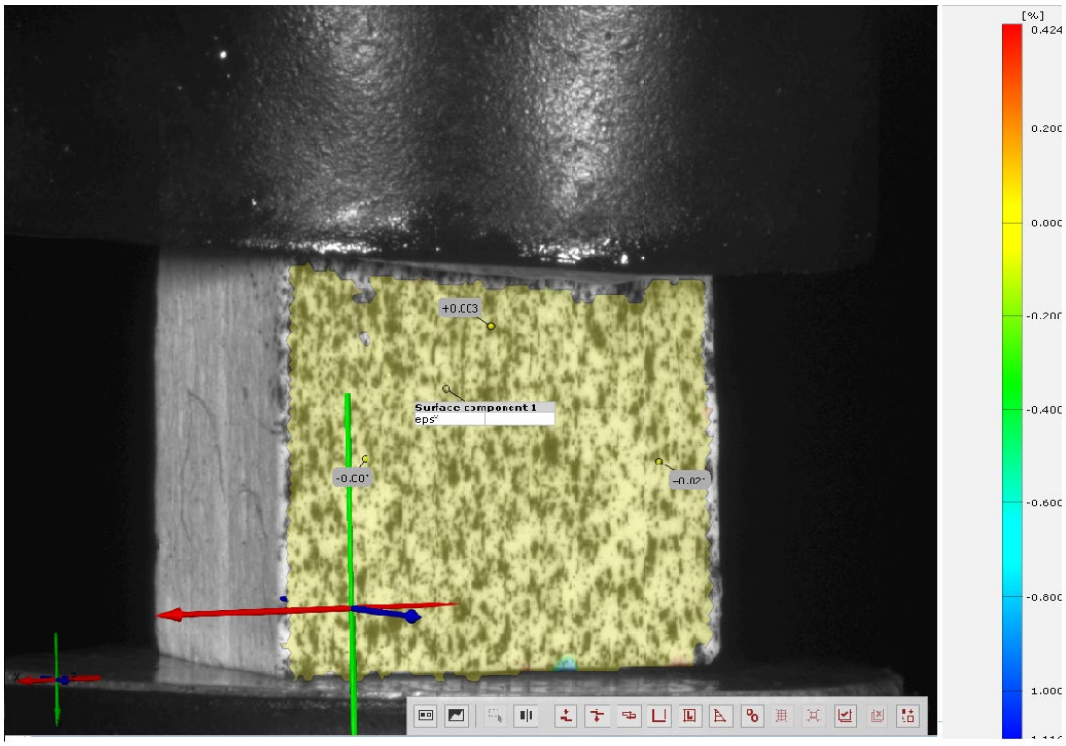

Figure 18 The initial pattern image when the pre-load is applied in the y-direction.

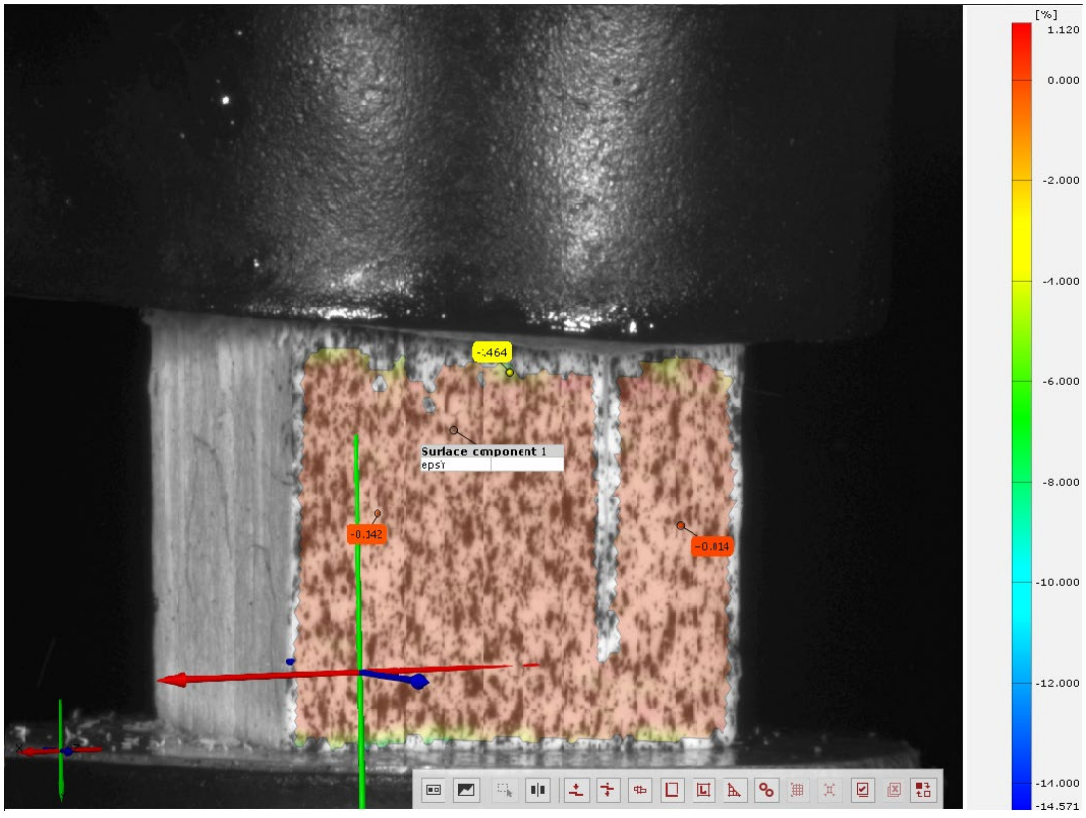

Figure 19 The strain values are recorded in this image at 55 sec in the y-direction

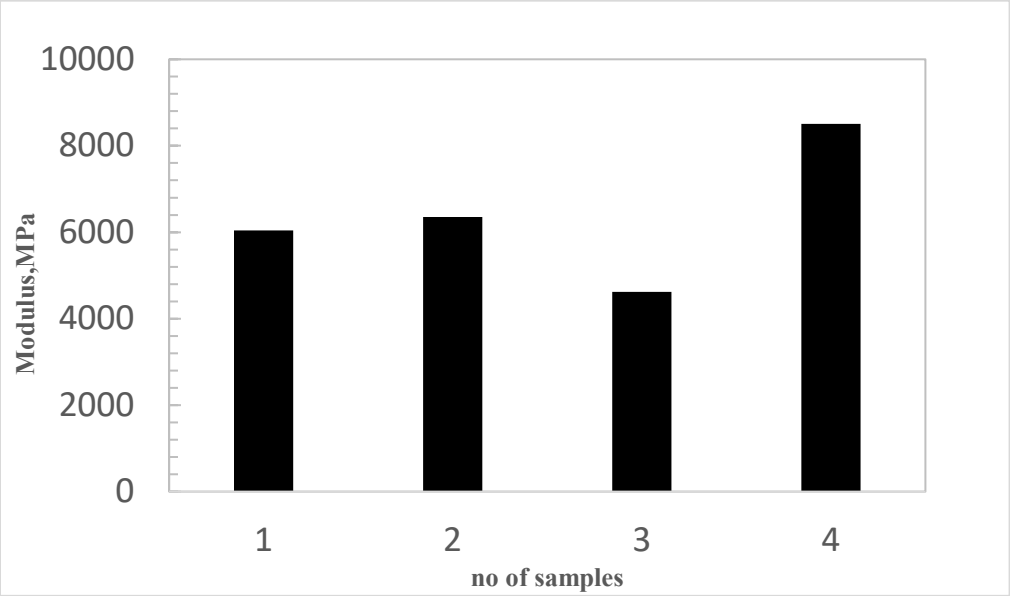

Figure 20 Modulus graph for all the tested samples loaded in orientation

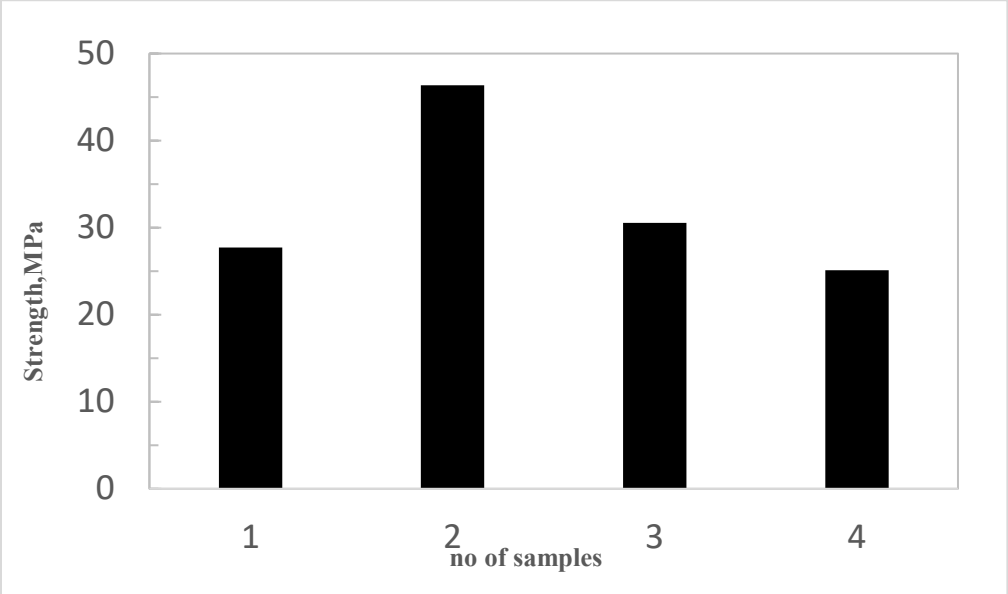

Figure 21 Compressive strength represented for all the tested samples loaded in orientation

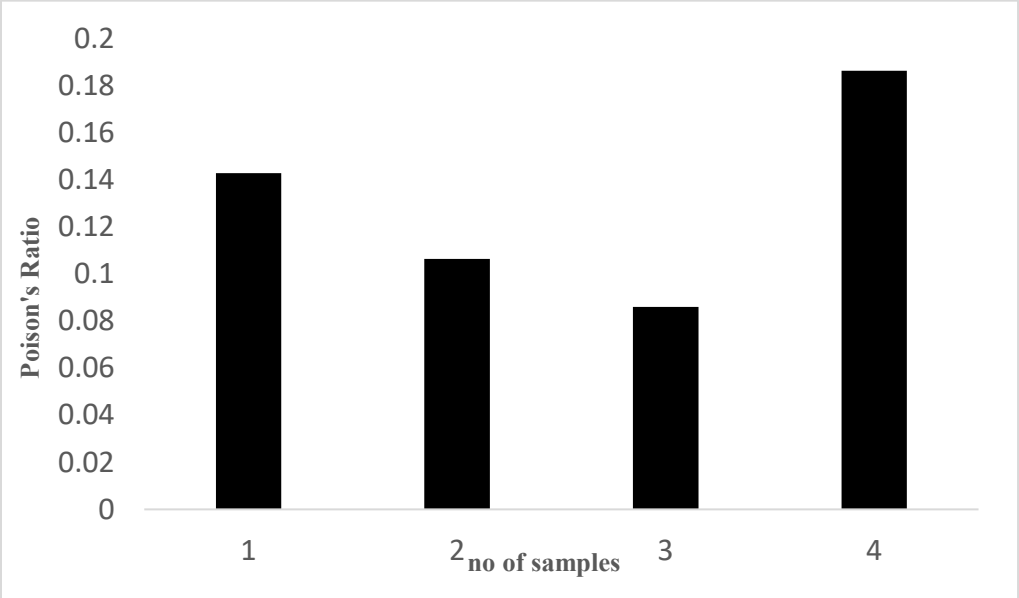

Figure 22 Ratio of lateral strain to the longitudinal strain of the tested samples loaded in orientaion

Fig. 20 represents Modulus values for all the tested samples in the zero-degree off-axis loading. Now from the load rate and strain rate with respective measured sample surface area we plotted the strength values in the Fig. 21. From the DIC system the strain values in x and y direction where the sample recorded to find out the Poison's ratio of all the samples in the Fig. 22. The average Modulus of the tested samples is $\overline{E} = 6382.32 \pm 1603.91\, MPa$. The average stress value is $\overline{[\sigma]} = 32.43 \pm 9.54\, MPa$. The Poison's ratio is the ratio of lateral strain and the longitudinal strain and the average Poison's ratio of compressed samples is $\nu_{12} = 0.122 \pm 0.042$.

4.2 15 - Degree Off-axis Loading: Uniaxial Compressive Response

The loading direction is varied from being directly in line with the ceramic axis to normal to the sample axis. Off-axis testing is therefore a straightforward technique that can be used to characterize a wide range of properties the ceramics. The off-axis test is particularly useful since it assesses the ability of the composite to preserve its properties when it is not loaded in the optimum ceramic direction. Understanding the manner in which the properties degrade as the loading conditions vary is an essential requirement in the practical use of anisotropic ceramics.

It is clearly evident that values of 15-degree off-axis loading differ from the 0-degree off-axis loading. The material parameters are measured from the force-time curve and strain-time curve for the same time period as shown in Fig. 23 and Fig. 24. The frequency of the image processing is 4Hz for recording the measurement data in both x and y direction. Interestingly the image frames reveal that initially the stress concentrations occur on top and bottom of the sample shown in Fig. 26 and Fig. 28. Further the crushing of the sample occurs in the direction of the off-axis loading.

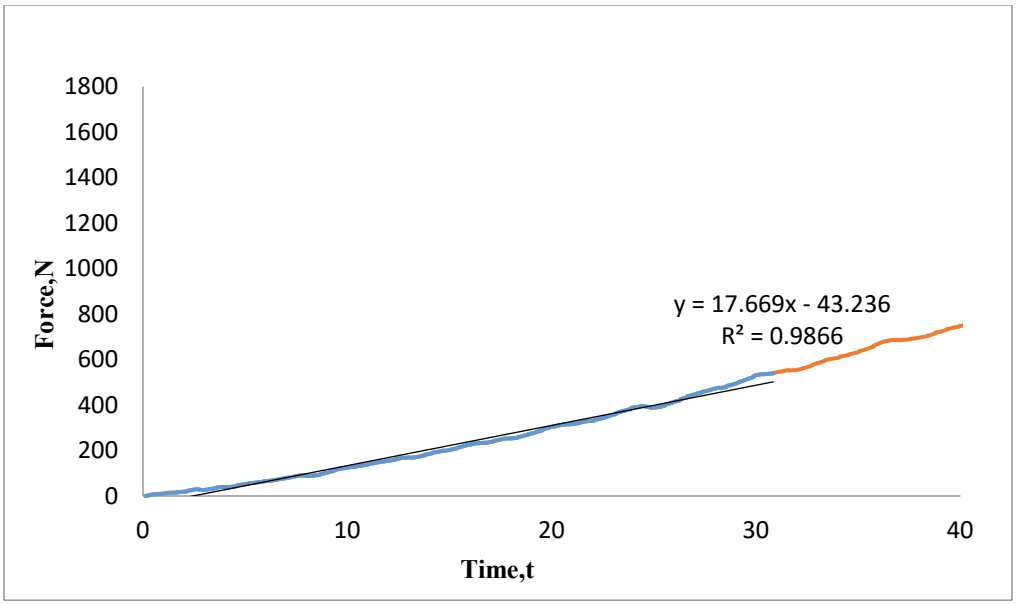

Figure 23 Compressive response of 15-degree manufactured slab which displays maximum load of all tested samples.

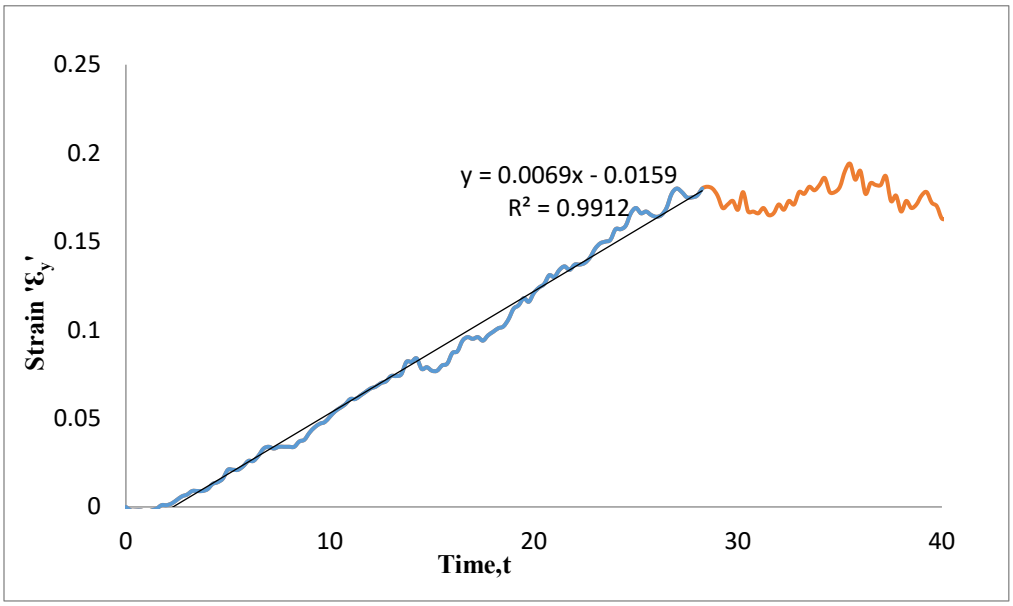

Figure 24 Strain-Time of a 15-degree manufactured slab which displays maximum load for tested samples.

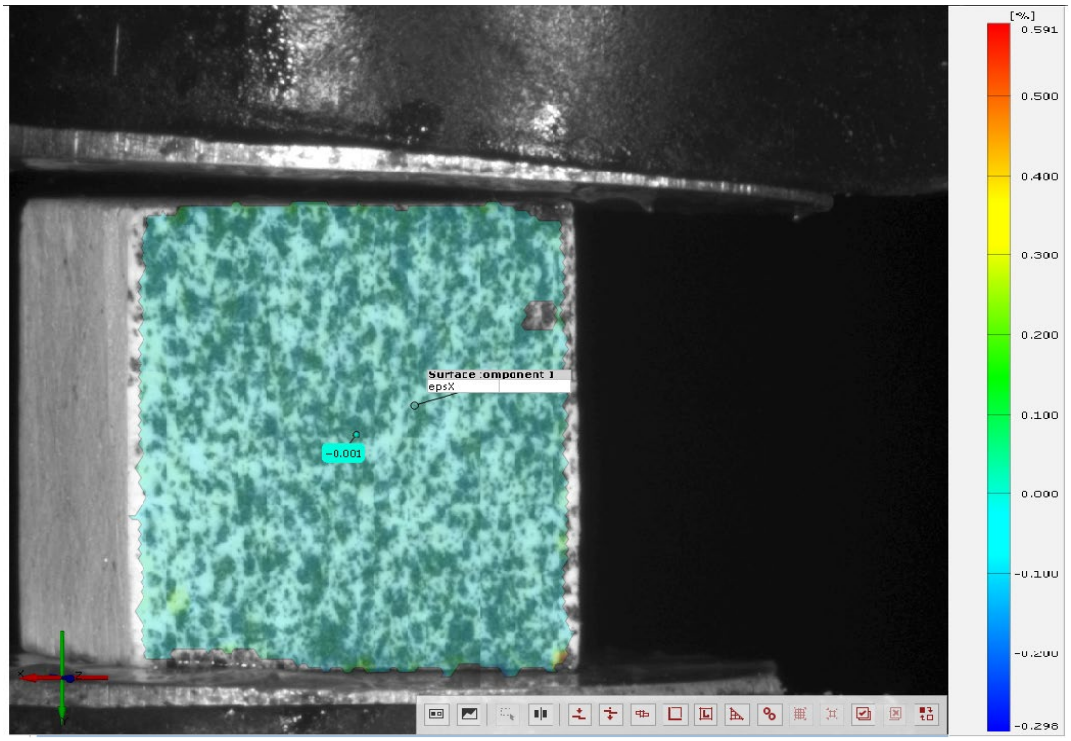

Figure 25 Initial pattern formation image for the 15-degree orientation in the x-direction.

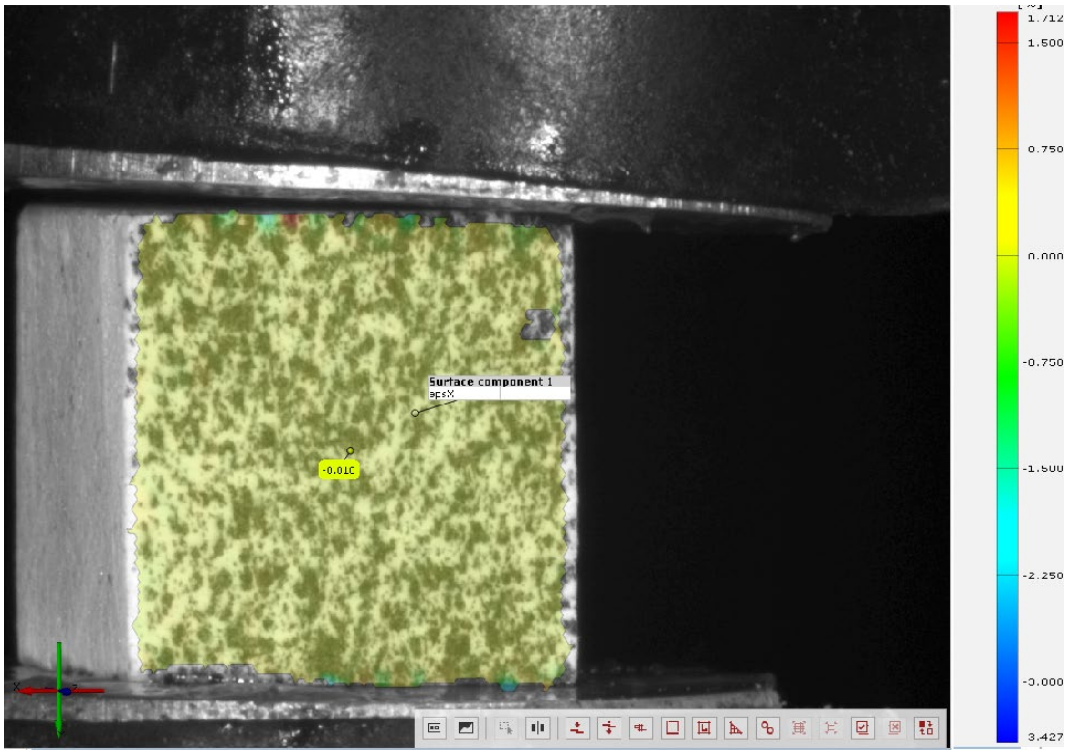

Figure 26 Strain recordings image at 35th sec of x-component under compressive load for 15-degree orientation

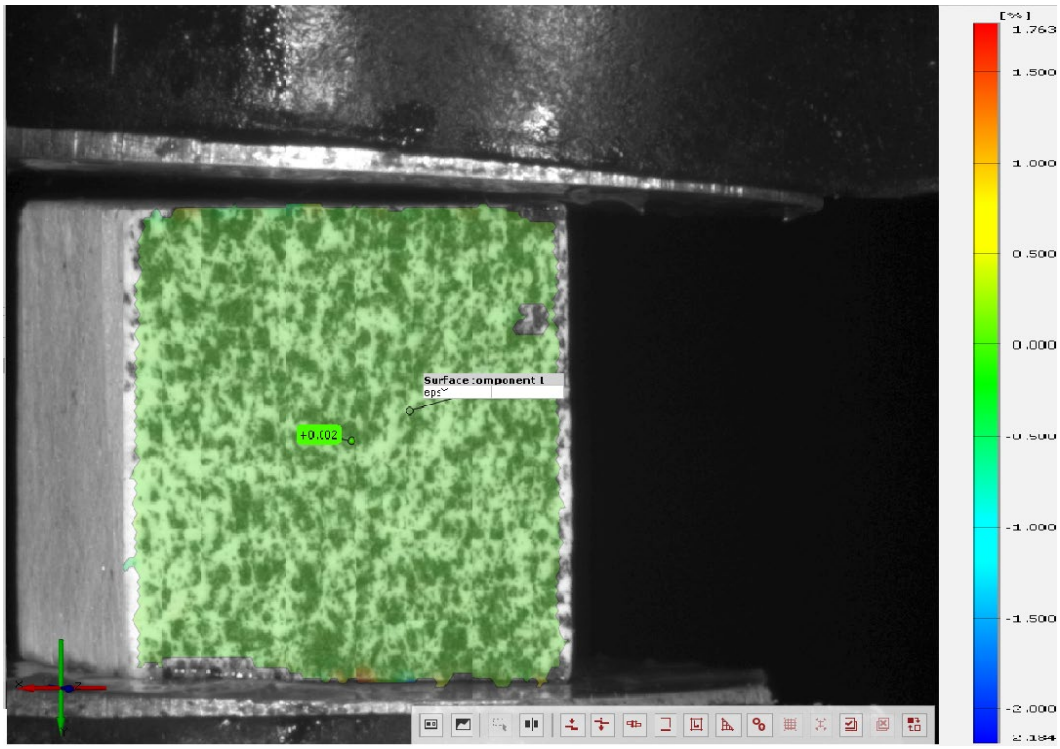

Figure 27 Initial surface component image in the y-direction when pre-load is applied.

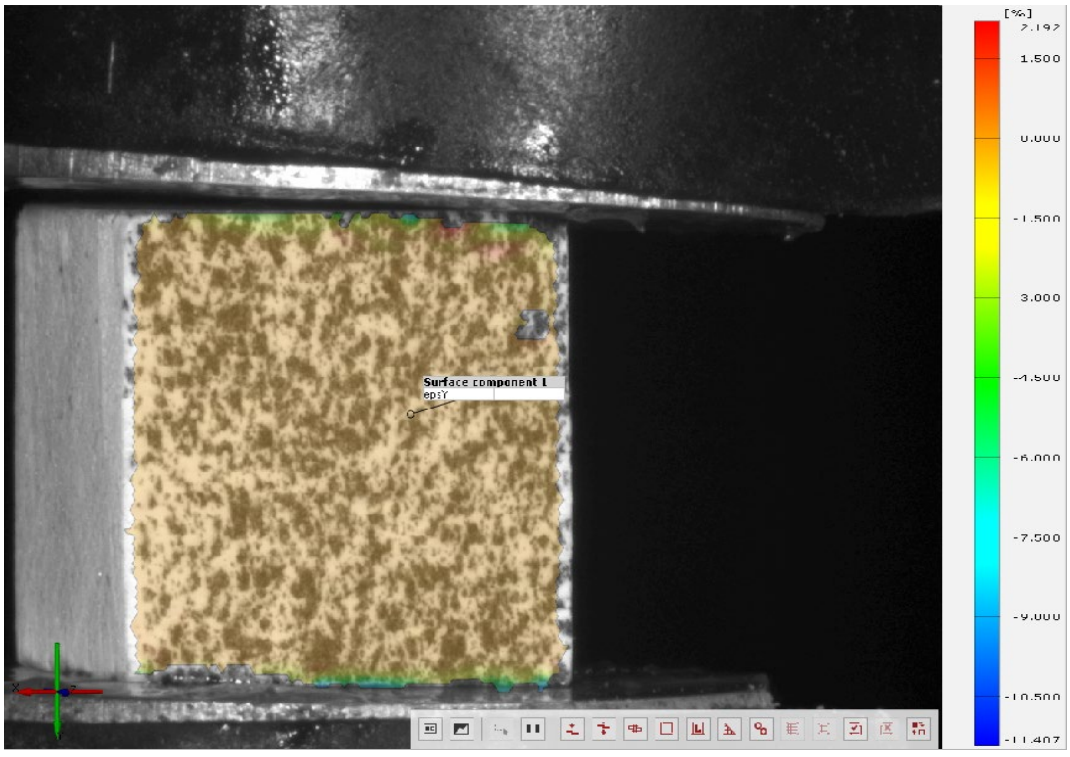

Figure 28 The strain value recorded at 35th sec in the y-component for 15-degree orientation.

The displacement measurements are introduced through digital image correlation. The stiffness is measured from the force-time and strain-time from Fig. 29-30. The load data is collected from the Tinus Olsen and the strain data is recorded in the DIC system. The below samples are for the minimum value sample. The initial pattern images are formed by the DIC system for the both x and y component when the pre-load is applied. The frequency at which all the strain measurements are recorded is 4Hz. We can observe how the manufactured sample deforms when the load is applied. There is an interesting difference when the compressive load is applied unidirectionally the zero-degree orientation deformation appears to in the middle of the sample whereas for the fifteen-degree orientation it is observed the shearing happens and deformation happens in the side walls, which is evident from the Fig. 32-34. It is very clear for the minimum value sample when the image pattern deforms in the direction of the manufactured off-axis loading.

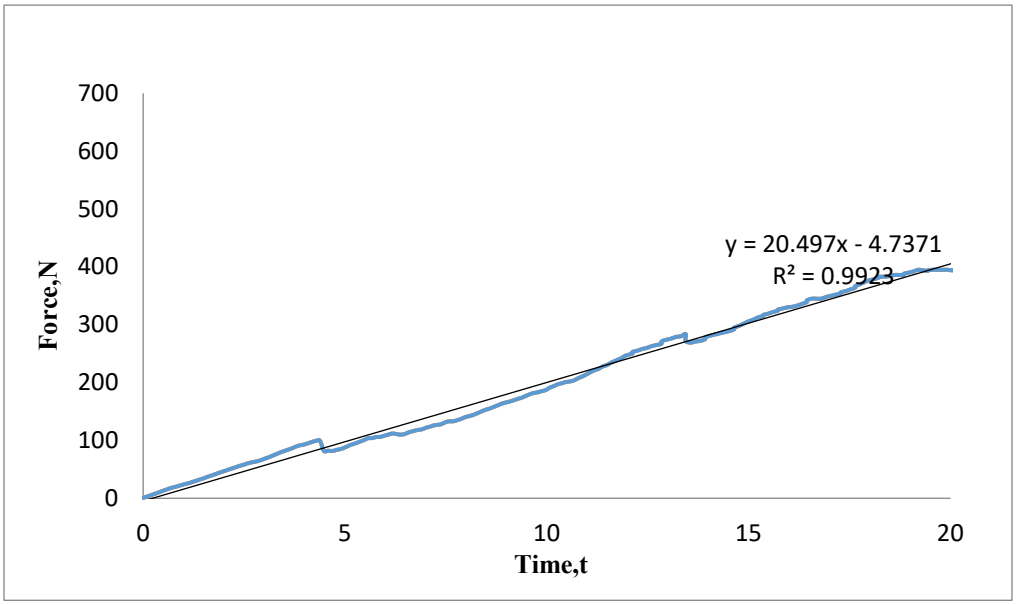

Figure 29 The compressive load response with respective time is plotted for a minimum strength sample of a 15-degree off-axis loading.

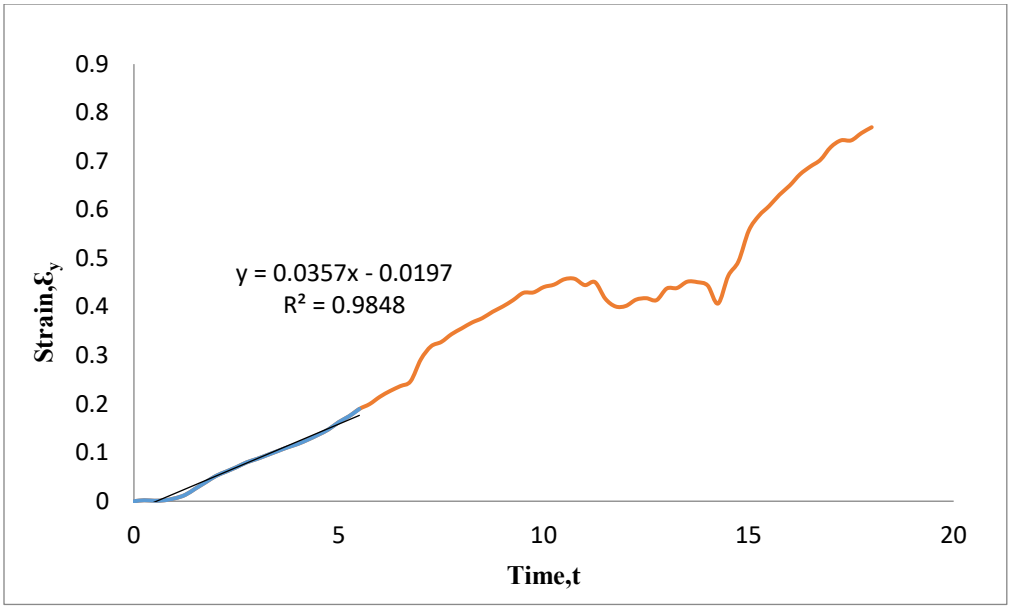

Figure 30 Strain with respective time is plotted for a minimum strength sample for 15-degree orientation

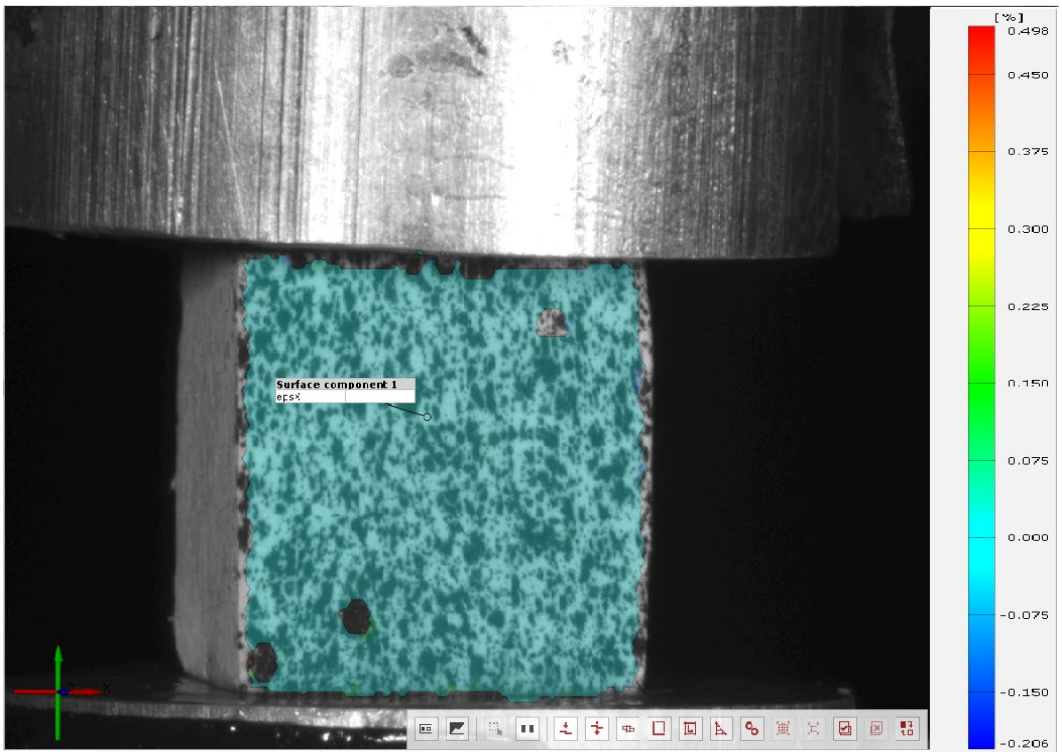

Figure 31 Initial pattern formation for the minimum value sample in the 15-degree orientation.

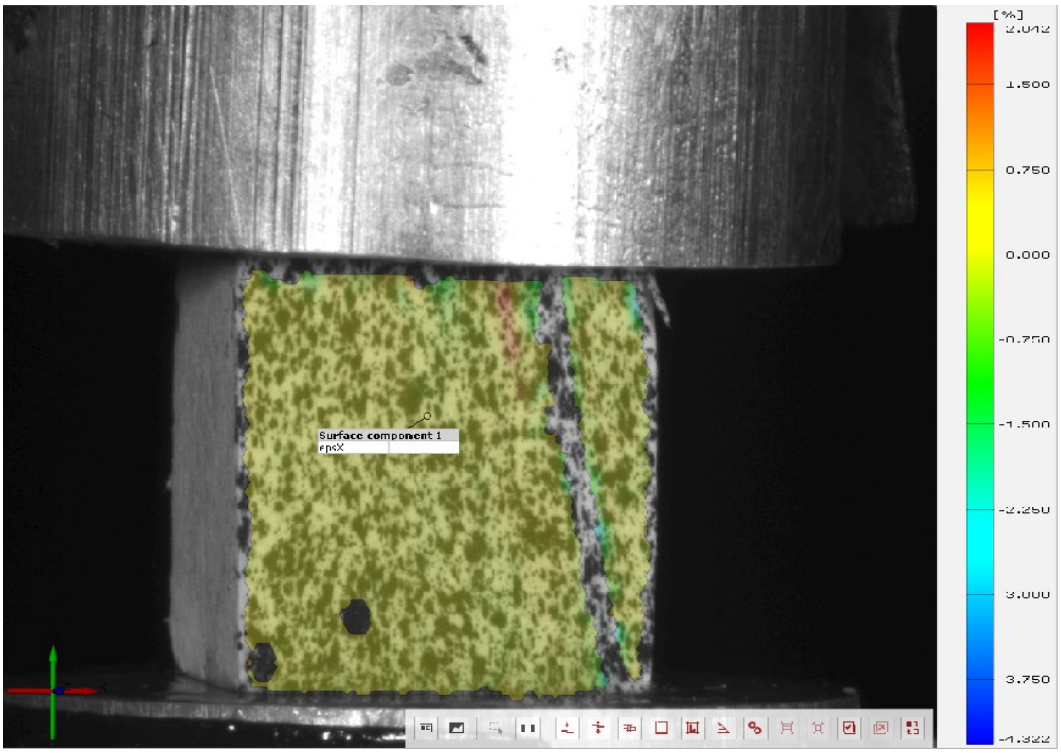

Figure 32 Strain measurements recorded at 20th sec as the sample deforms in the x direction

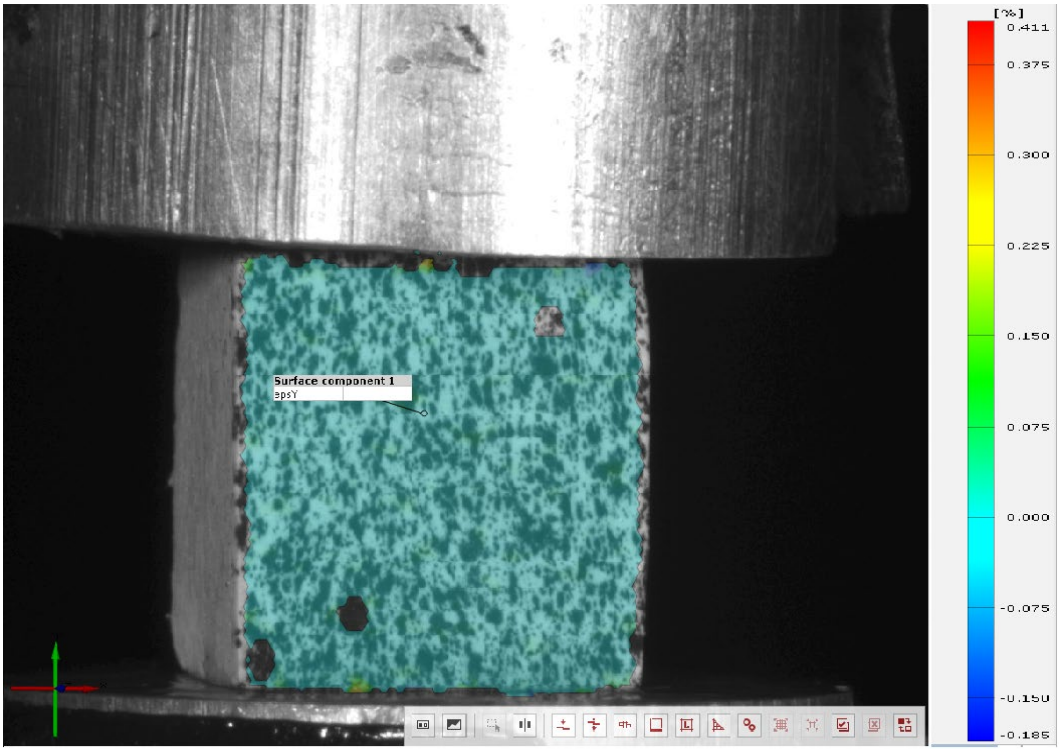

Figure 33 Initial surface component formation for the minimum value sample in 15-degree off-axis loading

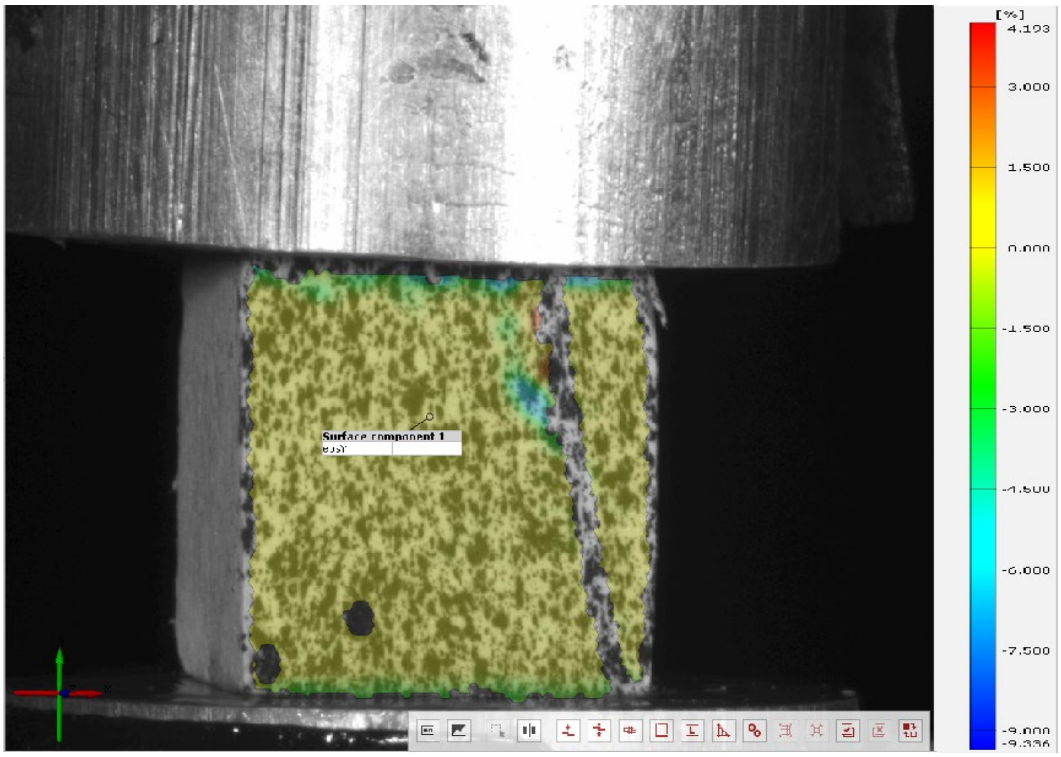

Figure 34 Strain recordings by DIC system at 15th sec for manufactured sample in the 15-degree off-axis loading.

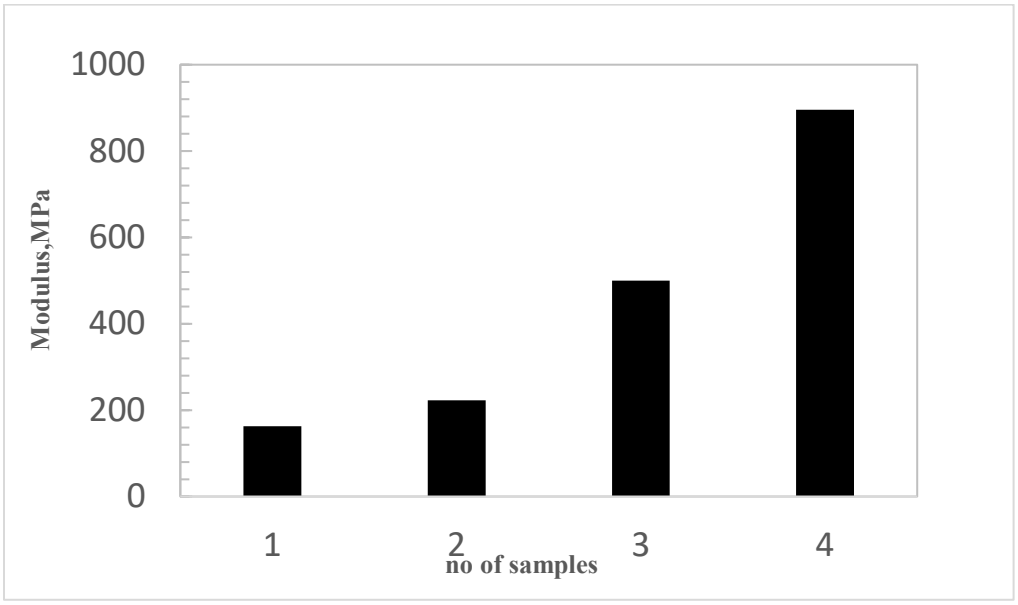

Figure 35 Modulus data of compressed samples for 15-degree off-axis loading.

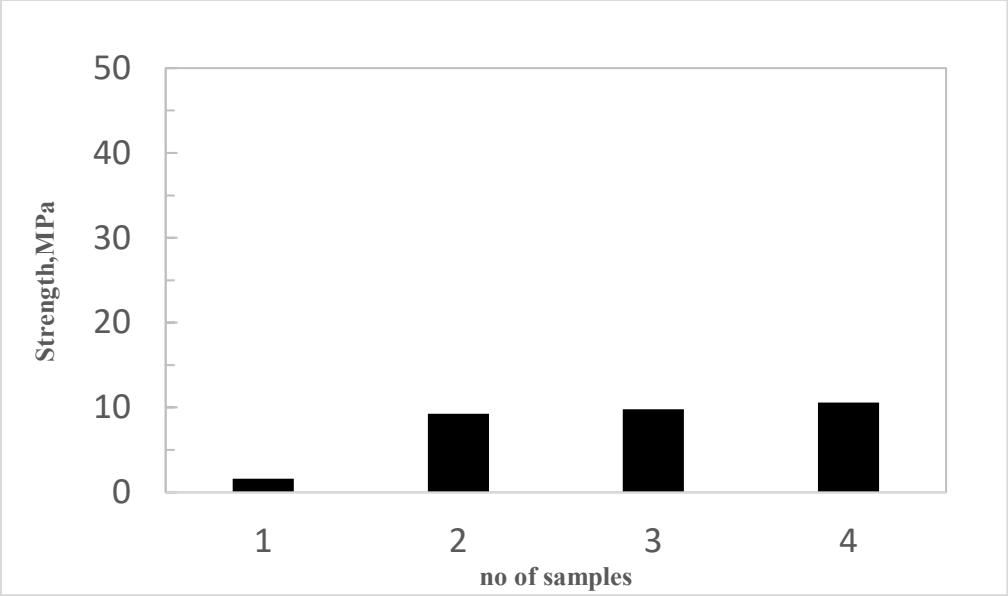

Figure 36 Compressive strength of the samples tested for 15-degree off-axis loading

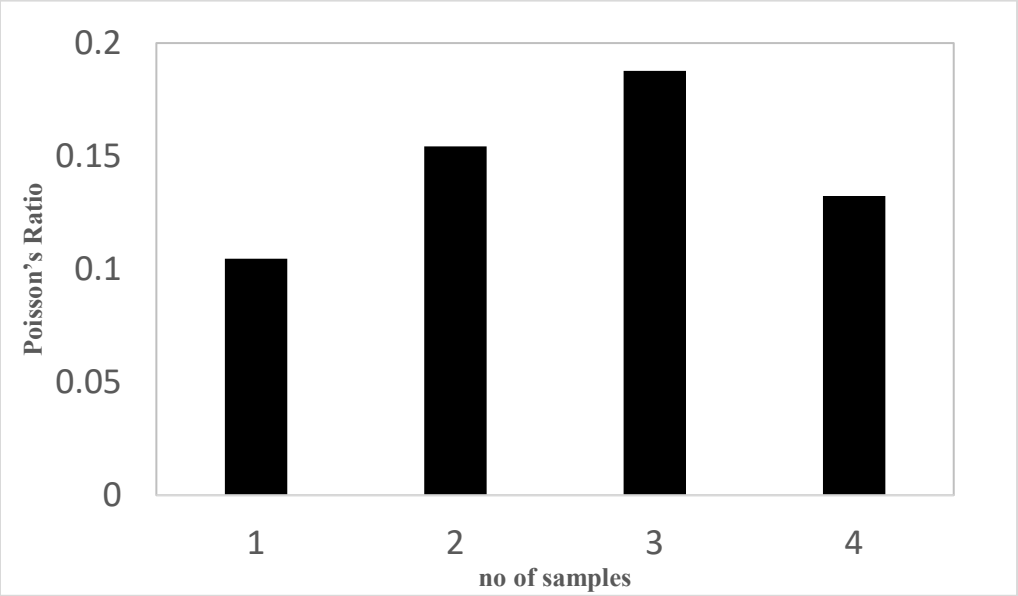

Figure 37 Strain measurements recorded from the DIC to determine the poison's ratio for 15 degree off-axis loading.

Fig. 35-37 represent the Modulus, Strength, and the Poison's ratio values for all the tested samples in 15-degree off-axis loading. The average modulus of the 15-degree off-axis loading samples is $\overline{E} = 4419.934 \pm 1468.86MPa$. The average stress value of the 15 degree off-axis loading is $\overline{[\sigma]} = 23.809 \pm 8.688MPa$. The Poison's ratio is defined as the lateral strain by the longitudinal strain where the average value of the compressed sample is $\nu_{12} = 0.1477 \pm 0.035$.

4.3 90 – Degree Off-axis Loading: Uniaxial Compressive Response

We applied this photogrammetry technique to calculate the square alumina samples throughout the compression-loading test to determine the actual cross section area with time. The speckled pattern after the calibration proceeded through the DIC system to form the surface component and during experiment deviation of the surface component is observed.

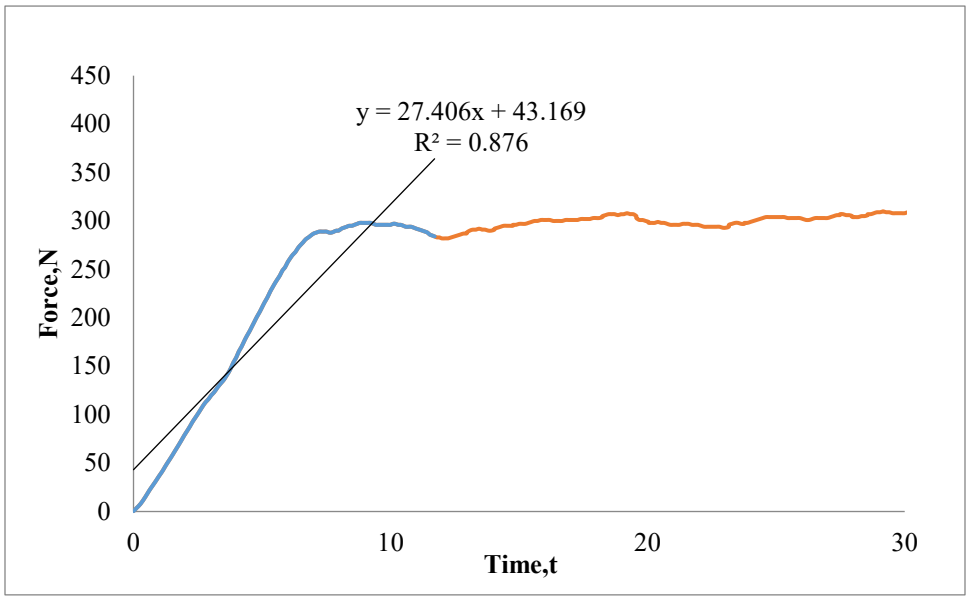

Figure 38 Force-Time of compressed sample represents the values for 90-degree orientation

The load with respective time is mapped in the above Fig. 38; it is seen during the tests of compression it first deforms in a linear-elastic way, then the sample breaks to give linear elasticity finally as the load increases as the faces and edges are forced together. The strains displacements are measured with respective time from the digital image correlation in the Fig. 39. The initial pattern formation while computing both x and y directions are shown in the Fig.

40 and Fig. 42. The loads are applied perpendicular to the ice-growth direction, which the sample start to break from the bottom of the sample as shown in Fig. 41 and Fig. 43.

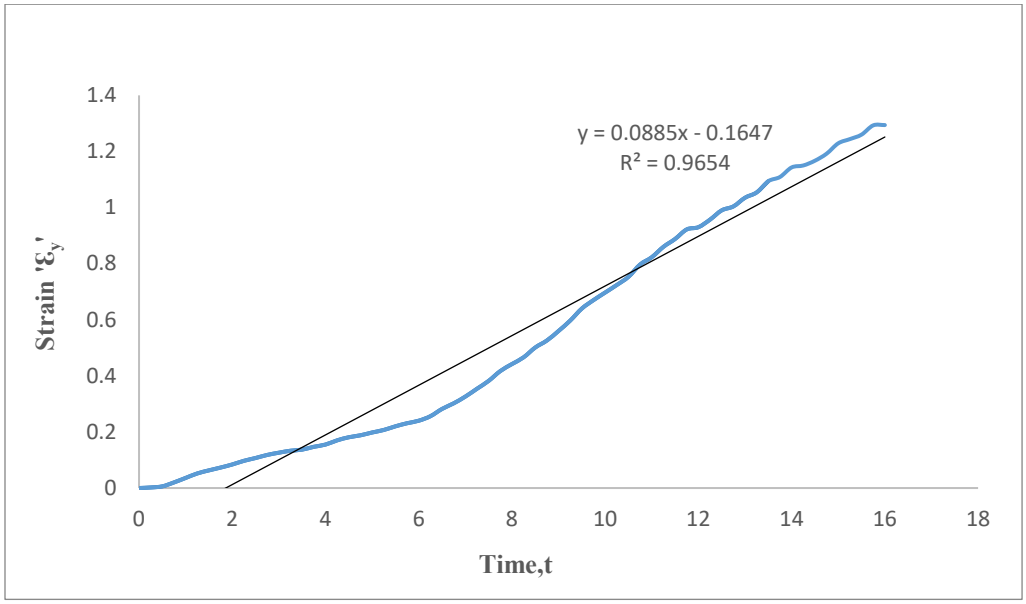

Figure 39 Strain with respective time is plotted for the 90-degree orientation compression tested samples

The load rates and strain rates are synchronized by considering the values for same time period. The maximum load for the 90 degree off-axis loading sample is almost 300 N at which the strain is recoded to be 1% at the breakage of the sample. More observations of the sample breakage are made in the Fig. 41. and Fig. 43. the patterns in both x and y direction this particular off-axis loading.

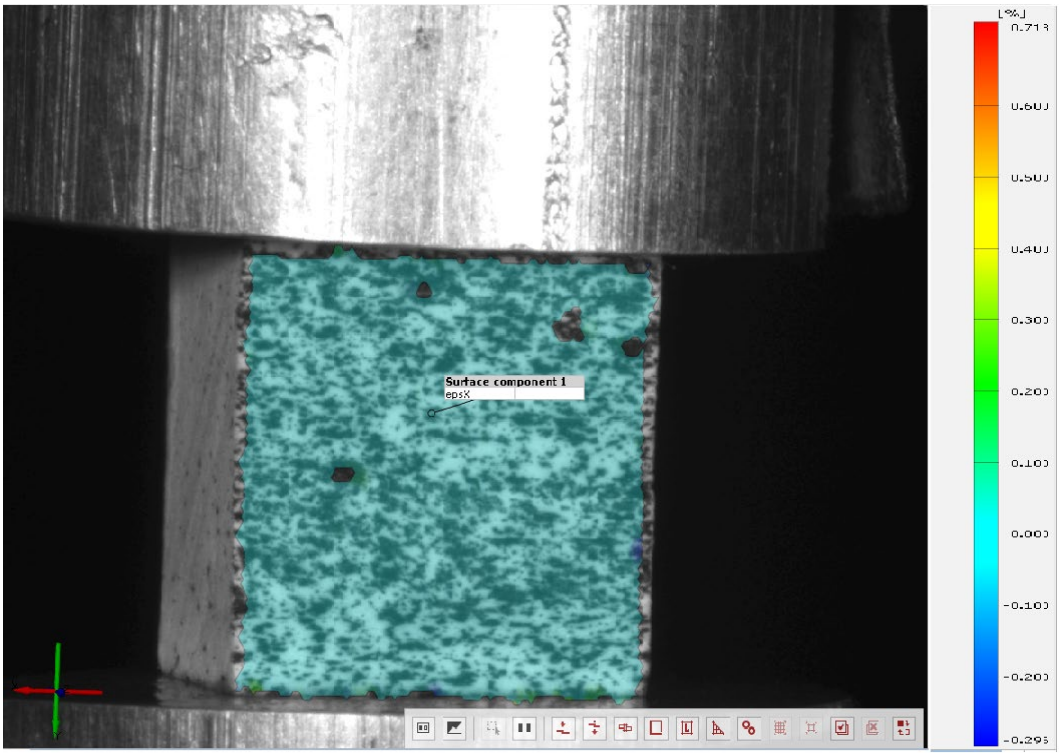

Figure 40 Surface component formed on the speckle pattern when the preload is applied to place the sample between the platens.

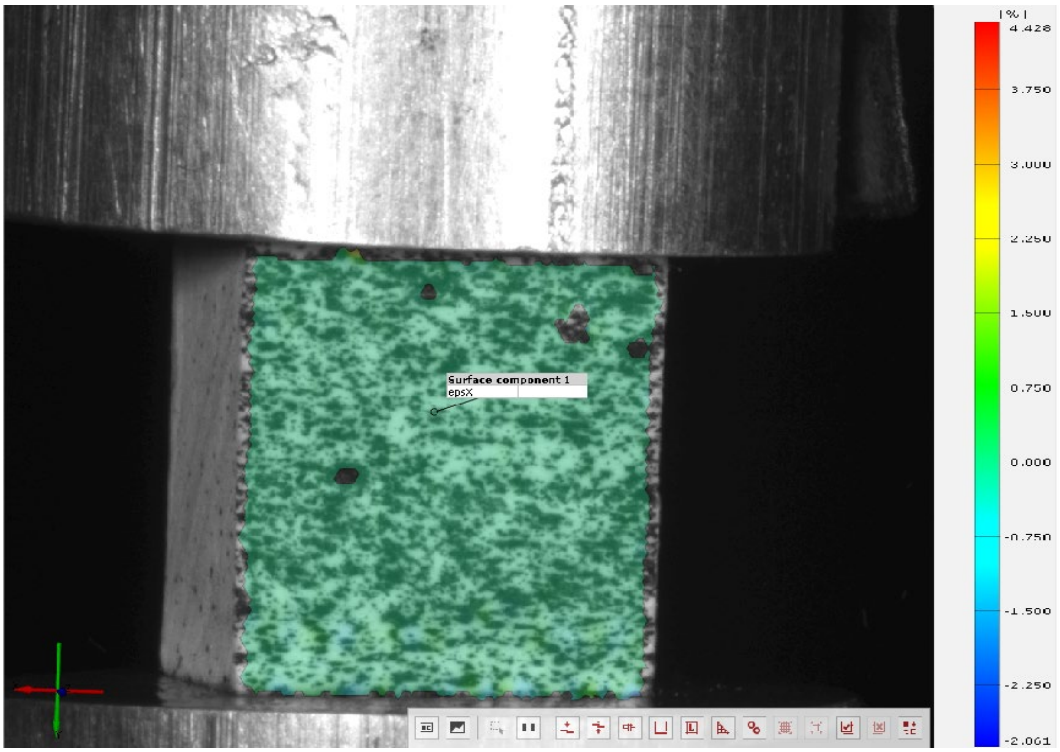

Figure 41 Strain measurements are recorded by the DIC system at 15th sec for 90-degree off-axis loading.

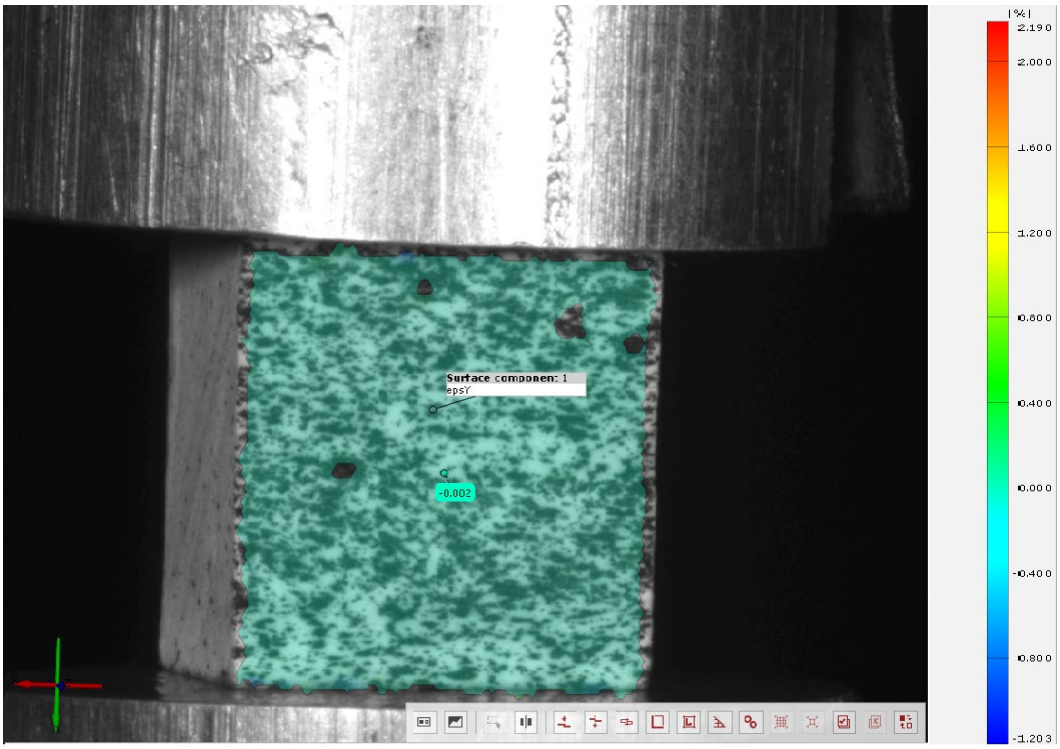

Figure 42 Initial surface component of the y-component in the applied direction

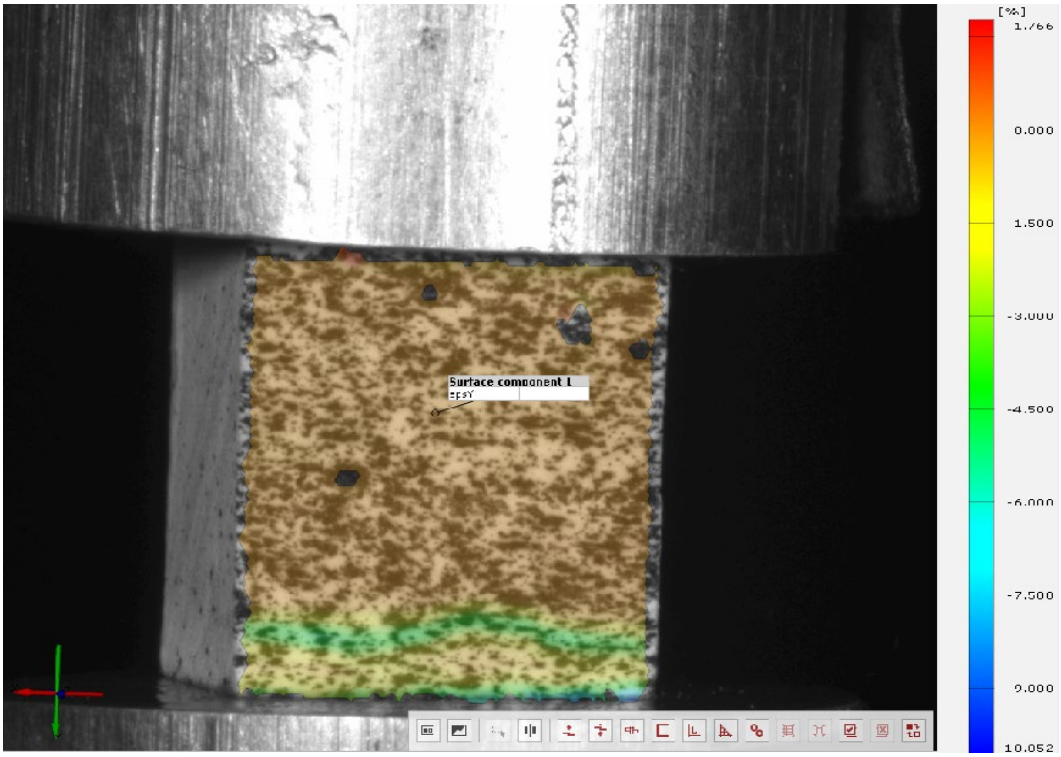

Figure 43 Strain measurements recorded by DIC system at 15th sec of y-component

The below plots are represented for the minimum value sample which is uniaxially compressed. The stress and strain values are determined from the above formulae. The load rate and force rate are determined from Fig. 44 and Fig. 45. The 90-degree orientation is the perpendicular to the zero-degree orientation. It is clearly observed from the images that the sample breaks from the bottom of the sample. These deformation values are recorded by the DIC system. The deformation that represented in the Fig. 47 and Fig. 48 are snapped when the sample starts to break at 0.8% strain.

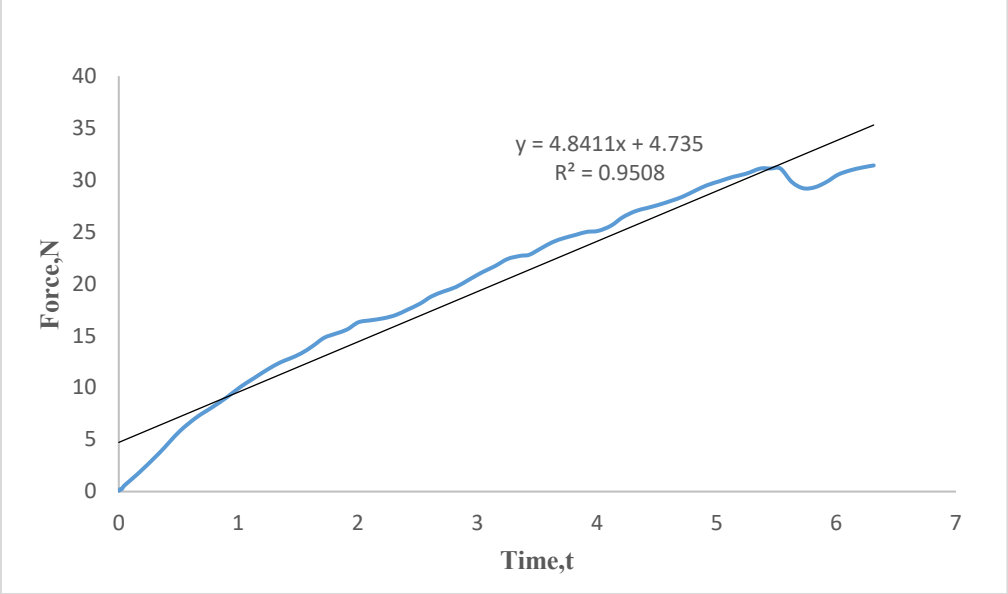

Figure 44 The compressive load with respective time of 90-degree manufactured slab with a minimum strength of all tested samples

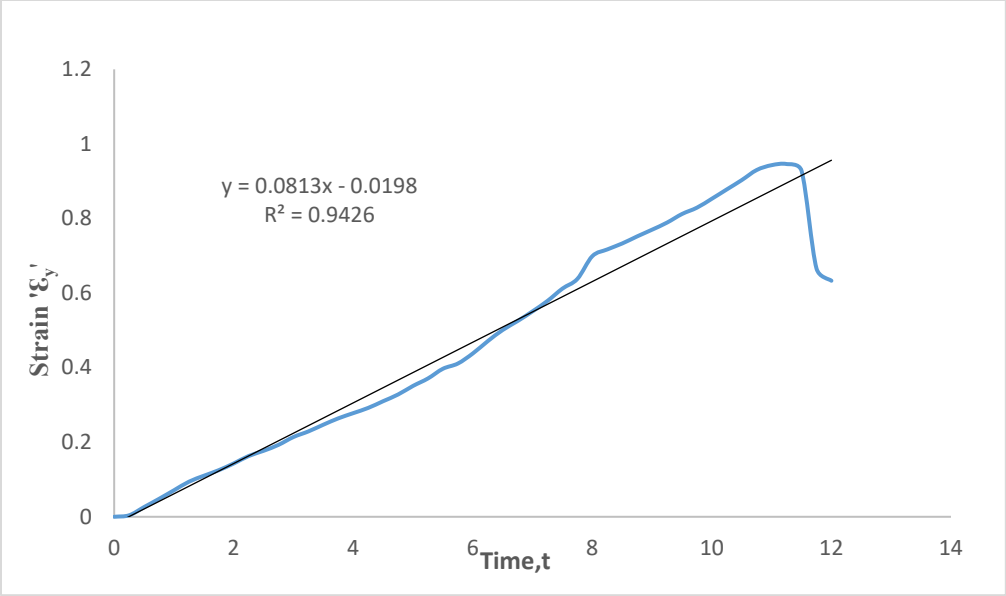

Figure 45 Strain-Time curve of 90-degree manufactured slab with a minimum strength of all tested samples.

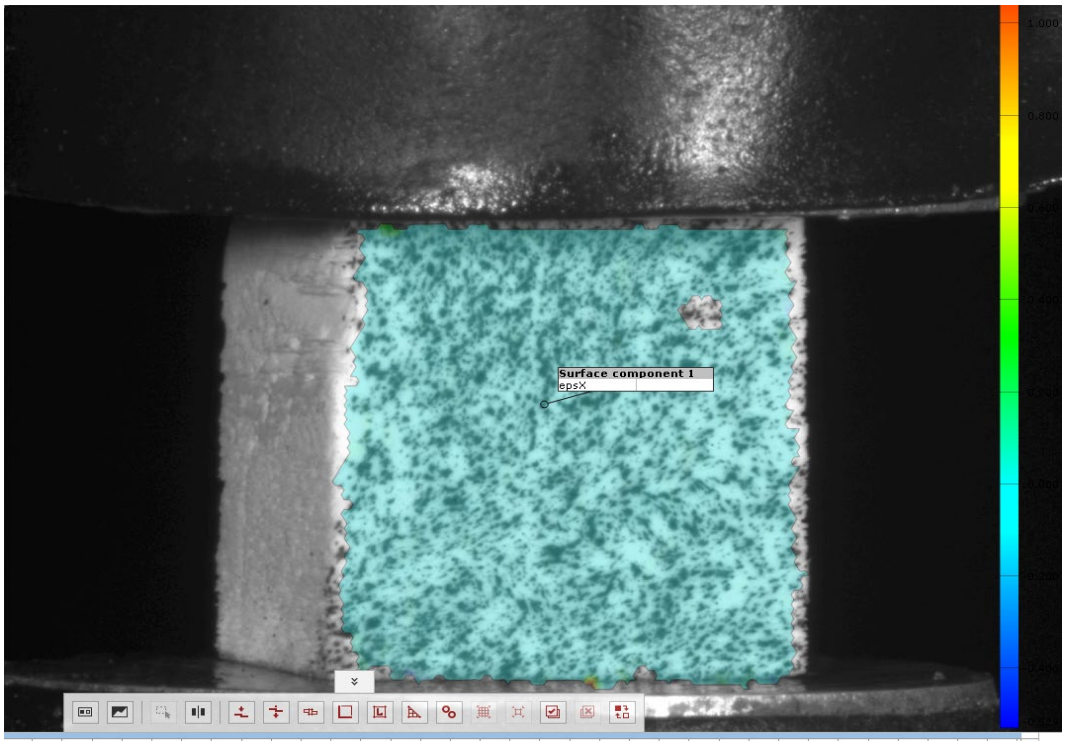

Figure 46 Initial pattern formation by DIC system in the x-direction for minimum value sample of 90- degree off-axis loading.

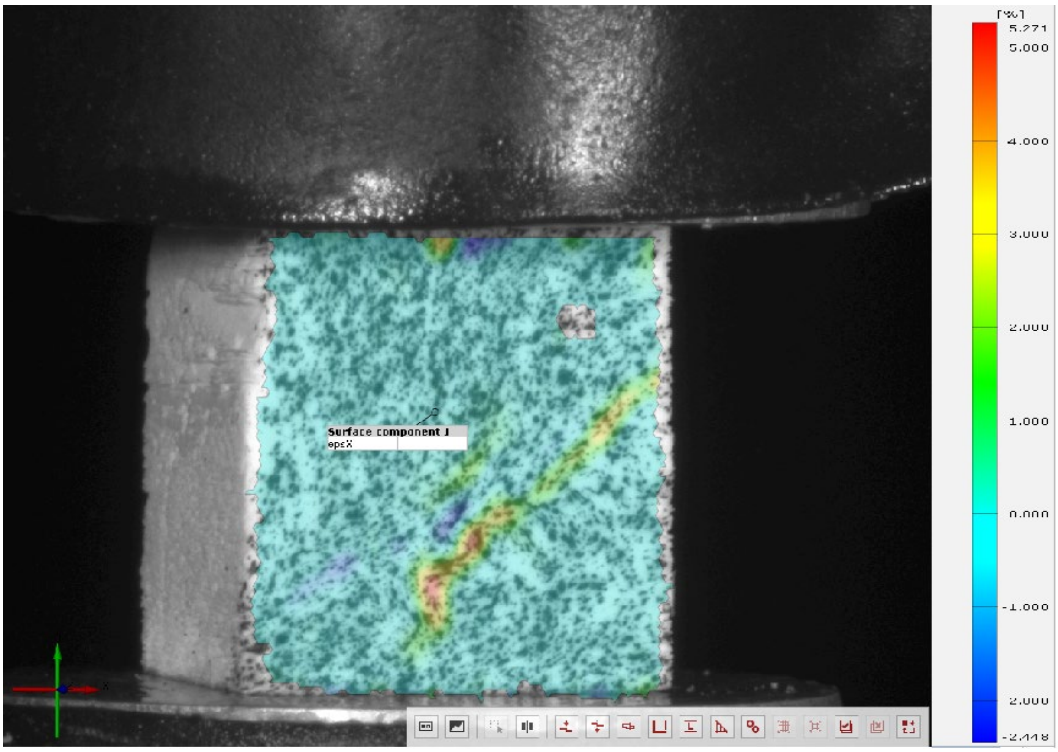

Figure 47 Strain value recorded at 15th sec when the load is applied for 90-degree off-axis loading sample.

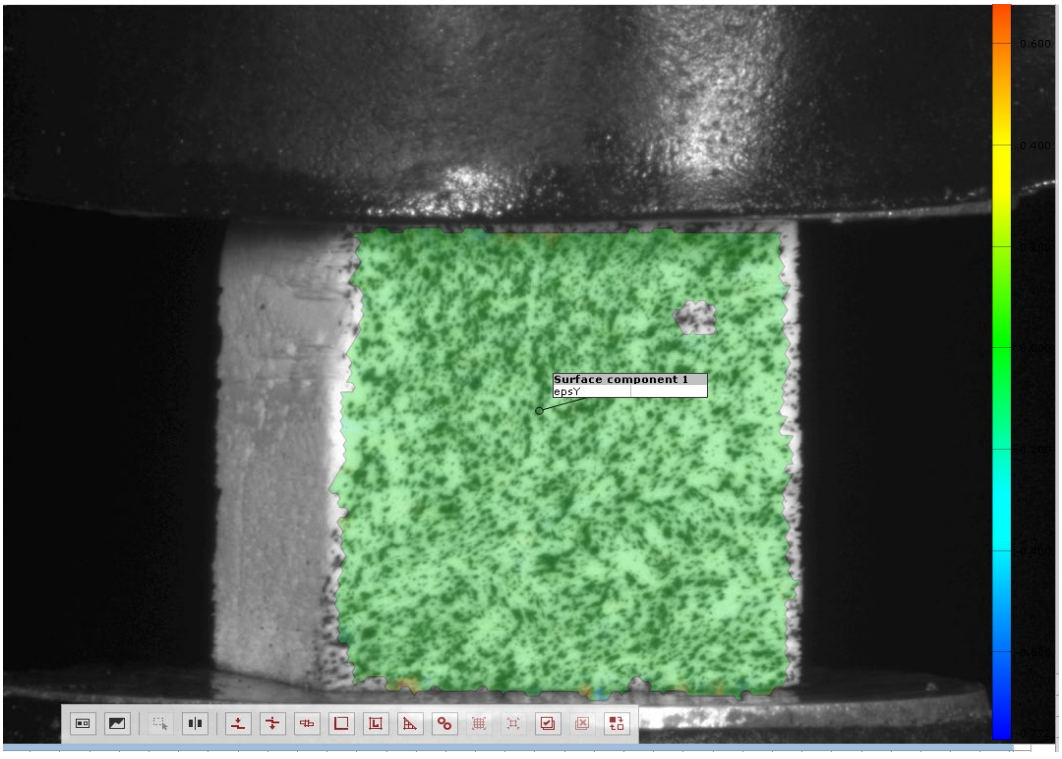

Figure 48 Initial pattern formation by DIC system when the pre-load is applied for 90-degree off-axis loading

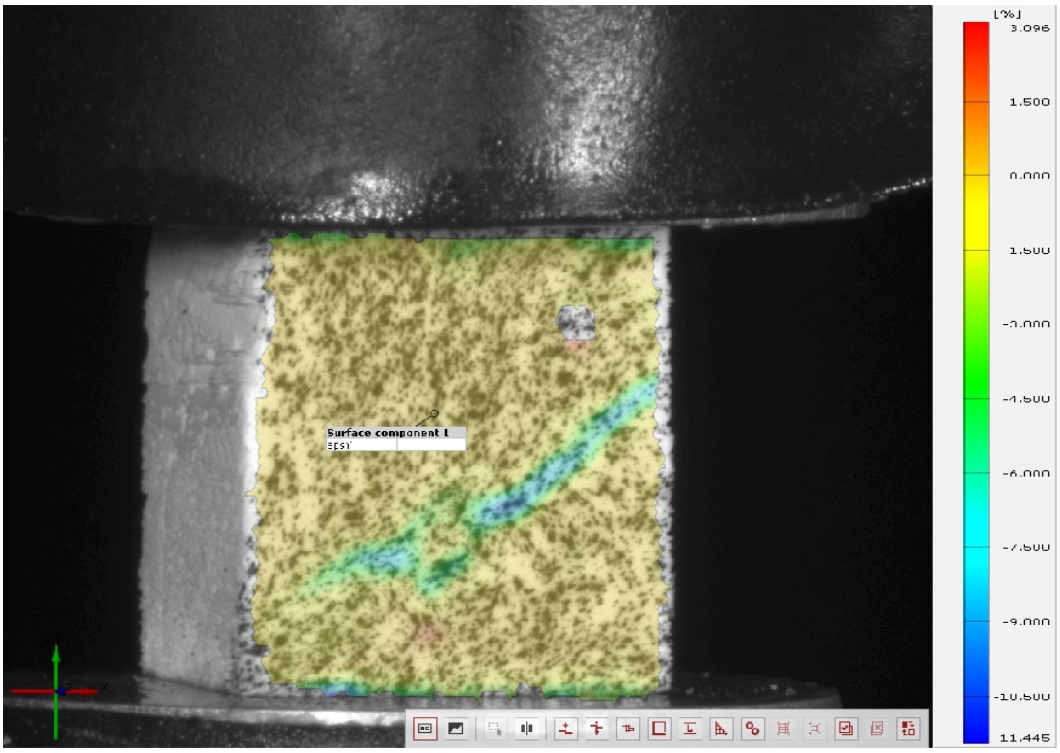

Figure 49 Deformation value recorded at 15th sec in the y-direction for 90-degree off axis loading

Fig. 50 represents the modulus values for the samples compressed perpendicular to ice-growth direction. The strength values are represented in Fig. 51 and the Poison's ratio values are represented in Fig. 52. The average modulus for the 90-degree orientation is $\overline{E} = 987.13 \pm 111.796MPa$. The average stress of the tested samples is $\overline{[\sigma]} = 7.808 \pm 3.61MPa$. The average value of poison's ratio where the $\vartheta_{12} = 0.1407 \pm 0.08$.

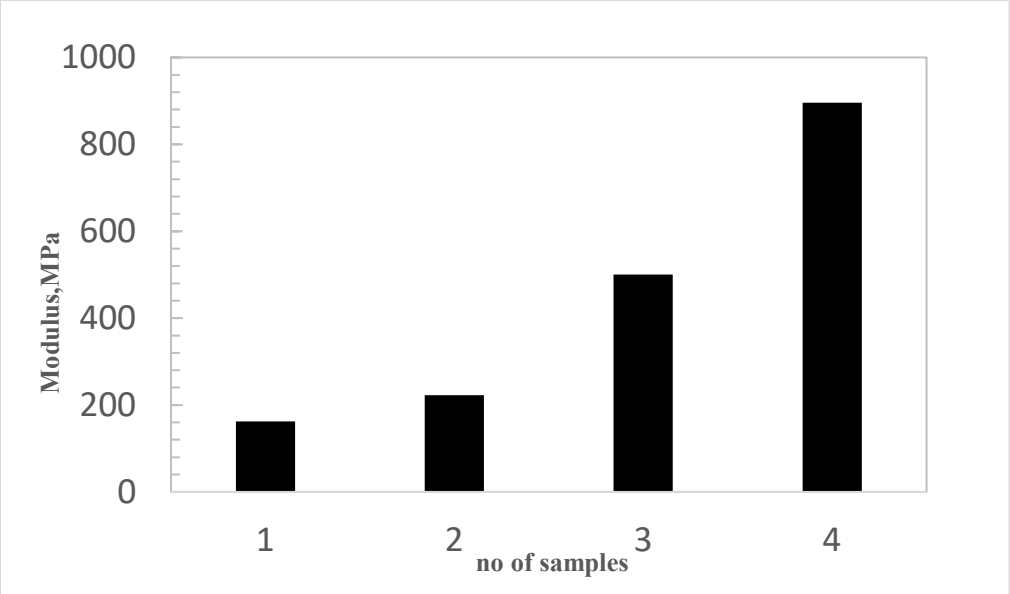

Figure 50 Modulus of all the compressed samples for 90-degree orientation

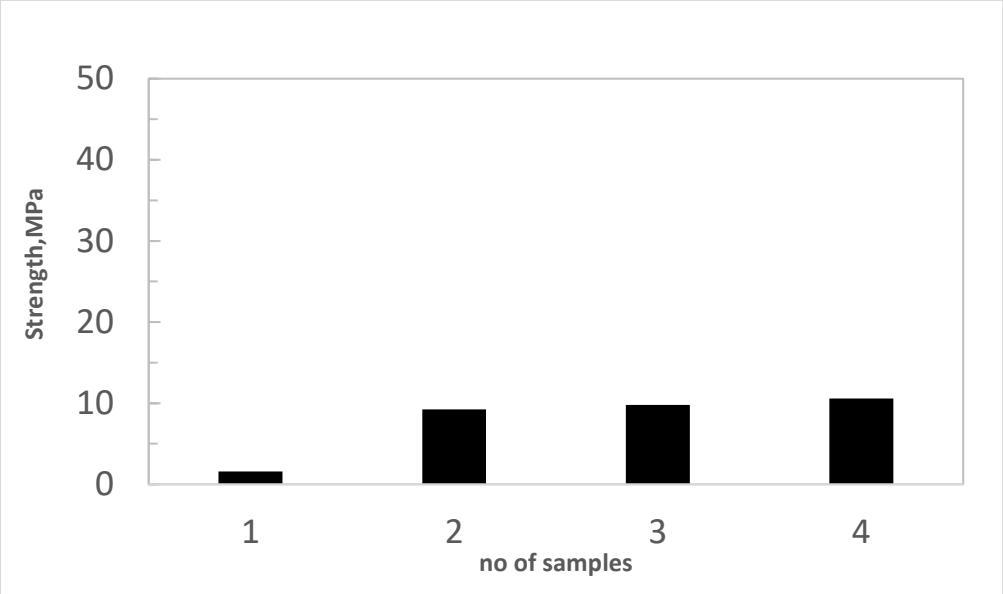

Figure 51 Compressive strength of tested samples for 90-degree orientation

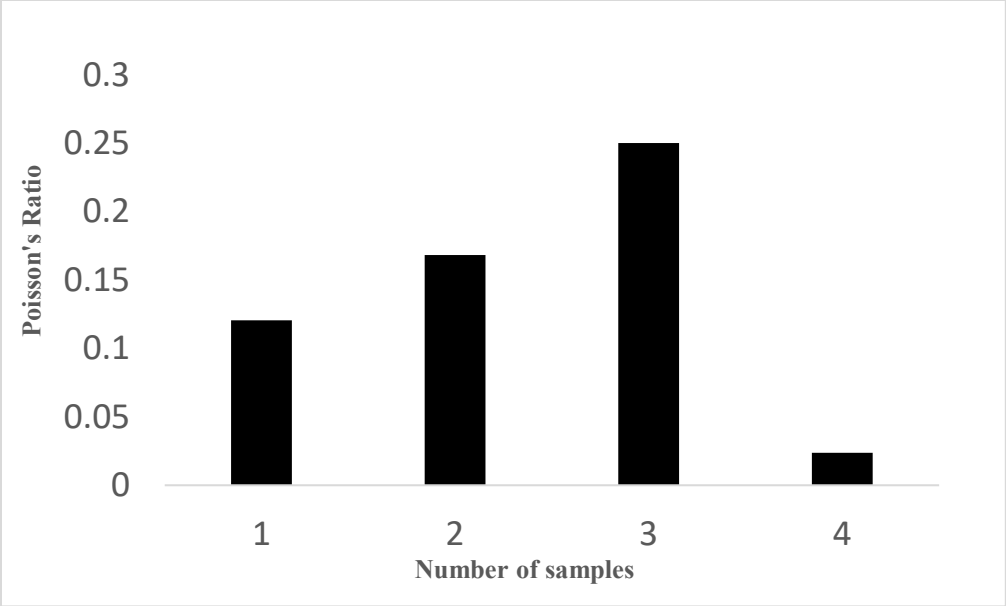

Figure 52 Poison's ratio of a compressed samples for 90-degree orientation.

The values of maximum and minimum values of each sample in three different orientations. The off-axis moduli of all the samples with respect to the angle of orientation are shown in Fig 53. It is observed that there is a decreasing trend with respect to the increasing angle. It is important to observe this trend as it will be helpful to corelate with the computational values.

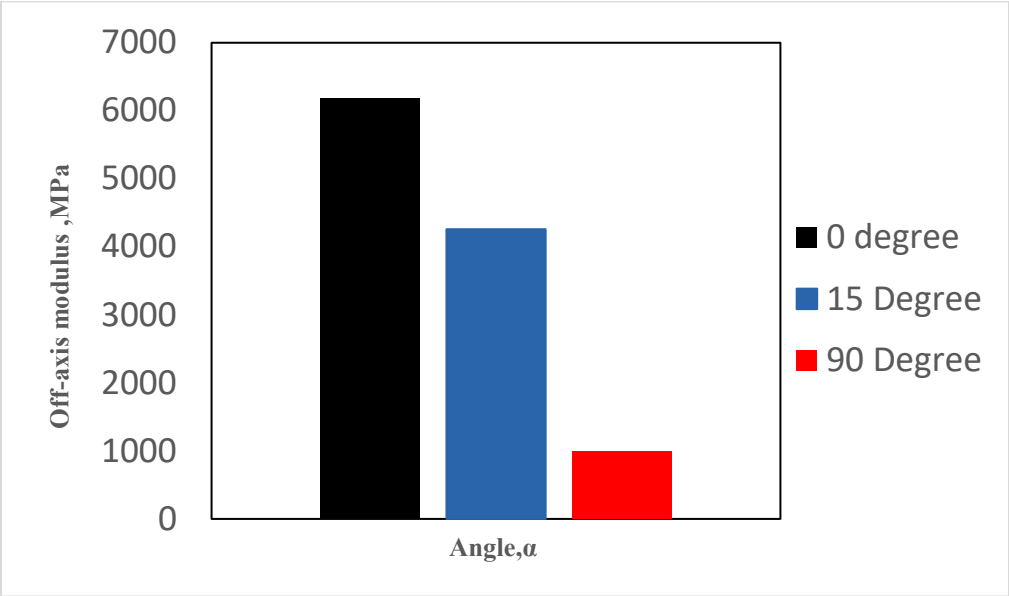

Figure 53 Comparison of off-axis modulus for three different off-axis loading

Table 1: Average off axis modulus and average strength experimental values for different orientations.

S. No	Angle of orientation (α)	Avg. Off-axis Modulus ($\bar{E}$,MPa)	Avg. Strength ($\bar{\sigma}$,MPa)
1	0	6181.36	32.43
2	15	4259.75	23.80
3	90	987.130	7.80

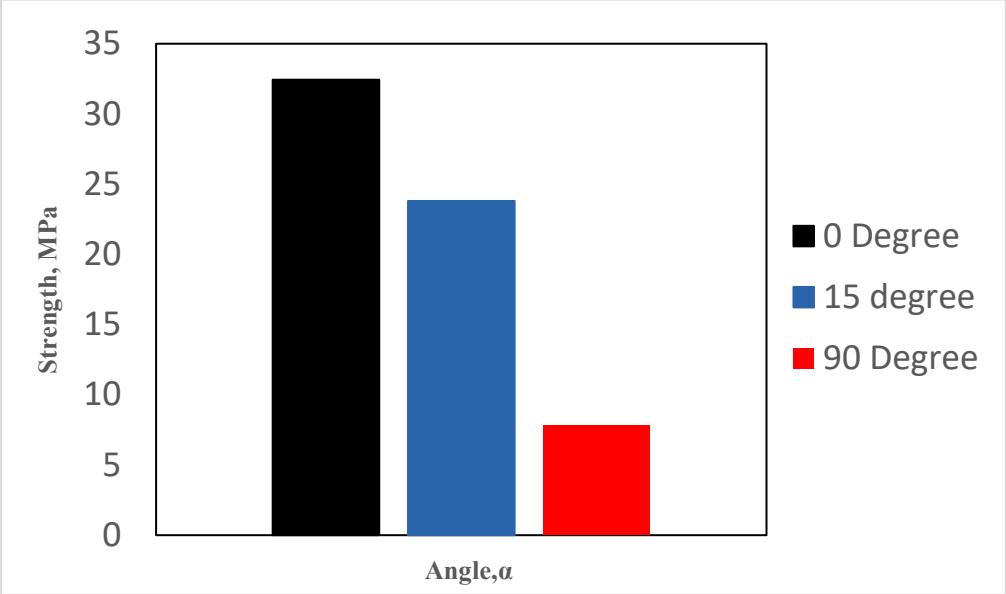

Figure 54 Comparison of strength in different orientations

It is depicted from the above data plot in Fig 54 that under compression for the considered off-axis loading zero-degree, 15-degree, 90-degree the calculated values for the strength and modulus are decreasing as the angle of orientation is increasing vice versa the calculated strength and the modulus increases as the angle of orientation decreases.

CHAPTER 5

Computational Results

5.1 Represented Volume Element

Cellular solids in the form of either honeycomb-like materials with prismatic cells or foams with polyhedral cells are widely used in engineering applications such as lightweight structural sandwich panels or components designed for absorbing impact energy. Models which predict their compressive failure behavior have broad applicability to both engineered and natural cellular ceramics.

Unit models have proven to be useful theoretical tools for understanding some of the key aspects of the mechanical behavior of cellular solids, such as the dependence of failure properties on relative density and on the failure mode of individual cells.

Gibson and Ashby reported that their unit cell models typically overestimated the compressive strengths of the metallic honeycombs. Papka and Kyriakides found that the strengths predicted by the finite element methods of honeycombs with periodic, hexagonal cells were approximately 15 % greater than the corresponding experimental values obtained from the tests on aluminum honeycombs. It was concluded that differences between the predicted and measured strengths were due in part variations in cell geometry that were not accounted for by their models.

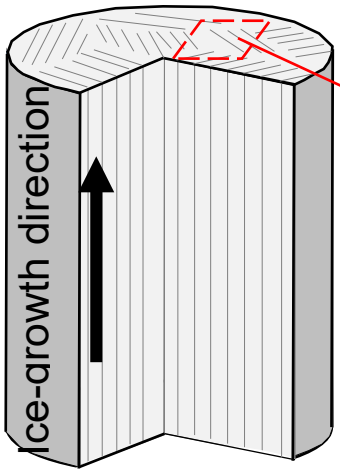

Figure 55 Schematic presentation of the growth-oriented alumina.

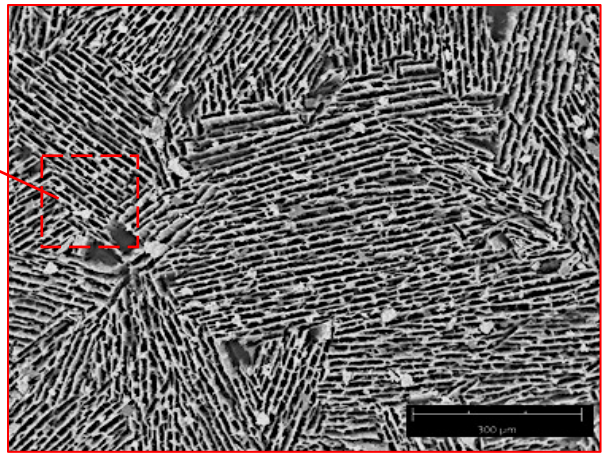

Figure 56 Images of alumina from Scanning Electron microscopy.

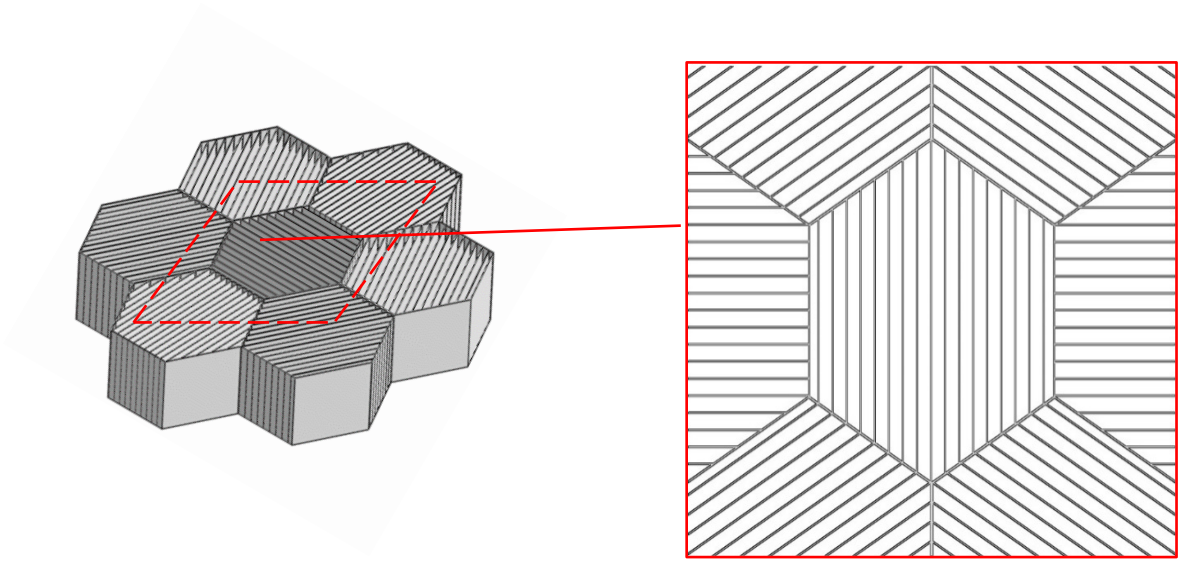

Figure 57 Schematic representation of the Represented Volume Element which is developed for micromechanical analysis.

A Representative Volume Element (RVE) of periodic geometry was generated. The compressive behavior of the RVE was determined using finite element analysis using ABAQUS software. The cell walls were straight and of uniform thickness throughout the model, the relative density of the model was specified by assigning the appropriate cell wall thickness. The material properties of the model considered are elastic modulus and the poison's ratio.

Displacement boundary conditions were imposed to simulate the uniaxial compressive axial and the transverse directions. The odes along the fixed edge of the model were constrained from translating in the loading direction; the nodes along the opposite, displaced boundaries were displaced incrementally in the loading direction and from rotating in the axial and transverse direction but were free to translate in non-loading direction. This approach allowed for the failure of cell walls by elastic buckling. The applying of boundary conditions results in the nodal reaction forces which are dived by the plane cross section area to determine the normal stress in the loading direction in each increment. The increment steps which are considered as a time period which later multiplied with strain rate to determine the strains. The elastic modulus was computed as the linear slope of stress-strain curve.

5.2 Boundary Conditions

Free Boundary Conditions:

These are the boundary conditions which are imposed for a molecule, a cluster or an aerosol particle in a vacuum. These conditions are also applied for the ultrafast process when the effect of boundaries is not important due to the short time scale of the involved process.

Periodic Boundary Conditions:

These boundary conditions are used to simulate the process in a small part of a large system. All the atoms in the cell are replicated throughout the space to form an infinite lattice. Each particle in the computational cell is interacting not only with other particles in the cell but also with other images in the adjacent boxes. The choice of the position of the original box has no effect on the forces or behavior of the system. The displacement of the particle is measured from left and right directions, then these measurements with the adjacent boxes in which these are used as a periodic boundary conditions and these tend to form boundary conditions which will replicate and tend to form boundary conditions which will replicate and tend to form boundary conditions which will replace and tend to form infinite cells.

The following are the boundary conditions applied for the RVE:

Periodic Displacement Boundary conditions

$$u\,(0, x_2, x_3) - u(L_1, x_2, x_3) = U_1$$

$$u(x_1, 0, x_3) - u(x_1, L_2, x_3) = U_2$$

$$u(x_1, x_2, 0) - u(x_1, x_2, L_3) = U_3$$

Homogenized stress, strain from RVE analysis

$$\varepsilon_i = \frac{U_i}{L_i}$$

$$\sigma_i = \frac{R_i}{A_i}$$

where

U is the displacements in the respective directions

L is the length of the applied load direction

R is the load applied

A is the area of the plane in which the load is applied

One of the most complicated loading conditions on the composite is off-axis loading. Off-axis loading happens when a uni-directional growth oriented is subjected to a force in inclined angle with direction.

In order to develop the RVE model of the micrographs, ice-templated scaffolds fabricated under uni-directional freezing conditions from a dense layer to anisotropic cellular structure to eventually a lamellar morphology oriented in the direction of the applied thermal gradient that prevails for rest of the length of the sample are studied. These micrographs are from Scanning Electron microscope. The geometric parameters of the micrographs where how the growth of ice influenced the porosity of the alumina scaffold are studied. From the images, the distance between the walls is measured and the thickness of the wall is measured. The mechanical

properties for different sintering temperatures of the α-alumina were studied. The objective of the study is to derive a coherent, self-consistent, and comprehensive set of property values for a single specification of alumina. This data has an increasingly important role to play in both manufacturing and material science applications. These data are helpful in understanding the significance of the properties and correlate the experimental data with the computational data. Finally, the number of displacements was defined on RVE to tabulate the Force and displacements and measuring the cross-sections of the RVE to plot the Stress-strain curves.

5.3 Results

Off-axial Loading in different directions.

The smallest repeating element of the composite can be used as the representative element (RVE). It is important to understand the x-direction, y-direction, z-direction for a three-dimensional computed representative volume element. For the below image (Fig. 58) the load-displacement is applied in the z-direction which we also refer as axial load direction. The job is performed incrementally with a defined step time. Upon the applied load the stress concentration values represented by different colors in the stress contour.

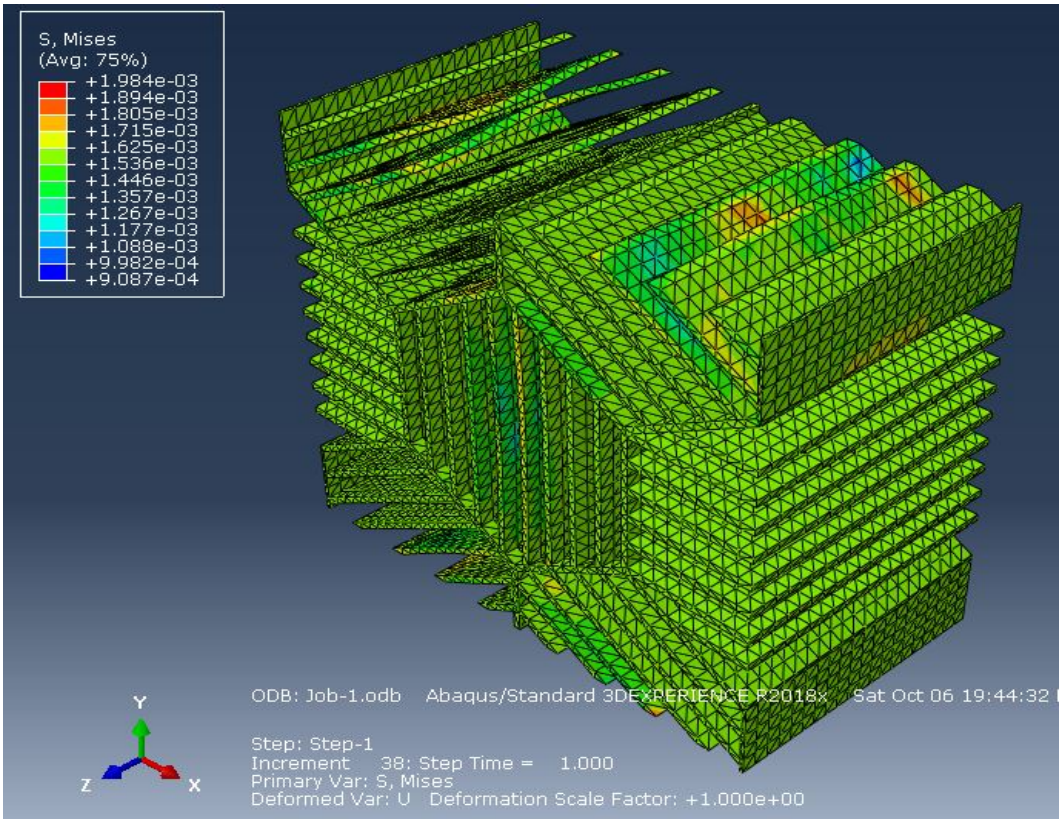

Figure 58 Stress contour plot of RVE under axial loading

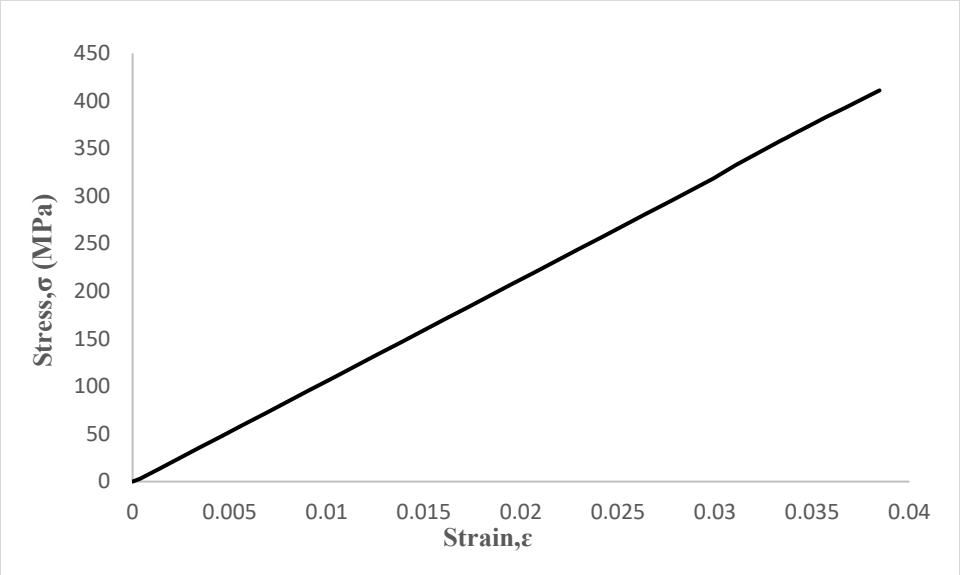

Figure 59 Stress-Strain values of Represented Volume Element displacements applied in the axial direction.

It is well observed from the above Fig. 59 that the stress-strain values are calculated by applying displacement boundary conditions, which the RVE is compressed by 4%. In addition to the displacement boundary condition, bottom edges and side edges are applied boundary conditions which ensure the fixed edges of the RVE which ensures the loading will be pure compression. The maximum stress values in the axial direction for 1% strain is almost 100 MPa. Similarly, as in the above case, the displacement boundary condition is applied in the transverse direction, the displacement applied with reference to the x-z plane. Then the RVE is compressed by 0.28%. This boundary condition is applied during "Applied Load" step of the Abaqus model. In addition to displacement boundary conditions, bottom edges and the side edges are constrained to ensure the loading will be pure loading.

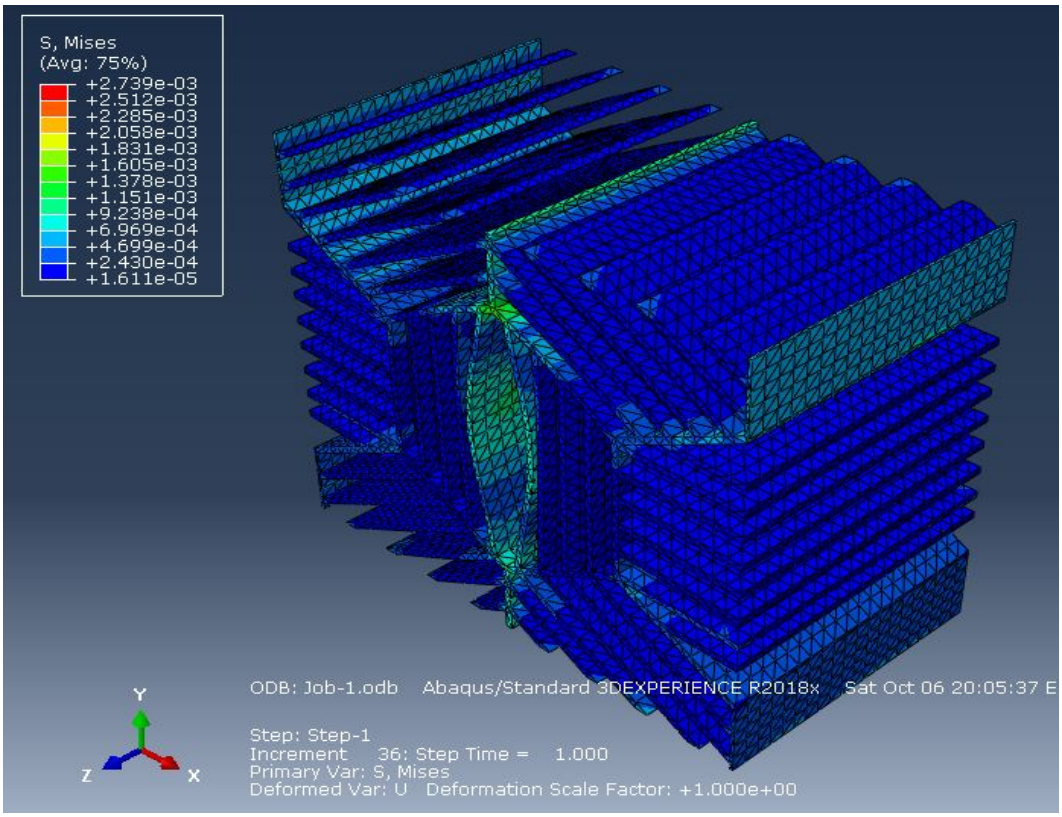

Figure 60 Stress contour plot of RVE under transverse load.

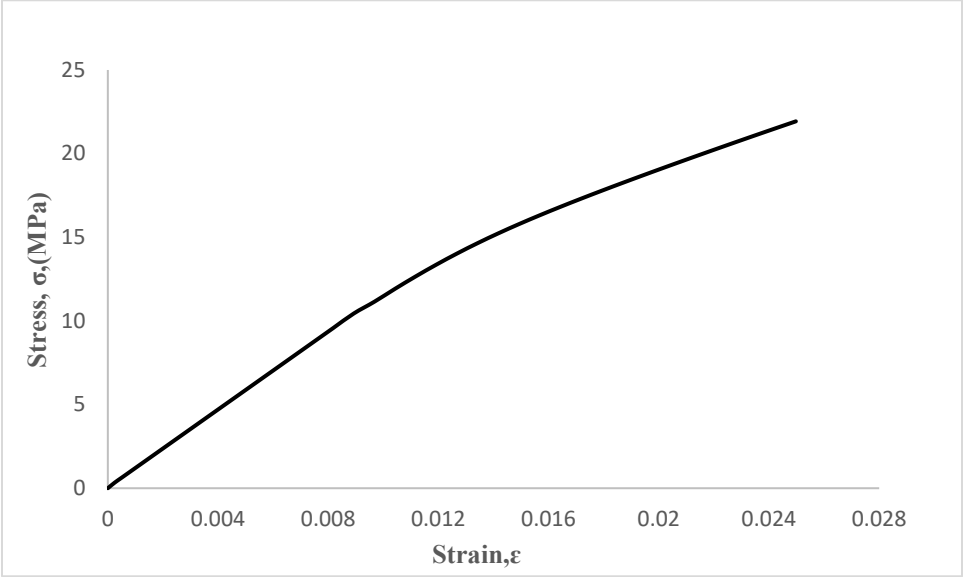

Figure 61 Stress-Strain curve for RVE under the transverse load.

For a finite mesh, the stress-strain curve is studied in order to analyze the results. The plot of Stress Vs Strain is obtained. According to this plot, stress varies linearly with the true strain till 1% strain and there is buckling observed in representative volume element.

Similarly, the compression displacement loading, the displacement boundary condition is applied to RVE 1% displacement is imposed on RVE under shear loading. Also, the bottom edges of RVE are fixed under shear loading. It is evident in the above Fig. 62 the stress on the four edges of the RVE where the values are defined in the stress contour table.

The shear loading stress-strain values are plotted in Fig. 63 after the job is submitted for analysis where the displacement boundary condition is applied at the dummy node or reference point. The stress varies linearly with true stain value up to 1% strain.

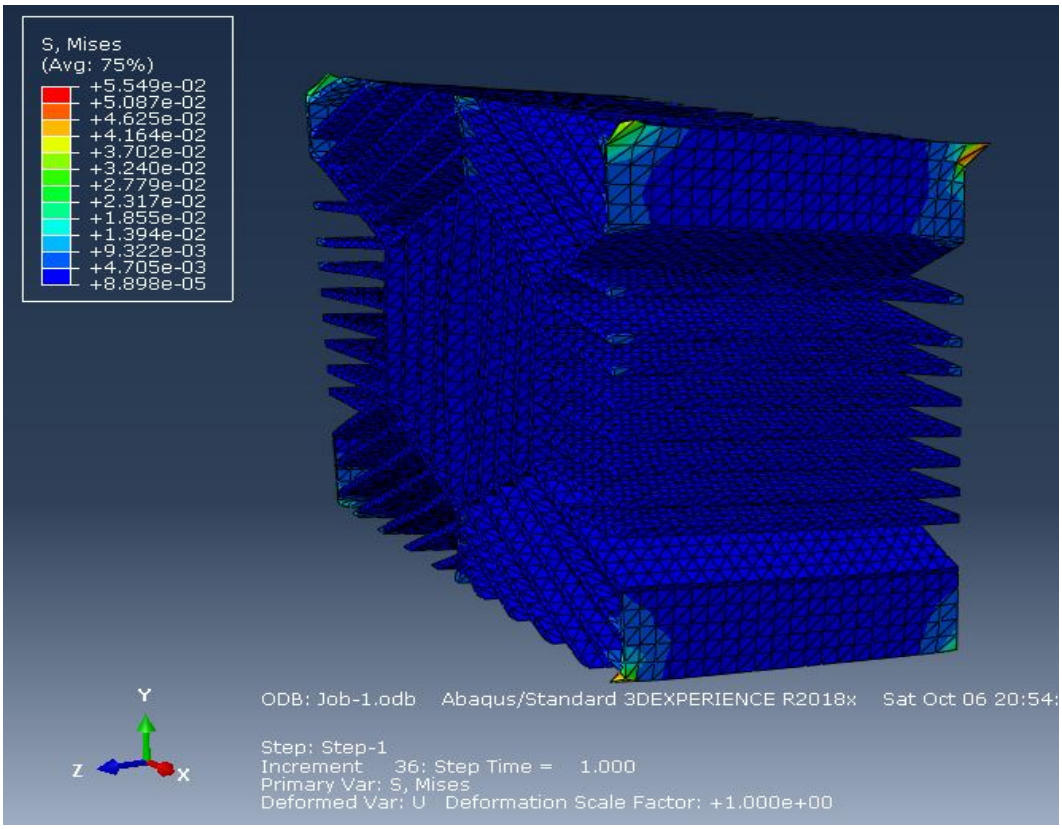

Figure 62 Shear displacements applied on the axial direction plane

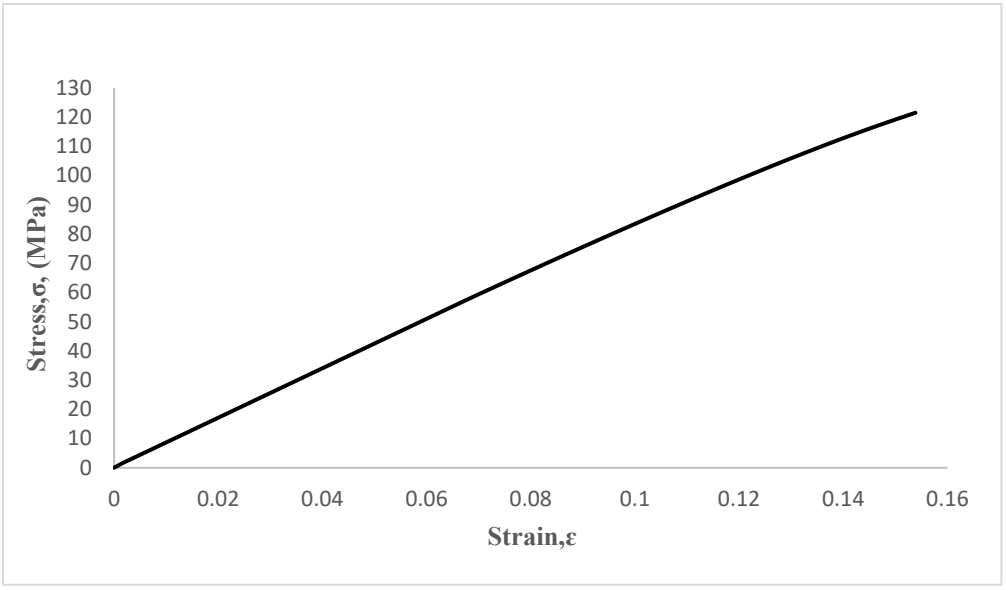

Figure 63 Stress-strain curve when displacement boundary conditions applied on the x-y plane

The relations between microstructural and elastic properties for both isotropic and anisotropic non-periodic honeycombs were, on average, not different from those for periodic honeycombs. A computational procedure for calculation of transformed elastic constants is illustrated by the following equation

$$\frac{1}{E_x} = \frac{m^2}{E_1} = (m^2 - n^2 v_{12}) + \frac{n^2}{E_2}(n^2 - m^2 v_{21}) + \frac{m^2 n^2}{G_{12}}$$

$$m = cos\theta \quad n = sin\theta$$

Poisson's ratio v_{12} achieves by dividing lateral strain (transverse strain)/Axial strain

Then v_{21} obtains by $v_{21} = \frac{E_2}{E_1} v_{12}$

The stiffness of the ice-templated sintered scaffolds was estimated from the slope of the linear part of the uniaxial compressive stress-strain curves. The Young's modulus of ceramics is dependent on crystal structure and microstructural features namely porosity. By changing the level of porosity various studies have been made to understand the strength, modulus and fracture toughness of alumina. The strength and modulus decreased with an increase in porosity.

Off axis moduli for 26% relative density

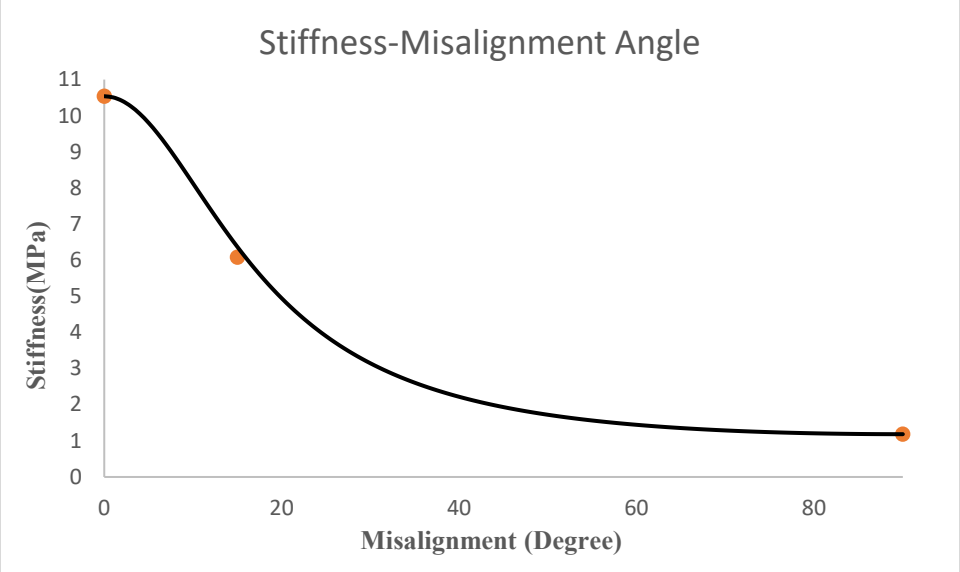

Figure 64 Calculated off-axis modulus is plotted for the different angle of orientations

It is very significant to understand the relationship between the off-axis modulus and the angle of orientation, as the alumina is anisotropic material. Now the modulus values, which are calculated from the above equation with respective off-axis loading angle are plotted and shown in Fig. 64. The trend of the graph is the off-axis modulus decreases as the angle of orientation increases. This calculated off-axis modulus at different orientations will help to correlate the modulus values with the different relative density representative volume and also with the experimental values.

Representative Volume Element of Relative Density 0.21

After successfully running the analysis for compression loading, the following contour plot is obtained for the RVE as shown in Fig. 65. It is observed that maximum stress and minimum stress are obtained for a defined mesh seed size. The stress concentrations values of RVE are illustrated in the stress contour. The stress-strain plot is observed to be the stress is linearly proportional to the strain. The stress linear elastic behavior is observed and the strain 4% is nearly 350 MPa shown in Fig. 66.

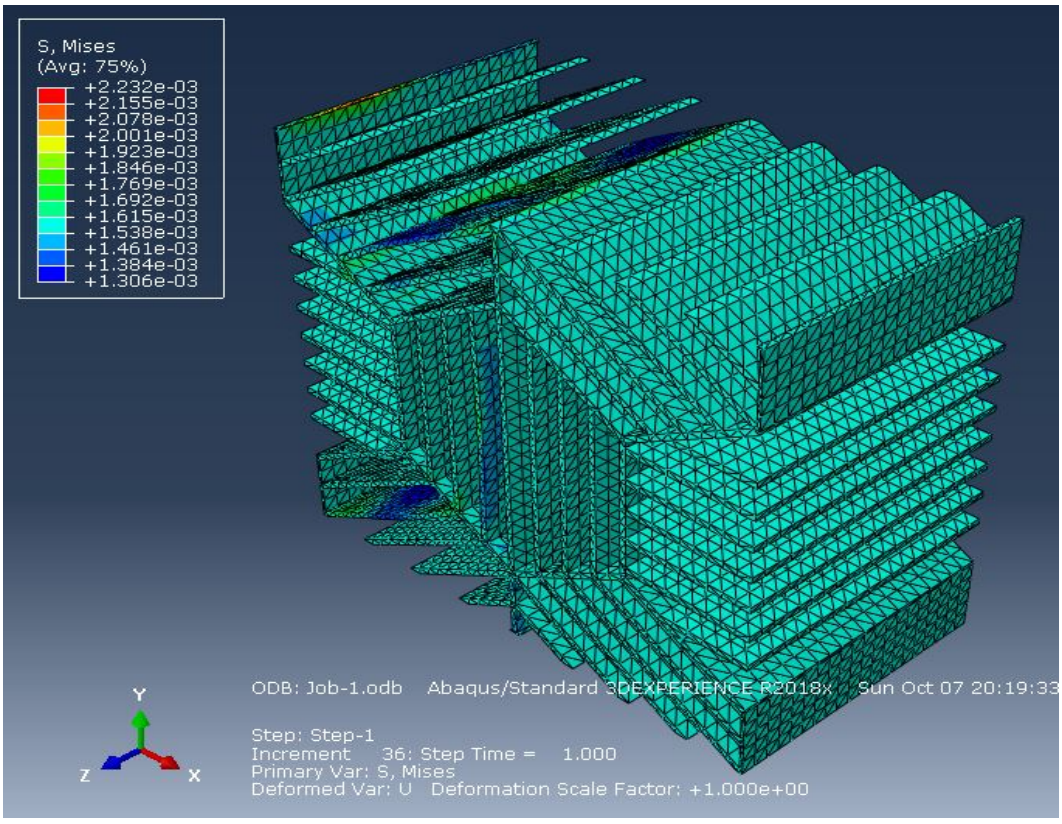

Figure 65 Stress contour of RVE with 21% relative density in the axial direction.

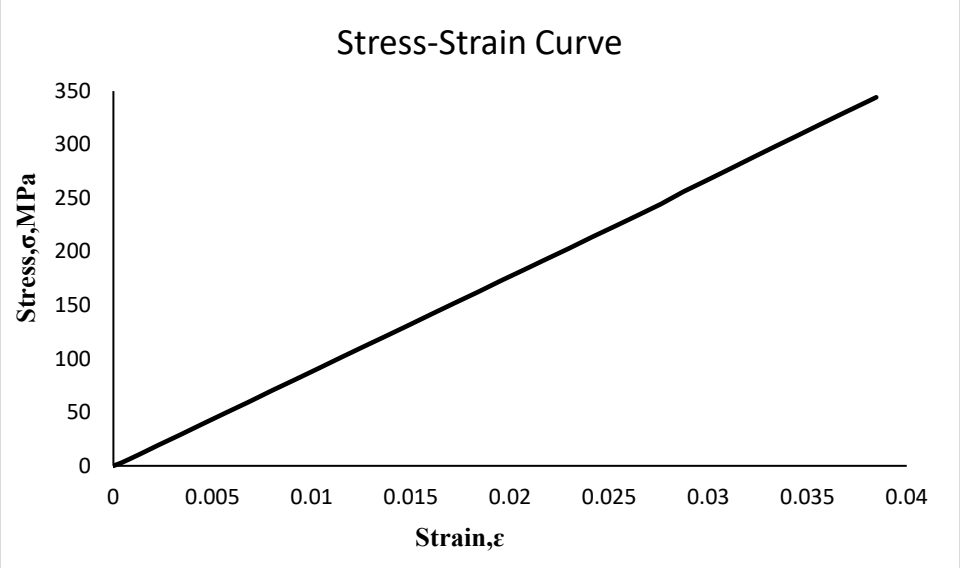

Figure 66 Stress-strain curve for the relative density is 0.21 under displacement boundary conditions.

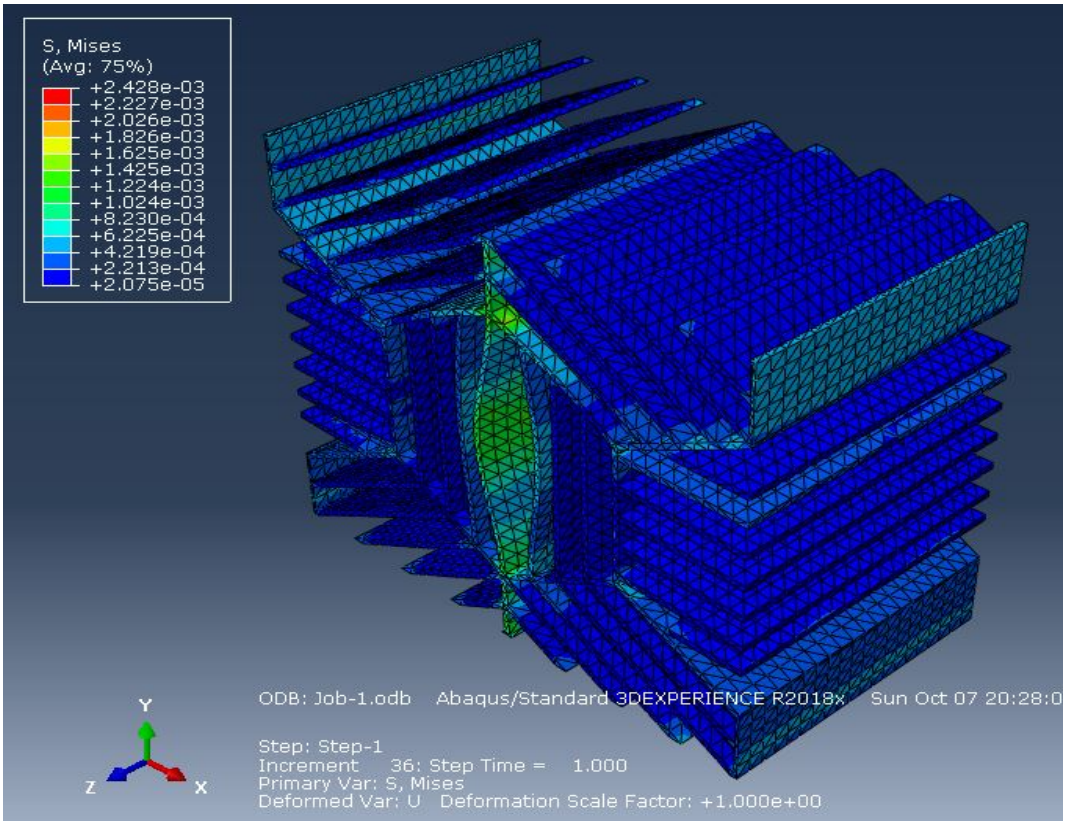

Figure 67 Stress contour of RVE with relative density 21% in the transverse loading

After submitting the job for analysis, which is applied in the transverse direction, it is observed that the buckling of the central walls of the RVE. The color representation of the RVE represents the indicates the stress contours. The stress varies linearly with the true strain of up to 1.2% from the Fig 68. The stress at 1.2% is 13 MPa and the stress at 2% strain is 18MPa.

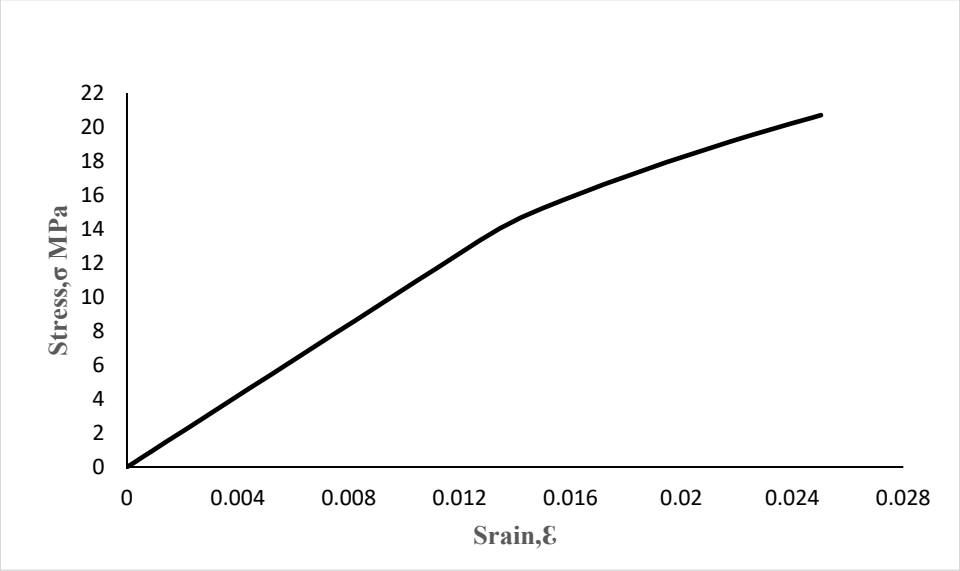

Figure 68 Stress-Strain curve plot of RVE which displacement boundary conditions are applied in the transverse direction.

From Fig. 68 the stress strain curves are plotted for the RVE of relative density 0.26 further calculating the stiffness values in the transverse direction. Similarly, the shear boundary conditions are applied to RVE in Fig. 69 to find the stiffness. From the transformed elastic constant equation for anisotropic materials the off-axis angle values are substituted to find the values of the modulus values for different off-axis loading.

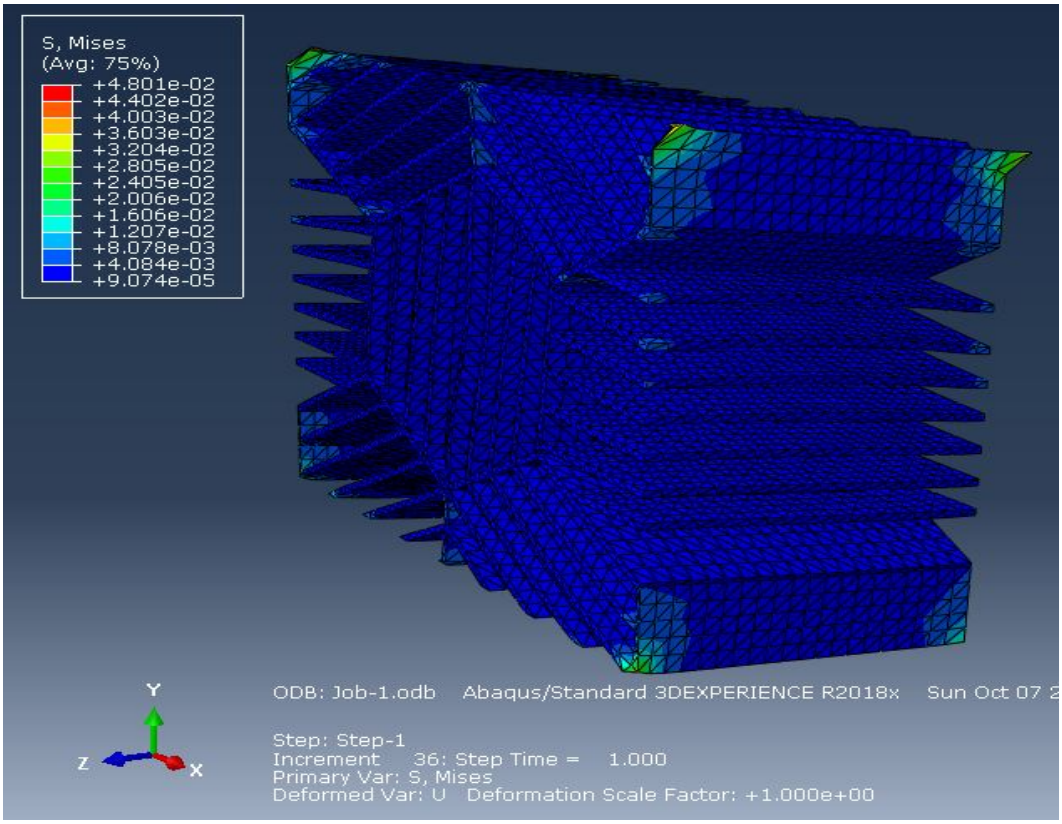

Figure 69 Shear displacement boundary condition applied in the axial plane

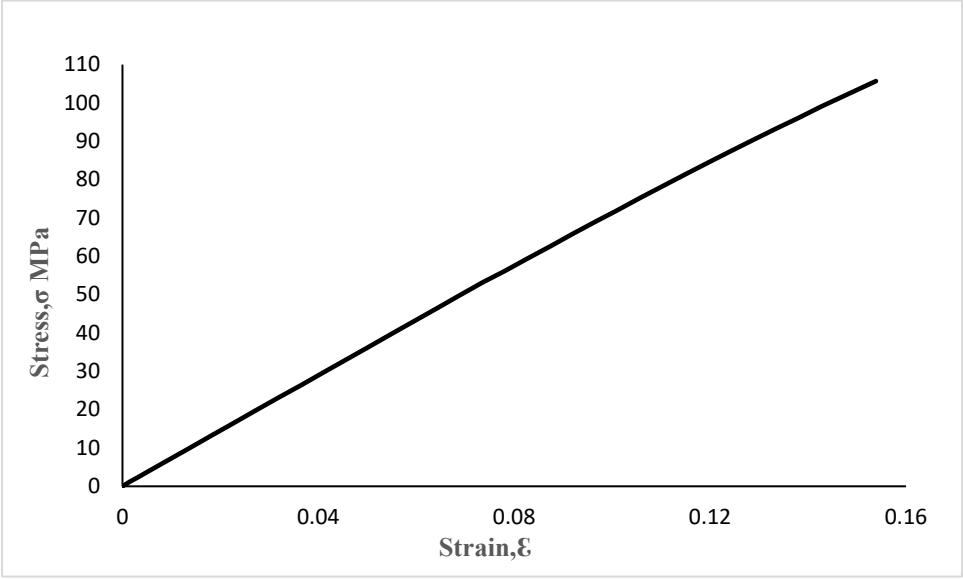

Figure 70 Stress-strain curve when shear displacement applied in the x-y plane.

Off-axis moduli for 21 % relative density

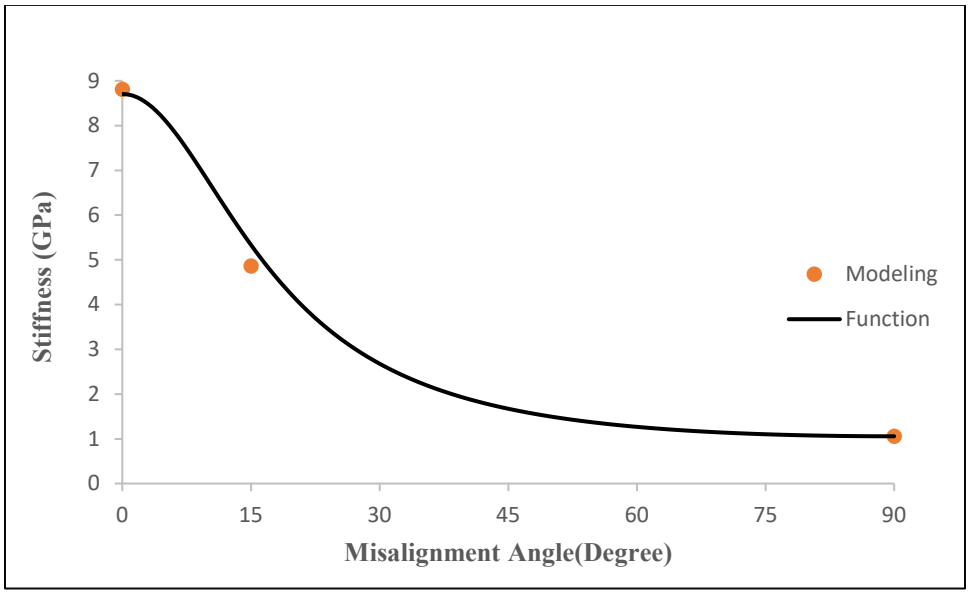

Figure 71 Off-axis modulus plotted for a different angle of orientations.

The above Fig. 71 describes the stiffness-angle where the off-axis modulus is decreasing as the angle of orientation is increasing. The finite element predictions of relative densities 0.21 and 0.26 were analyzed were of the elastic constants are compared with available experimental modulus values.

Table 2: Comparison of modulus values experimentally and modelling values in different orientations

	0-degree Off- Modulus, GPa	15-Degree Off- Modulus, GPa	90-Degree Off- Modulus, GPa
RVE 0.21 % Relative Density	8.806	4.857	1.056
RVE 0.26 % Relative Density	10.539	6.0808	1.1843
Experimental Values (Average Value) 0.21 % relative density	6.181	4.259	0.987

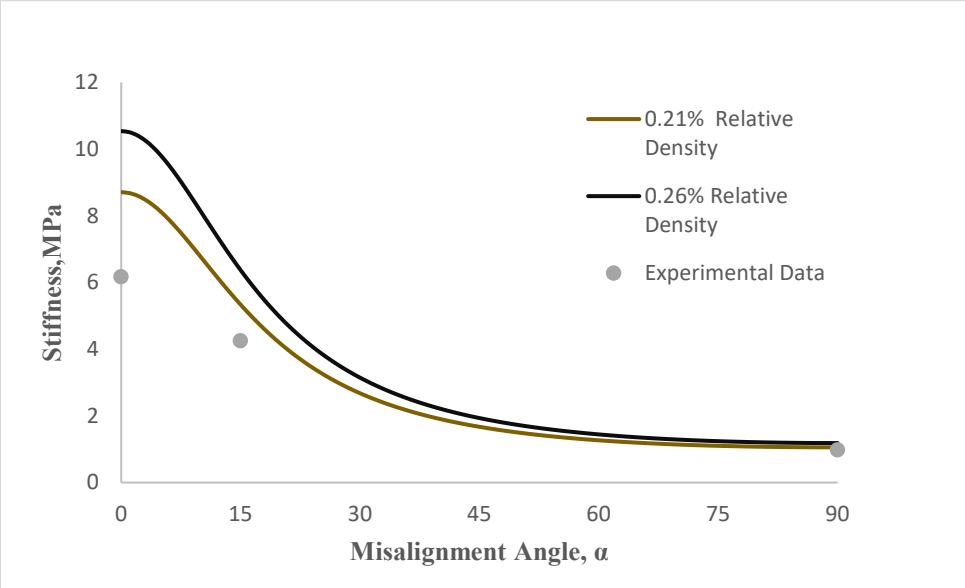

Figure 72 Comparison stiffness with misalignment angle of different relative densities and experimental values.

Results of the micromechanical model were compared of two relative densities compared with the experimental results are shown in Fig. 72. The above data table reveals that for the 0.21% relative density of the computational model is almost nearly to the experimental values of samples with 0.21 relative density. The values also indicate that as the relative density increases, the stiffness of the sample increases.

CHAPTER 6

Conclusions

The off-axis compressive behavior of ice-templated ceramic was analyzed using experimental results and micro-mechanical model simulation. Ice-templated ceramics is a versatile processing technique to manufacture the anisotropic ceramic foam by exploiting the anisotropic growth characteristics and lamellar morphology. During the freeze casting process, the gap between the cold plate and the liquid nitrogen is not varied; it is understood that the freezing velocity for all the casted samples is constant. The ice-templating process results in processing-structure-property relationships determined by the microstructure. The processed alumina samples which later manufactured by water jet machine from the freeze casting were tested under quasi-static off-axis loading conditions and were used to determine the mechanical properties of the material. Digital image correlation (DIC) was used to measure the strain response of ice-templated ceramic under off-axis loading. DIC results revealed non-homogenous strain distribution in the material during compression. Specifically, the origin of the localized strain concentration columnar regions, which are oriented in the ice-growth direction. Those regions were found to be the onset failure of in off-axis and 0-degree loading conditions. The experimental results reveal the strong influence of the loading direction on the compressive behavior of the ice-templated ceramic. Additionally, the properties like modulus, strength, and Poison's ratio are compared in all three different orientations, which essentially helps us to relate the values of computational model. It is observed from the tests that these values of three different loading conditions decrease as the angle of orientation increases. A Representative Volume Element is developed

to predict the behavior of off-axis loading. The micro-mechanical modelling is analyzed for two different relative densities. Micro-mechanical loading results indicated that buckling of lamella walls was determined as the driving factor of failure. The results of the model compared favorably with the experimental results. It is evident from the plots of computational models that the modulus value increases as the relative density increases. Nearly, the values of three different loading conditions and the values obtained from the anisotropic equation of computational model with same relative density are equal. This gives insight in future to work on more relative densities and different loading conditions. Studies reveal that there is influence of platelets on the strength and stiffness of the sample which modelling them will give better understanding of the microstructural-relationship with the properties of the material.

REFERENCES

1. Lorna J.Gibson, M. F. (1997). *Cellular Solids Structure and Properties.* Krieger Publishing Coorporation.

2. D.Dhavale, N. (2016). *A comparision of microstructure and Uni-axial compressive response of Ice-templated porous Alumina Scaffolds fabricated from two different particle sizes.* Norfolk: ODU digital commons.

3. Deville, S. (2008). Freeze-Casting of porous Ceramics: A Riview of Current Achievements and Issues. *Advanced Engineering Materials*, 15.

4. Dipaankar Ghosh*, N. D. (2016). A comparision of microstructure and uniaxial compressive response of ice-templated alumina scaffolds fabricated from two different particle sizes. *Ceramics International*, 10.

5. Dipankar Ghosh*, H. K. (2016). Influence of anisotropic grains (platelets) on the microstructure and uniaxial compressive response of ice-templated sintered alumina scaffolds. *Acta Materialia*, 14.

6. Dipankar Ghosh*, M. B. (2016). Platelets-induced stiffening and strengthening of ice-templated highly porous alumina scaffolds. *Scripta Materialia* , 5.

7. Dipankar Ghosh*, M. B. (2017). On the brittle fracture characteristics of lamella walls of ice-templated sintered alumina scaffolds and effects of platelets. *Scripta Materialia*, 5.

8. Dipankar Ghosh*, M. B. (2018). Dynamic strength enhancement and strain rate sensitivity. *Scripta Materialia*, 5.

9. Mahesh Banda, D. G. (2018). Effects of porosity and strain rate on the uniaxial compressive response of ice-templated sintered macroporous alumina. *Acta Materialia*,

10. *Basic Waterjet Principles*. (2016, June 14). Retrieved from Water Jets.org Olsen Software LLC.

11. Olsen, J. H. (1999). Motion Control for Quality in Jet Cutting . *The Wayback Machine*.

12. Black, J. T., & Kosher, R. (2012). DeGarmo's materials and processes in manufacturing. *Wiley* , 226.

13. B.E Burakov, M. I. (2010). Crystaline Materials for Actinide Immobilisation . *Imperial College Press*, 198.

14. A.V. Manoylov, F. B. (2013). Modellinng of elastic properties of sintered porous materials. *Royal Society Publishing*, 19.

15. Hill, R. (1963). Elastic properties of reinforced solids: some theriotical principles. *Journal of the Mechanics and Physicss of Solids*.

16. T. J. Keating, P. W. (1975). An improved Method of Digital Image Correlation . *Photogrammetric Engineering and Remote Sensing* , 993-1002.

17. Bay BK, S. T. (1999). Digital Volume Correlation: Three dimensional stain mapping using X-ray Tomography . *Experimental Mechanics*.

18. Corelate, G. (2017). *3D testing Inspection Basic GOM software.* Germany: GOM corelate.

19. Dogan, S. W. (2001). Freeze Casting of Aqueous Alumina Slurries with Glycerol. *American Ceramic Society*, 6.

20. E.A. Nekliudova, A. S. (2014). Experimental research and finite element analysis of elastic and strength properties of fiberglass composite material. *Research Gate*, 18.

21. Ezra Feilden, T. G. (2017). Micromechanical strength of individual Al2O3 platelets. *Scripta Materialia*, 4.

22. GOM. (2013). *Aramis User Information- Hardware.* Germany: GOM.

23. J.Jamali, M. A. (2003). Micro-mechanics of off-axis loading of unidirectional composites using Simplified Unit Cell Model (SUM). *Research Gate*, 8.

24. J.S.Magdeski. (2010). The Porosity Dependence of Mechanical Properties of Sintered Alumina . *Journal of the University of Chemical Technology and Metallurgy*, 6.

25. John Tomblin, W. S. (2009). *Effects of Disbonds, Lighting Strikes and Low velocity Impact damage on Adhesively bonded composite joints.* Springfield: U.S Department of Transportation .

26. John Tyson 11, P. &. (n.d.). *Advanced Vehichle Structural Testing with Optical Metrology.* King of Prussia, PA : Trilion Quality Systems .

27. John Tyson, J. P. (2011). Advanced Material properties Measurements with Optical Metrology. *SAE International* , 10.

28. John TysonTimothy Schmidt, D. C. (2005). 3D Image Correlation for Dynamic and Extreme Environment Materials Measurements Holistic Structure Measurements from the Laboratory to the field. *SEM 2005 Conference Proceedings* (p. 9). Portland OR: Trillion Quality systems.

29. Jordi Seuba, S. D. (2016). Mechanical properties and failure bahavior of unidirectional porous ceramics. *Scientific Reports*, 11.

30. Kulkarni, M. (2012). *Finite Element Analysis of 2-D representative volume element.* Michigan: Digital Commons-Michigan Technological University.

31. Matthew J. Silva, W. C. (1995). The effects of Non-periodic Microstructure on the elastic properties of two-dimensional cellular solids . *Elsevier Science* , 17.

32. Matthew J.Silva, W. C. (1994). The effects of Non-periodic Microstructure on the elastic properties of two-dimensional cellular properties of two-dimensional cellular solids. *Elsevier Science Ltd*, 17.

33. Munro, R. G. (1996). Evaluated Material Properties for sintered alpha-Alumina. *American Ceramic Society* , 10.

34. Na Ni, S. B.-T. (2015). Understanding Mechanical Response of Elastomeric Graphene Networks. *Scientific Reports*, 14.

35. NASA. (2018). Optical 3D deformation and strain measurement. *American Society of Non-Destructive Testing* .

36. Oleksandr G.Kravchenko, G. G.-Z. (2018). Modelling Compressive Behavior of Open Cell Polymerized High Internal Phase Emulsions: Effects of Density and Morphology. *Royal Society of Chemistry* , 10.

37. Roberts, A. P. (2005). *Cellular Ceramics: Structure, Manufacturing, Properties and Applications.* Colombo: Wiley.VCH Verlag GmbH & Co. KGaA, Weinheim .

38. Stephen R. Heinz, J. S. (2010). Uniaxial compression analysis of glassy polymer networks using digital image correlation. *Elsevier*, 8.

39. Stephen W. Sofie, F. D. (2001). Freeze Casting of aqueous Alumina Slurries with Glycerol. *Journal of America Ceramic Society*, 6.

40. T.Schmidt, J. T. (2005). Performance Verification of 3D image Correlation Using Digital High-Speed Cameras. *Proceeding of 2005 SEM Annual Conference and Exposition*, (p. 10). Portland, OR .

41. Tsung-Hui Huang, T.-H. H.-S.-H.-Y.-W.-S. (2017). Phase-Field MModeling of Microstructural Evolution by Freeze-Casting. *Advanced Engineering Materials*, 13.

42. Zihiu Xia, Y. Z. (2003). *A unified periodic boundary conditions for representative volume elements of composites and applications.* Edmonton, Canada: International Journal of Solids and Structures.

VITA

Rahul Kumar Jujjavarapu

Education

Master of Science in Mechanical Engineering at Old Dominion University, May 2019.

Thesis Title: “Off Axis Compressive Response of Ice-Templated Ceramics.”

Bachelor of Technology in Mechanical Engineering at ALIET, Jawaharlal Nehru Technological University, India,2014

Project Title: “Formulation of Machine Cells and Part Families.”